THE PERFORMANCE OF A THERMAL TRANSIENT ANEMOMETER (TTA) FOR NONUNIFORM VELOCITY MEASUREMENTS

By

Sarah Plant

A THESIS

Submitted to
Michigan State University
in partial fulfillment of the requirements
for the degree of

Mechanical Engineering – Master of Science

2020

ABSTRACT

THE PERFORMANCE OF A THERMAL TRANSIENT ANEMOMETER (TTA) FOR NONUNIFORM VELOCITY MEASUREMENTS

By

Sarah Plant

A thermal transient anemometer (TTA) is a device used to measure fluid flow over a planar cross-sectional area. The TTA system includes a frame containing several cells arranged in a grid and an electronic control unit. Each cell contains a sensing wire which provides an area-averaged velocity measurement. The measuring strategy relies on the transient convection and the temperature decay of the sensing wire, which is correlated with the magnitude of the velocity. The relationship between the temperature decay and the velocity is determined by calibrating the TTA with a set of known uniform velocities.

The performance of the TTA under uniform and nonuniform flow conditions has been evaluated through numerical analysis and experimentation. Following the calibration of the TTA, a numerical model was developed to simulate the sensing wire in a TTA cell when exposed to a given velocity field. The model was used to investigate how linear velocity profiles affect the convective heat transfer and resulting temperature response of the sensing wire. Dimensionless velocity gradients ranging from 0 to 1.9 with corresponding mean velocities ranging from 0.1 to 15 m/s were evaluated. The temperature decay with velocity gradients exceeding 0.5 was slower than that of the uniform decay, due to strong axial conduction effects. This contributed to error in the mean velocity measurement from 1% with gradients of 0.4 to 24% with gradients of 1.9. A nonuniform flow correction scheme was developed using the numerical simulations that can reduce the mean velocity measurement error to within $\pm 1\%$ in the presence of large velocity gradients (≥ 0.4). The correction scheme was validated by experimental measurements using the TTA. The TTA was used to evaluate the distribution of flow exiting an automotive radiator for various installation configurations. The correction scheme was utilized in the presence of strong velocity gradients.

ACKNOWLEDGEMENTS

Special thanks to Dr. Foss and Dr. Klausner for the opportunity to work on this project. I'm lucky to have such knowledgeable advisors to guide and encourage me during my graduate studies. I'm appreciative of their patience and their adaptability during this time period.

I'd also like to thank my thesis committee, consisting of my two advisors and Dr. Petrasch, for their feedback and support.

To the doctorate and post-doctorate students I've met, thanks for the continuous academic (and emotional) support. I wish them the best of luck with their academic careers and future endeavors.

Finally, I'd like to collectively thank the faculty and staff within the Mechanical Engineering Department. Whether it was staying late during class office hours or offering advice for my research, I'm appreciative of my professors for always finding time in their busy schedules to help me.

TABLE OF CONTENTS

LIST OF TABLES

LIST OF FIGURES

LIST OF ABBREVIATIONS AND SYMBOLS

Abbreviations	**Description**
$AFRD$	Axial Fan and Research Development (facility)
CFD	Computational Fluid Dynamics
CTA	Constant Temperature Anemometer
TTA	Thermal Transient Anemometer
Coordinate Systems	**Description**
$x-y-z$	Spatial coordinate system
$x-y-s-\phi$	Spatial coordinate system (of TTA cell)
Greek Symbols	**Description**
γ	Resistivity (Ωm)
Δ	Percent difference
κ	Sum of U^3 for all TTA cells ($\propto$ kinetic energy flux)
ν	Kinematic viscosity (kg/ms)
ξ	Gradient (horizontal or vertical orientation)
ρ	Density (kg/m^3)
σ	Standard deviation
τ	Time constant (s)
θ	Angle
ζ	Temperature coefficient of resistance ($1/^\circ C$)

Roman Symbols	**Description**
A	Area (m^2)
C_D	Discharge coefficient
C_p	Specific heat (J/kgK)
D	Diameter (m)
dU^*/dx^*	Uniform horizontal velocity gradient (imposed along the length of a TTA cell)
dU^*/dy^*	Uniform vertical velocity gradient (imposed along the height of a TTA cell)
E	Voltage (V)
$\vec{F}$	Force vector (N)
Gr	Grashof number
h	Heat convection coefficient (W/m^2K)
H	Height of cell (m)
I	Current (A)
k	Thermal conductivity (W/mK)
L	Length of cell (m)
$\dot{m}$	Mass flow rate (kg/s)
M	Moment (Nm)
$\hat{n}$	Normal vector (m)
N	Number of samples
Nu	Nusselt number
P	Pressure (Pa)

Pr	Prandtl number
$\dot{q}$	Heat transfer over wire segment (kg/s^3)
$\vec{r}$	Position vector (m)
R	Resistance (Ω)
R^*	Dimensionless resistance
Re	Reynolds number
t	Time (s)
T	Temperature ($^\circ C$)
U	Velocity (m/s)
$\vec{U}$	Velocity vector (m/s)
w	Width of slit-jet opening (m)

Subscripts and Superscripts	**Description**
0	Initial condition
a	Ambient property
in	Inlet condition
max	Maximum
$mean$	Mean/average
min	Minimum
n	Nonuniform
ref	Reference property
u	Uniform
w	Wire property

CHAPTER 1

INTRODUCTION

1.1 Background

The thermal transient anemometer (TTA) is an instrument that measures mass or volume flow over a discrete region. For uniform density with a fixed cross section, the mean velocity is also determined. The TTA frame, which includes multiple interrogation cells, provides a detailed mapping of the flow distribution spanning the interrogation region. The TTA frame described here is applied for flow conditions in which the velocity is normal to the area of interest. The TTA in this work is shown in Figure 1.1.

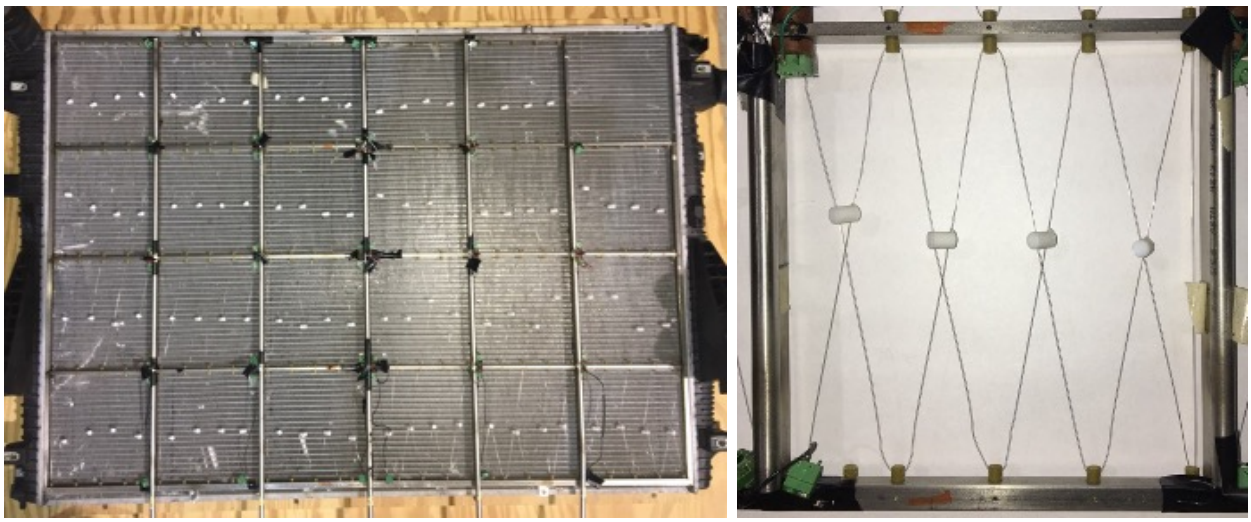

(a) TTA frame mounted on automobile radiator (b) Individual TTA cell

Figure 1.1: Images of TTA

The TTA is intended to measure the mass flow rate distribution for applications with large cross-sections, such as heat exchangers, gas turbine inlets, wind turbines, and pipe conduits, among others. Most instruments used to measure velocity are intended to provide a single-point measurement, and they need to be traversed over many points to resolve the flow field over a cross-section, which may be tedious or impractical. In contrast, the TTA

frame is specifically designed to resolve the flow distribution over a large cross-section.

The TTA is comprised of two parts; the frame with individual cells and an electronic control unit. The frame is subdivided into a grid containing several cells. The size of the frame and its corresponding cells are determined based on the area of interest and the desired length scale over which the velocity distribution needs to be resolved. Each cell contains a sensing wire used to measure the total temperature dependent resistance when subjected to the flow field. The sensing wire is strung in a multi-X pattern to recover an area-average flow rate measurement.

The electronic control unit provides a heating current to elevate the temperature of the sensing wire until it reaches a preset threshold resistance, R_T. Then the heating current is switched to a sensing current of 10 mA to record the resistance of the wire while it is allowed to convectively cool by flow field. The resistance of the wire exhibits an exponential decay [8],

$$R^* = \frac{R(t) - R_a}{R_0 - R_a} = e^{-t/\tau} \tag{1.1}$$

where R denotes the resistance of the wire, subscripts a and 0 refer to respective ambient and initial (when the sensing current starts) resistances, and τ denotes the time constant for resistance decay (proportional to temperature decay). The sensing wire resistance decay is observed until the dimensionless resistance reaches a value of $R^* = e^{-1}$. The duration of resistance decay to this point defines the time constant.

The TTA is typically calibrated by measuring the time constants for a set of uniform velocities. The mean velocity and measured time constant are related by the calibration equation [8],

$$\frac{1}{\tau} = A * U^B + C \tag{1.2}$$

where A, B, and C are calibration constants. Once a TTA cell is calibrated, the spatially averaged velocity, U, can be inferred from the measured time constant, τ. Using this strategy, the average velocity over each cell is evaluated, providing a comprehensive velocity distribution over the area of the frame.

1.2 Motivation

Internal combustion engines are found in transportation vehicles such as automobiles. They are used to convert chemical energy (through combustion of a fuel and oxidizer) to work. These engines produce heat from the combustion process, but require a controlled temperature environment to avoid damage and maintain a high-performance level.

In automobiles, the excess heat is addressed with the cooling system. Generally, a liquid is circulated through the engine, carrying the excess heat from the engine to the radiator assembly. This assembly consists of the radiator with an attached shroud and fan. As air passes through the radiator, fins are used to assist in the convective dissipation of heat from the liquid to ambient air. The cooled liquid is then returned to the engine. Often, vehicles are moving at fast enough speeds to provide a sufficient amount of airflow through the radiator to dissipate heat from the coolant. However, at high ambient temperature conditions or low vehicle speeds, a fan is used to draw in excess air through the radiator.

Knowing the magnitude and distribution of airflow through the radiator is necessary for analyzing the cooling performance. One method for improving the cooling system is to optimize the design of the fan or shroud to create more homogeneous airflow at the appropriate operating condition. This requires a detailed understanding of the air passing through the radiator. The TTA is an instrument well suited to measure the airflow distribution through a radiator with and without a shroud. The thin frame of the TTA fits between the exit plane of the radiator and shroud with minimal blockage of the radiator flow area. In doing so, the exiting flow is minimally disrupted.

1.3 The Present TTA Description

The TTA frame used in this work is designed to span the area occupied by a stock automobile radiator. The frame is fabricated from stainless steel with outer dimensions of 0.698 m x 0.981 m. This area is subdivided into a 6 x 4 grid containing 23 cells (the top left cell is omitted for mounting purposes) to provide a detailed survey. Each cell has inner

length and height dimensions of 154 mm x 166 mm. The sensing element is a 1.6 m long, 0.2 mm diameter tungsten wire, chosen for its high temperature coefficient of resistance, making it sensitive to temperature changes. Garolite rods serve as tether points to secure the sensing wire to the edge of the frame and provide electrical and thermal insulation from the stainless steel. The garolite rods measure 4.5 mm in diameter and are placed 36 mm apart. Teflon spacers measuring 6.5 mm in diameter are added where the wire crossed at the 'X', to prevent radial conduction. Terminal blocks are used to connect the endpoints of the sensing wire to the electrical wires.

The electrical control unit is supplied by Sakor Technologies Inc. It is used to supply the heating current to the sensing wires and to record the transient resistance. Upon operation of the TTA, the control unit supplies a heating current of 2 A to the sensing wire for a specified duration of time, called the pulse time. The current is then switched to the 10 mA sensing current to record the resistance during the decay period. The time constant, τ, is determined within the program based on Equation 1.1 at the end of the cooling period.

The control unit is accessed through a LabView program installed on the PC. From the program, the user can specify the specific row(s) of interest and adjust the pulse time and/or duration of the cooling period. The resulting data in the form of the time constant, velocity, and/or temperature can be recorded from within the program.

1.4 Prior Work

The TTA was first introduced by Foss *et al* [8]. A later publication, Foss *et al* [7], explored the ambient temperature and free stream turbulence effects on the TTA. The calibration (with ambient temperature, $T_a = 30°\text{C}$) was used to determine the mean velocity when the TTA was subjected to elevated ambient temperatures for measurements ($T_{a,cal} \leq T_{a,meas}$). It was found that the room temperature calibration could be used to adequately measure the velocity magnitude when the free stream temperatures of $T_{a,meas} = 50°\text{C}$, $70°\text{C}$, $100°\text{C}$ were present. Based on results from the ambient temperature exploration, Foss also concluded

that the radiation effects did not influence the heat transfer of the TTA. The freestream turbulence was evaluated with controlled disturbance levels. It was found that the TTA was insensitive to disturbances in the approaching flow. In these conditions, the TTA was found to maintain the $1/\tau = f(U)$ relationship established after calibration.

In the M.S. thesis by Leung [11], the radiator in application was studied using the TTA. During this stage the present TTA was fabricated. Leung introduced the question of how the TTA would perform under nonuniform flow distributions. This thesis attempts to build upon that framework to answer the question.

1.5 Objectives

Previous investigations have demonstrated confidence in the TTA as a measuring tool when free stream turbulence and radiation effects are present, but have not addressed concerns when the velocity distribution is nonuniform. Practical applications suggest the possibilities of nonuniform velocity distributions in the flow fields of interest. The present investigation establishes a parameter space in which the TTA can accurately measure uniform and nonuniform flow using the uniform calibration.

CHAPTER 2

EXPERIMENTAL FACILITY AND MEASUREMENT TECHNIQUES

2.1 The Test Facility

The present investigation is conducted in the Axial Fan Research and Development (AFRD) facility at Michigan State University. This vertical wind tunnel provides a constant, uniform velocity flowing in the downward direction. In previous investigations, the facility was utilized to study axial fans, but the design accommodates a wide variety of geometries. The large inlet allows for convenient mounting of the TTA and radiator in the various installation conditions. Features of the AFRD facility are outlined in Figure 2.1.

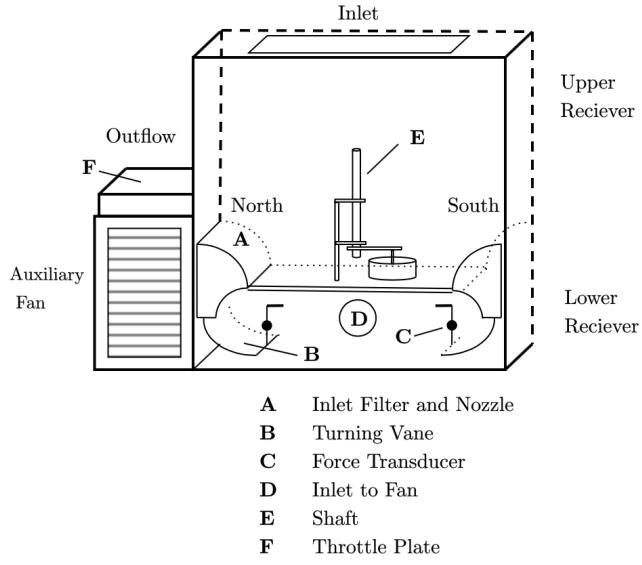

(a) Schematic of interior

(b) Image of exterior

Figure 2.1: Axial Fan Research and Development facility

The vertical wind tunnel transports air from above the AFRD into the upper receiver, via the inlet. The air is driven by the auxiliary fan, with an adjustable throttle plate (F) to control the mass flow rate. Air enters the upper receiver and is directed to the lower receiver through the nozzles (A) on the north and south end of the facility. After passing through

the nozzles, turning vanes (B) direct the air back to the inlet of the fan (B). The two turning vanes are used to measure the net moment of momentum flux using force transducers (C). A vertical shaft within the upper receiver (E) can be used to mount axial fans. Morris *et al* [13] provide a detailed description of the AFRD facility.

The AFRD introduces a unique measurement system for the mass flow rate, using the net moment of momentum flux. The incoming air passes through the nozzles and undergoes a 90° turn across the turning vanes. The turning vanes are supported by a knife-edge pivot to provide the net moment of momentum flux [13],

$$\sum M = \vec{r} \times \vec{F} = \int_{CS} \rho \left(\vec{r} \times \vec{U} \right) \left(\vec{U} \cdot \hat{n} \right) \tag{2.1}$$

where $\vec{r}$ represents the radius from a point on the pivot, $\vec{F}$ represents the measured force, $\vec{U}$ represents the fluid velocity, $\hat{n}$ represents the normal vector, and CS is the control surface. Features of the system are shown in Figure 2.2.

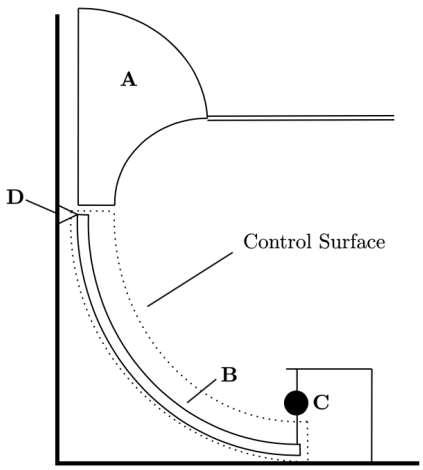

Figure 2.2: Schematic representation of the net moment of momentum flux measuring apparatus

The force transducers, located on the opposite edge of the turning vanes, measure the force from the incoming air, which is proportional to the mass flow rate.

2.2 Measurement Techniques and DAQ

Several measurement techniques are available to measure the mean velocity or mass flow rate. While the thermal transient anemometer is one such method, another independent measurement is needed for the calibration of the TTA and for reference. Other measuring techniques utilized in the present study include: (i) the force transducers in the AFRD for a mass flow rate measurement, (ii) a hot-wire anemometer for local velocity measurements, and (iii) a pitot probe for local velocity measurements. Methods (i) and (ii) are discussed in Sections 2.3 - 2.4, as they require an instructive calibration process. The pitot tube in combination with a pressure transducer or manometer does not require such calibration and is accurate within $\pm 0.3\%$ [14].

It is noted that only the force transducers provide a direct mass flow rate measurement, and the mean velocity can be inferred with knowledge of the cross-sectional area and density. The pitot probe and hot-wire anemometer provide a direct local velocity measurement.

The air density is acquired using the barometric pressure and temperature (converted to density using $P = \rho RT$). The barometric pressure is acquired through the Lansing airport (LAN) hourly pressure readings. The altitude in the test facility is understood to be the same as that of the airport, making it a reasonable source for the barometric pressure. The temperature is based on ambient conditions (typically $24°\text{C} \leq T_a \leq 26°\text{C}$). The pressure is measured using an MKS Baratron capacitance manometer, with an uncertainty of $\pm 0.25\%$ in a 10 V signal range.

Data is acquired using the LabJack Pro T7 board. The board has a 16-bit analog to digital conversion with a ± 10 V range and is controlled through a program installed on the PC. The LabJack Pro is utilized for data acquisition (DAQ) in which the pressure transducer, strain gauges (north and south), and CTA anemometer (for hot-wire measurements) are connected. Data acquired with the board is taken over a time period (typically between 30 – 60 seconds) at a scan rate of 20 Hz, then averaged in post-processing to provide a time-averaged measurement.

2.3 The Force Transducers

The force transducers are constructed with a proving ring, each containing four strain gauges fastened to create a Wheatstone bridge circuit. The force transducers are utilized for the mass flow rate measurements within the AFRD facility. The established relationship between the measured force (as a voltage) and the mass flow rate is determined after calibration. The uncertainty in the strain gauges is $\pm 0.5\%$ and $\pm 0.4\%$ for the north and south strain gauges respectively [13].

2.3.1 The Slit-Jet and its Discharge Coefficient

The calibration of the strain gauges require a slit-jet orifice for proper measurement. The air passing through the slit-jet resembles a nominally steady, incompressible, inviscid flow (in an otherwise viscous flow), wherein the Bernoulli equation can be utilized for the determination of velocity [14]. That is,

$$U = \sqrt{\frac{2\Delta P}{\rho}} \tag{2.2}$$

where ΔP is change the pressure (from atmosphere to upper receiver) and ρ is the density of the air.

The slit-jet consists of two identical nozzle plates, of length L, in planar position with the opening or 'slit', of width w. The nozzles are placed a distance of w apart such that $L/w \gg 1$. The thickness of the nozzle is very small in proportion to its length, so as to maintain two-dimensional flow characteristics.

The vena contracta describes the point of maximum velocity and occurs downstream of the slit opening. For air, this distance is approximately $1.5w$ downstream of the opening. The calculated velocity in Equation 2.2 refers to the vena contracta velocity.

Potential flow analysis suggests that the discharge coefficient, C_D – the ratio which compares the mass flow rate at the end of the nozzle to the mass flow rate of an ideal nozzle – is a value of ≈ 0.611. The discharge coefficient is of interest for mass flow rate calculations

in nozzles particularly, where the mass flow rate is then given by [14],

$$\dot{m} = \rho U A C_D \tag{2.3}$$

where U refers to the velocity calculated using Equation 2.2 and A is the area of the slit-jet opening.

The slit-jet used in calibration is comprised of two sets of nozzles fabricated from 1.5 mm (nominally 1/16") thick stainless steel plates with L x w to be 14 cm x 100 cm. The nozzles are supported by thin (1.5 mm wide, 12.7 mm deep) ribs spaced 2.54 cm apart at the separation lip to ensure the required planar condition. The nozzles rest on a piece of 1.25 m x 1.25 m medium-density fiberboard (MDF), with a cutout to clear the nozzles and ribs. Two pieces of 35 cm x 1.25 m sheet metal are placed vertically on either side of the slit-jet as guidance rails, to ensure incoming air only in the y-direction. Two pieces of 14 cm x 100 cm sheet metal are placed to cover the remainder of the MDF for smooth airflow transition. The slit-jet setup for the force transducer calibration is in Figure 2.3.

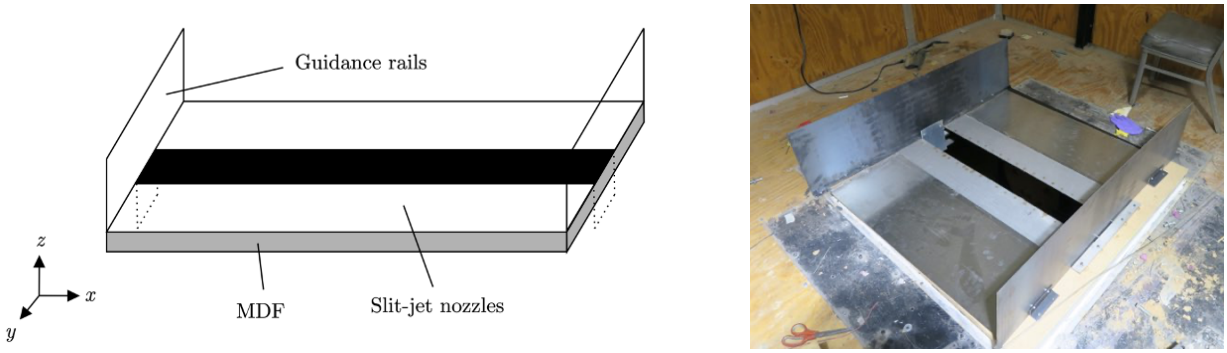

(a) Schematic of setup

(b) Image of setup

Figure 2.3: Slit-jet nozzle mounted at AFRD inlet for calibration of force transducers

2.3.2 Computational Fluid Dynamics (CFD) Analysis on the Discharge Coefficient

Although close, the slit-jet utilized in calibration does not provide perfectly inviscid flow. Attempts to quantify the expected discharge coefficient for mass flow rate calculations are done using computational software. Ansys Fluent software is utilized for CFD analysis.

The Fluent model consists of a two-dimensional geometry (simplified to two dimensions due to uniform flow in the x-direction) matching the dimensions of the fabricated slit-jet. The length, L, is 1 m, with a thickness of 1.5 mm. The slit width, w is 140 mm. The induced air coming from the atmosphere, is assumed to come uniformly from all sides, thus modeled by a semi-circle (radius equivalent to 1.07 m). The exit is made far enough away so as to analyze the jet profile downstream (3 m away downstream of slit-jet). The modeled slit-jet is shown in Figure 2.4. Note that the velocity flows 'downward' in the z-direction.

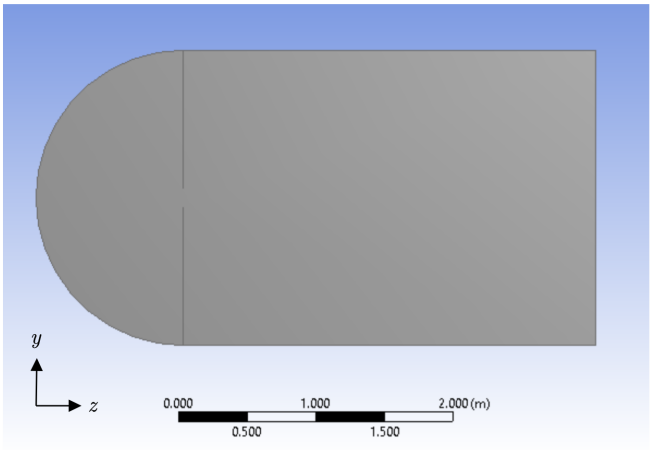

Figure 2.4: CFD model of slit-jet

No-slip boundary conditions are implemented at the walls and slit-jet. The velocity is defined incoming in the normal direction from the semi-circular 'atmosphere'. This creates a sink around the opening of the slit-jet.

The discharge coefficient, C_D, is calculated based on the following equation,

$$C_D = \frac{\pi D U_{in}}{2 U_{max} w} \tag{2.4}$$

where D is the diameter of the 'atmosphere' (semicircle representative of atmosphere), U_{in} is the inlet velocity (normal to semicircle as defined within Fluent), and U_{max} is the maximum or vena contracta velocity (determined from Fluent solution). The discharge coefficients calculated are a function of velocity are shown in Figure 2.5.

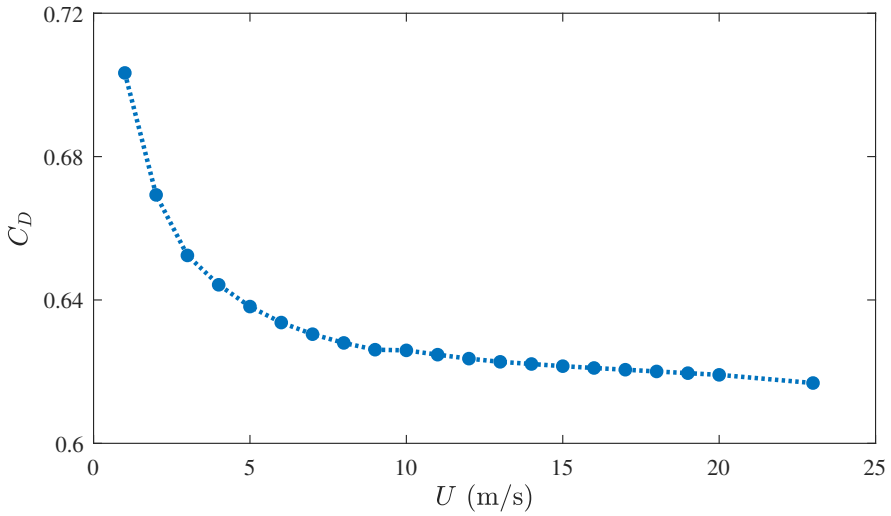

Figure 2.5: Discharge coefficient calculated using Fluent for various maximum velocities

The inability of the streamline to make abrupt turns is a distinguishable trait which is visible in the CFD results, following proper setup. As the flow approaches the opening, the velocity should gradually increase as a result from the interfering nozzles. For this reason, a vertical (z-direction) velocity field is modeled in Fluent and compared to hot-wire measurements for validation of the Fluent analysis.

For the supporting measurements, the hot-wire is mounted on a digital height gauge to take a vertical survey of the flow in 1 mm increments. The height gauge is positioned out of the jet path so as to not disrupt hot-wire readings. At a distance of approximately 2 mm away from the edge of the nozzle (laterally), the vertical survey is taken to assess the profile of the turning flow. Starting at a vertical height approximately parallel to that of the slit-jet ($\pm$ 0.5 mm), the hot-wire is traversed upward a distance of 7 mm for a total of 8 measurements. This process is repeated for two different flow conditions with corresponding maximum velocities, U_{max}. Note that only one nozzle is evaluated, as it can be assumed that the velocity profile is the same for the other nozzle due to symmetry. The setup is illustrated in Figure 2.6.

(a) Hot-wire placed 2 mm away from slit-jet nozzle

(b) Hot-wire mounted on digital height gauge

Figure 2.6: Hot-wire setup for CFD validation of discharge coefficient

The vertical velocity component is extracted from the Fluent simulation and compared to the hot-wire measurements in Figure 2.7. For the two inlet settings (20 and 23 m/s) with respective maximum velocities, the hot-wire results from the vertical survey are in reasonable agreement with the Fluent analysis so as to proceed with the determined discharge coefficients.

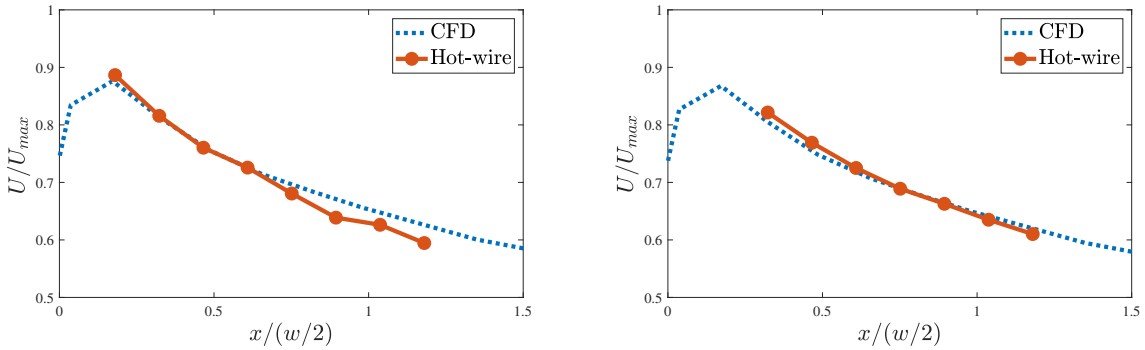

(a) Inlet condition with maximum velocity of 20 m/s

(b) Inlet condition with maximum velocity of 23 m/s

Figure 2.7: Comparison of hot-wire and Fluent velocity vertical survey

2.3.3 Procedure for Calibration

After confirming the discharge coefficients as determined in Fluent, the force transducers are calibrated. The relationship between the voltage of the strain gauges (proportional to the force) and the mass flow rate is established during the calibration.

Fifteen inlet conditions (inlet flow rates) are measured in the calibration process. The pressure drop, barometric pressure, temperature, and voltages as measured by the north and south strain gauges, are recorded for each inlet condition. This process is repeated for each inlet condition.

Equation 2.3 is utilized for the mass flow rate calculation. The area of the slit-jet is 0.14 m^2, while the respective velocity is determined from the Bernoulli Equation (Equation 2.2) based on the pressure drop between atmosphere and upper receiver. For the calibration, it can be assumed that the mass flow rate is split evenly between the north and south strain gauges – that is each strain gauge measures half of the mass flow rate passing through the AFRD. The calibration curve for the strain gauges is shown in Figure 2.8.

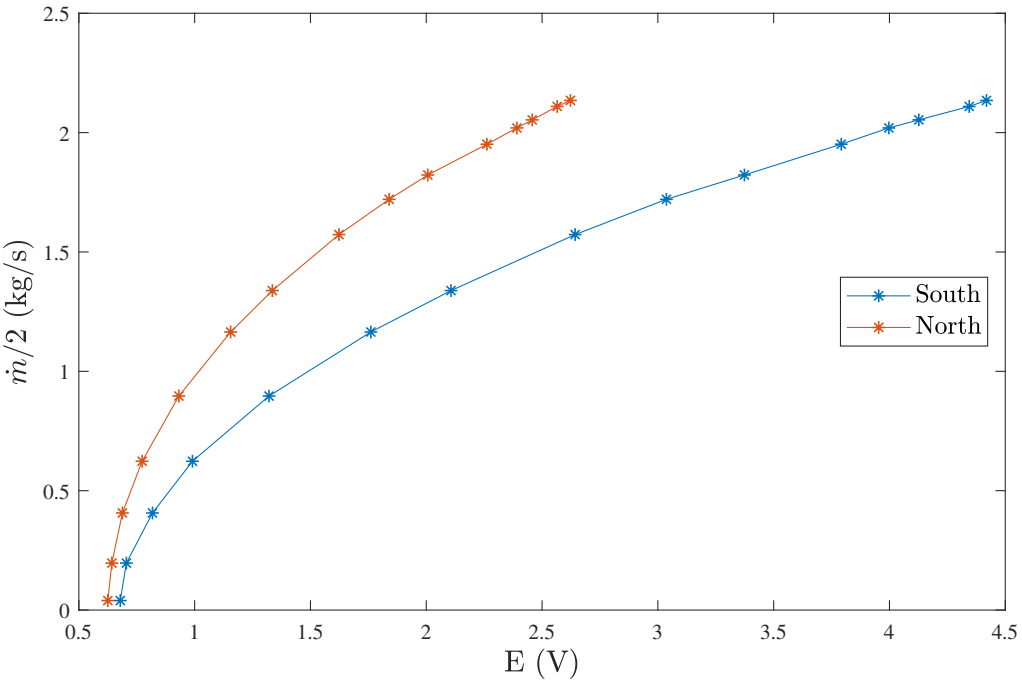

Figure 2.8: North and south force transducer calibration

2.3.4 Final Notes on the Force Transducers

The unique measuring strategy of the force transducers provides a mass flow rate measurement following calibration. The calibration is limited within 0.08 kg/s $\leq \dot{m} \leq$ 4.27 kg/s. This equates to a velocity of roughly 40 m/s for the nozzle area (0.14 m^2) and 5 m/s for the experimental inlet area (0.68 m^2). Therefore the maximum mass flow rate measured with the experimental inlet (approximately 8 kg/s) cannot be precisely evaluated using the force transducers, as it exceeds the calibration range. Additionally, at high mass flow rates ($\sim$4 kg/s), the uncertainty in the measurements is approximately $\pm$0.5 V or $\pm$10% error in mass flow rate.

Presumably, the force transducers in the AFRD favor a smaller inlet area in combination with lower mass flow rates ($\dot{m} \leq$ 4 kg/s) for accurate measurements. For this reason, it is decided to measure the reference velocity using other techniques. To preserve the strain gauges, a block is placed underneath the turning vanes to prevent deformation at high mass flow rates.

2.4 Hot-wire Anemometry

A Dantec MiniCTA (constant temperature anemometer) control unit is utilized to provide a constant temperature to the hot-wire probe to measure the velocity. The operating principle of a hot-wire anemometer is similar to that of the TTA – it measures the convective heat transfer of the wire related to the fluid velocity.

The hot-wire probe is shown in Figure 2.9. The probe consists of prongs holding a 5 μm diameter wire with a resistance of 0.4 Ω. The thin wire allows the hot-wire to measure velocity fluctuations at fine scales.

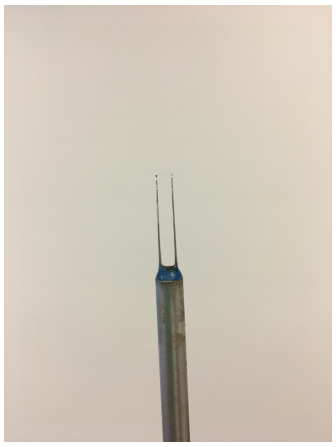

(a) View of probe sensor

(b) Entire probe

Figure 2.9: Hot-wire probe

2.4.1 Procedure for Calibration

Standard experimental techniques require the hot-wire to be calibrated each time before measurements. The calibration is good for about 3-4 hours, after which it should be re-calibrated again. The relationship between the hot-wire voltage and the velocity follows the hot-wire calibration equation [12],

$$E^2 = A + BU^{0.43} \tag{2.5}$$

where E is the voltage and A and B are constants established after the calibration process.

The hot-wire is calibrated in the facility illustrated in Figure 2.10. The facility includes a blower, to provide an inlet base condition and slit-jet exit, where the hot-wire is placed. The blower provides velocities at the inlet via an adjustable throttle plate.

(a) View of facility and blower (b) View of slit-jet exit

Figure 2.10: Hot-wire calibration facility

After powering on the CTA and waiting 30 minutes to warm up, the hot-wire sensor is placed in the calibration facility at a distance of approximately $x/w = 1.5$ away from the slit jet. This is to ensure the hot-wire measures the velocity directly related to the plenum pressure (see Equation 2.2). The sensor is mounted in the same orientation with respect to the flow (0° or 90°). The throttle on the blower is adjusted to vary the inlet velocity. Selected inlet velocities (between 8 - 16 velocities) well within the range of expected velocities (typically between 1 to 25 m/s) are used. Measurements for both the hot-wire and plenum pressure are taken over a 30 second period and recorded with the LabJack Pro for each inlet velocity. A least-squares curve-fit is fit to the data to follow Equation 2.5.

It is important to note that while the slit-jet and its discharge coefficients are necessary in determining the mass flow rate for the strain gauge calibration in Section 2.3, the discharge coefficient is not necessary in the hot-wire calibration. This is because the hot-wire measures the velocity instead of the mass flow rate, which can be computed using the Bernoulli equation (Equation 2.2).

An example calibration is shown in Figure 2.5. Note, that the hot-wire calibration curve varies slightly with each new calibration. For the calibration illustrated, the constants A and

B are 1.73 and 1.09 respectively.

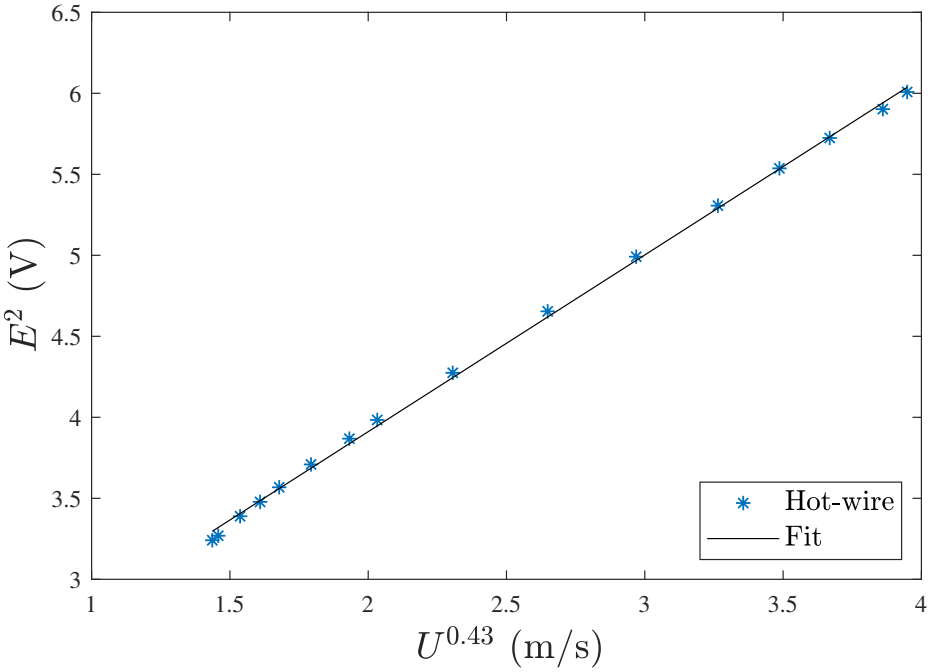

Figure 2.11: Sample hot-wire calibration curve

CHAPTER 3

CALIBRATION OF TTA

The TTA is calibrated in the AFRD facility. The calibration is used to establish a relationship between the time constant for resistance decay, τ, and the passing velocity, U, for each cell, as noted in Equation 1.2. Once calibrated, the TTA can be used to infer a velocity based on the measured time constant, τ.

Measurements using the TTA rely on an accurate and robust calibration. It is suggested that the entire TTA frame be calibrated every few months when not in use. This is due to the sensitivity of the sensing wires and connectors that can experience small changes in ambient resistance over time.

3.1 Procedure for Calibration

During calibration the TTA is supported by a piece of medium-density fiberboard (MDF). The MDF is placed at the inlet of the AFRD and a hole is cut to redefine the inlet area to match the dimensions of the TTA (excluding the outer frame), that is 0.96 m x 0.68 m. The outer frame of the TTA then rests on the MDF. Quarter-rounds are placed around the perimeter of the TTA to uniformly guide air to the TTA. A hot-wire is used to measure the velocity. The hot-wire sensor is placed 5.08 cm (2") above the TTA sensing wire. In this position, the hot-wire measures the velocity of the approaching flow to the sensing wire. The setup is shown in Figure 3.1.

The throttle plate on the AFRD is adjusted to vary the inlet velocity between 0.1 to 13.1 m/s. Seventeen measurements (between 15-20 measurements is recommended) spaced evenly within this range are used for the calibration. At each velocity, ten measurements are taken with the TTA (pulse time of 0.3 seconds, duration of 3 seconds). The average of the ten measurements (excluding any outlying data) is determined in post processing.

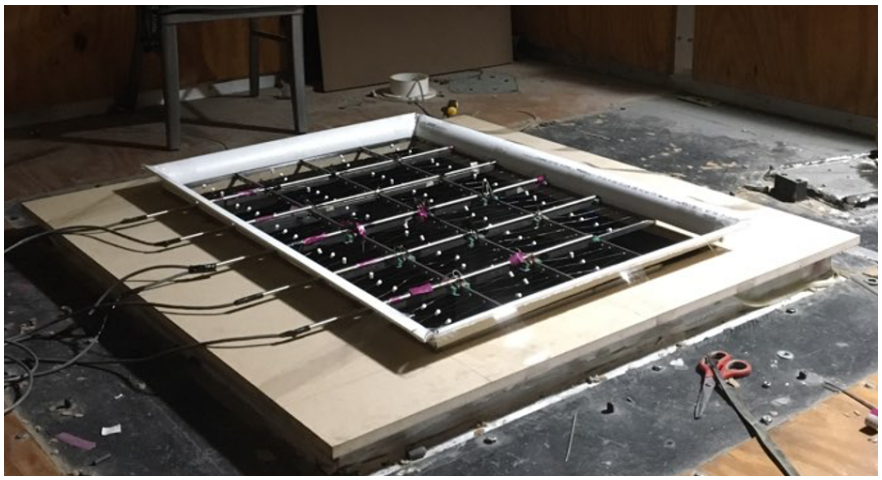

(a) TTA placed on MDF with quarter-rounds at inlet

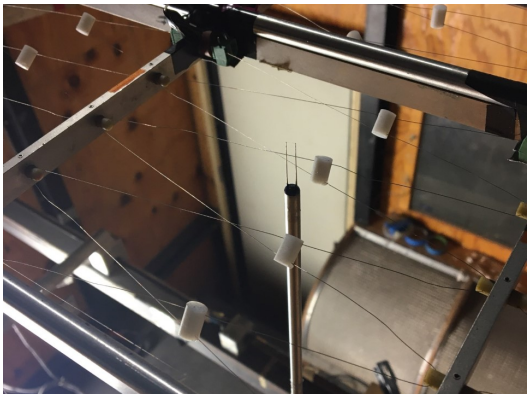

(b) Hot-wire probe sensor placed 5.08 cm above the plane of the TTA sensor wires

Figure 3.1: TTA calibration setup at inlet of AFRD facility

3.2 Calibration

Since each of the 23 cells in the TTA frame has a unique calibration curve, each cell is assigned a number for reference. The number assignments for the TTA cells is shown in Figure 3.2. Note that the dimensions of the frame and cells are not to scale.

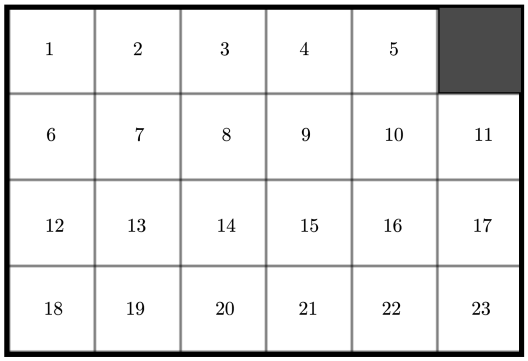

Figure 3.2: TTA cell number assignments

Using the hot-wire velocity measurements the TTA is calibrated according to Equation 1.2 ($1/\tau = A * U^B + C$). The calibration constants A, B, and C for each cell are determined using a least-squares curve-fit for the time constant data points. The calibration curve for cell 1 is shown in Figure 3.3 (See Appendix A for all cell calibration curves). The calibration constants for each cell are listed in Table A.1 in Appendix A.

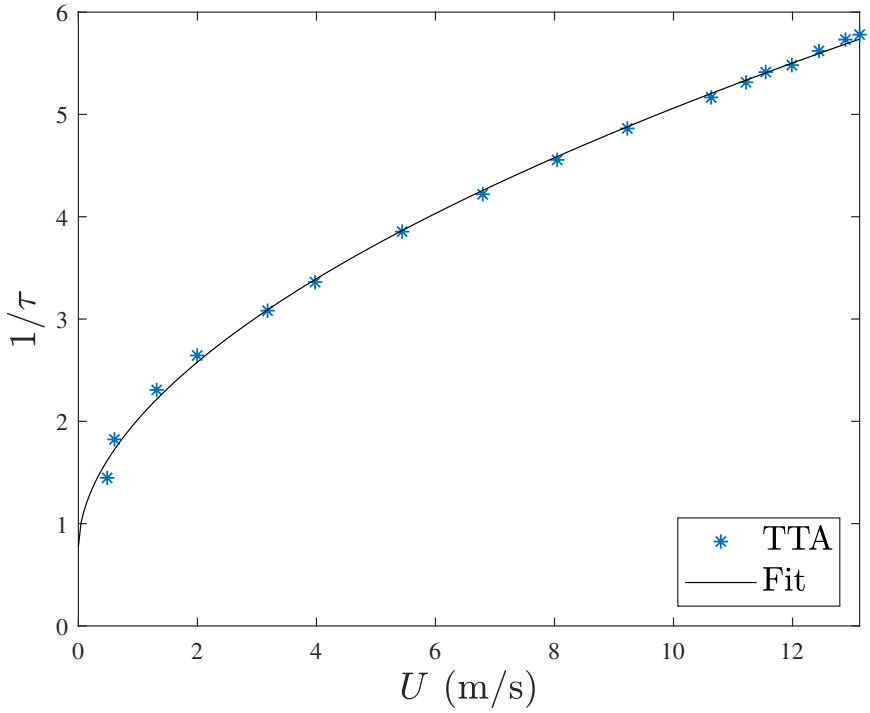

Figure 3.3: TTA calibration curve for cell 1

3.3 Uncertainty

The standard deviation between the calibration fit and the data points is used to estimate the measurement uncertainty. The standard deviation, σ, is defined as [7],

$$\sigma = \sqrt{\frac{1}{N-1}\sum_{i}^{N}(U_{calc} - U_{meas})_i^2} \tag{3.1}$$

where N is the number of samples ($N = 17$, for the total velocity samples taken).

The uncertainty for all the cells is shown in Table 3.1.

Cell Number	Uncertainty (m/s)
1	0.3317
2	0.2290
3	0.3176
4	0.4597
5	0.3797
6	0.0656
7	0.1251
8	0.0812
9	0.1410
10	0.1794
11	0.1004
12	0.1055
13	0.1721
14	0.1324
15	0.1040
16	0.1121
17	0.1855
18	0.1340
19	0.3656
20	0.1926
21	0.2141
22	0.1687
23	0.1624

Table 3.1: Calibration uncertainty for each cell

CHAPTER 4

NUMERICAL SIMULATIONS

A significant portion of the TTA investigation includes computational analysis and simulation of the sensing wire, later supported by experimentation (see Chapter 5). The computational simulation is utilized to study the convective heat transfer effects of uniform and nonuniform velocity profiles on the response of a TTA cell. A TTA cell is calibrated with a uniform velocity field and thus the temperature and thermophysical properties of the sensing wire are uniform. A concern arises when the TTA cell is subjected to a nonuniform velocity field, since the sensing wire temperature and thermophysical properties will also be nonuniform along the length of the wire. When measuring mean velocity in the presence of a nonuniform velocity field, it is of interest to understand the error introduced by temperature and thermophysical property nonuniformities. This understanding is garnered by solving a transient energy model for the sensing wire that is developed within a MATLAB computational platform.

4.1 Model and Assumptions

A schematic depiction of a TTA cell is shown in Figure 4.1. Each cell consists of a single sensing wire, strung across the entire cell in a multi-X pattern; therefore the wire position, s, is defined with respect to the spatial coordinates (x, y, ϕ) of the cell.

A transient heat transfer model is used to compute the temperature distributions along the sensing wire for various flow conditions. The thermal energy conservation equation for the wire is [11],

$$\frac{1}{\rho Cp}\frac{\partial k(s,t)}{\partial s}\frac{\partial T_w(s,t)}{\partial s} + \frac{k(s,t)}{\rho Cp}\frac{\partial^2 T_w(s,t)}{\partial s^2} - \frac{4h(s,t)}{\rho C_p D}(T_w(s,t) - T_a) + 16\frac{I^2\gamma(s,t)}{\rho C_p \pi^2 D^4} = \frac{\partial T_w(s,t)}{\partial t} \tag{4.1}$$

where s is the position along the wire (see Figure 4.1) and T_w is the temperature of the wire.

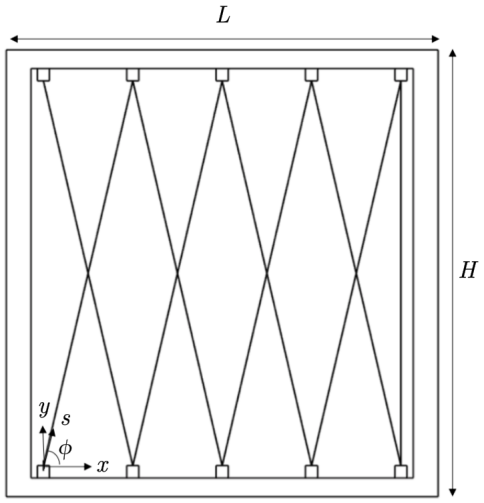

Figure 4.1: Schematic representation of a TTA cell

The derivation of the energy equation is in Appendix B.1.

The transient model is used to simulate the transient variation of temperature during two different time periods. The first period is the heating period, in which a controller is used to pass 2 A of current through the wire for heating. The resistance and temperature of the wire are computed at each time step (Δs=1 ms). Once the resistance reaches the threshold resistance at $R_T = 5\Omega$, the current is switched to a sensing level of 10 mA and the second period begins. The temperature of the wire decays due to convection by the passing air flow. This period is referred to as the cooling period and continues until the wire reaches a dimensionless resistance (defined by Equation 1.1) of $R^* = e^{-1}$. The time during the second period for R^* to reach e^{-1} is the time constant. Computational methods for determining the time constant are discussed in Section 4.2.2.

For both time periods, Equation 4.1 is solved explicitly with a forward marching scheme in time and space. The spatial step, Δs, is a value of 1 mm ($\Delta s/D = 5$) and the time step, Δt is a value of 1 ms; these increments are selected to maintain stability. The MacCormack predictor-corrector method [2] is used to obtain second order accuracy. The following assumptions are inherent in the model. Heat conduction is neglected in the radial direction. This is justified due to the very low Biot number. Thermal expansion and contraction of

the wire is neglected since the wire temperature does not exceed 250°C. Heat exchange with the garolite rods, Teflon spacers, and electrical connectors is neglected. The endpoints of the wire are assigned adiabatic boundary conditions. The initial condition sets the wire temperature to that of the ambient.

4.1.1 Thermophysical Properties

The temperature of the wire, calculated from Equation 4.1, depends on several temperature dependent thermophysical properties of the air and the tungsten wire. The variables ρ, C_p, D, and I – the density (of the tungsten wire), specific heat (of wire), diameter (of wire), and electrical current respectively are taken to be constant. The density and specific heat can be taken as constants since there is little variation over the temperature range of interest ($20°\text{C} \leq T_w \leq 250°\text{C}$). These values are listed in Table 4.1. The remaining properties in Equation 4.1 such as k (thermal conductivity of tungsten), h (heat convection coefficient), γ (resistivity of tungsten) are taken to be temperature dependent.

Property	Value
C_p (tungsten)	133.15 J/kgK
k_a (air)	$25.4 * 10^{-3}$ W/mK
R_a	2.85 Ω
T_a	24°C
T_{ref}	30°C
γ_{ref}	$5.6 * 10^{-8}$ Ωm
ρ (tungsten)	$19.3 * 10^3$ kg/m^3
ζ	$4.403 * 10^{-3}$ 1/°C

Table 4.1: Constant properties used in simulation

The properties of the tungsten sensing wire (k, γ) are evaluated at the respective temperature of the wire while the properties of air (pertaining to h) are evaluated at the film temperature ($T_f = (T_a + T_w)/2$). The respective thermal properties are provided from tables in two Heat Transfer texts [5] and [10]. The tables of properties are used to create a best-fit equation for each property to describe it as a function of temperature. This is done in

lieu of interpolation. The relations for air and tungsten properties (specific heat, kinematic viscosity, Prandtl number, and thermal conductivity) are shown in Appendix B.2.

4.1.2 Sensing Wire Resistance

The sensing wire resistivity is evaluated locally at the wire temperature $T_w(s,t)$. The resistivity of tungsten characterizes the material response to the electrical current. It is used in the heat generation term in the energy equation (Equation 4.1) and for determining the resistance (see Equation 1.1). The resistivity varies linearly with temperature and is represented as,

$$\gamma(s,t) = \gamma_{ref}\left[1 + \zeta(T_w(s,t) - T_{ref})\right] \tag{4.2}$$

where ζ is the temperature coefficient of resistance. The value of ζ is shown in Table 4.1.

The resistance of the tungsten wire is an integral quantity over the length. The wire resistance is computed as [11],

$$R(t) = \frac{\int_0^L \gamma(s,t)ds}{A} \tag{4.3}$$

where A refers to the cross-sectional area of the wire, that is $A = \pi D^2/4$.

Best-fit polynomial equations based on the tables for tungsten [10] are utilized for the thermal conductivity and specific heat computations. A 6th order polynomial is fit to the thermal conductivity scheme while an 8th order polynomial is fit to the specific heat of tungsten. Note that the specific heat of tungsten is a constant value based on the ambient temperature and the best-fit polynomial is utilized to determine that condition, whereas thermal conductivity is not a constant value. The exact equations and fits are shown in Appendix B.2.

4.1.3 Air Characteristics

The properties of air are computed at the film temperature. The boundary layer temperature of the air passing over the wire during convection can be assumed as the average of the

ambient and wire temperatures, $T_f = (T_a + T_w)/2$.

The convective heat transfer coefficient over the wire is,

$$h(s,t) = \frac{k_a Nu(s,t)}{D} \tag{4.4}$$

where k_a refers to the thermal conductivity (of air) at ambient conditions and Nu refers to the Nusselt number.

The Nusselt number is characteristic of the subject geometry and convection method. Several correlations exist to describe forced convection over a wire (or a long, thin cylinder). The chosen correlation used in the simulations is a modified version of the Hilpert correlation [5] for flow over a cylinder. The Hilpert correlation suggests different values for c and m in Equation 4.5 based on the Reynolds number regime during operation. However, the suggested constants are slightly modified to fit the TTA calibration (see Section 4.2.1). The Nusselt number is,

$$Nu(s,t) = cRe(s,t)^m Pr(s,t)^{1/3} \tag{4.5}$$

where c and m are the constants defined by the Reynolds number regime. Re and Pr are the Reynolds and Prandtl numbers respectively. See Section 4.2.1 for determination of the constants c and m.

The Reynolds number for flow over the sensing wire is defined as,

$$Re(s,t) = \frac{U(s,t)D}{\nu(s,t)} \tag{4.6}$$

where ν is the kinematic viscosity of the fluid at the film temperature.

After combining Equations 4.5 and 4.6, the heat convection coefficient is rewritten as,

$$h(s,t) = \frac{k_a c U(s,t)^m D^{m-1} Pr(s,t)^{1/3}}{\nu(s,t)^m}. \tag{4.7}$$

Best-fit polynomials based on tables [5] for kinematic viscosity and Prandtl number are used to describe the air properties. The corresponding equations and fits are shown in Appendix B.2.

4.2 Simulation Considerations

4.2.1 Nusselt Number Determination

For the numerical simulations, the constants in the Nusselt number equation, c and m are modified to fit the TTA calibration for selected cells (cells 13 - 15). These cells are selected because they are used in experimentation with the velocity gradient (see Chapter 5.5). The Reynolds regime of the modified Nusselt number is valid for $1 \leq Re \leq 185$.

The determination of the constants is done through an iterative process. The initial guess is based off the analytical time constant for uniform flow (see Appendix B.3 for the derivation),

$$1/\tau = ln\left(cRe^{m}\right) = m\ln(Re) + ln(c). \tag{4.8}$$

The calibration provides both the time constant and the uniform velocity (thus the corresponding Reynolds number). Plotting the inverse time constant against the natural log of the corresponding Reynolds numbers determines the initial values for c and m as the slope and intercept. The iterative process then continues until there is reasonable agreement between the calibration fit and numerical simulation.

The simulated calibration curve along with the TTA fit and data for cell 13 is shown in Figure 4.2 (see Appendix A for cells 14 - 15). The constants for cells 13 - 15 along with the calculated uncertainty (determined using Equation 3.1) are shown in Table 4.2.

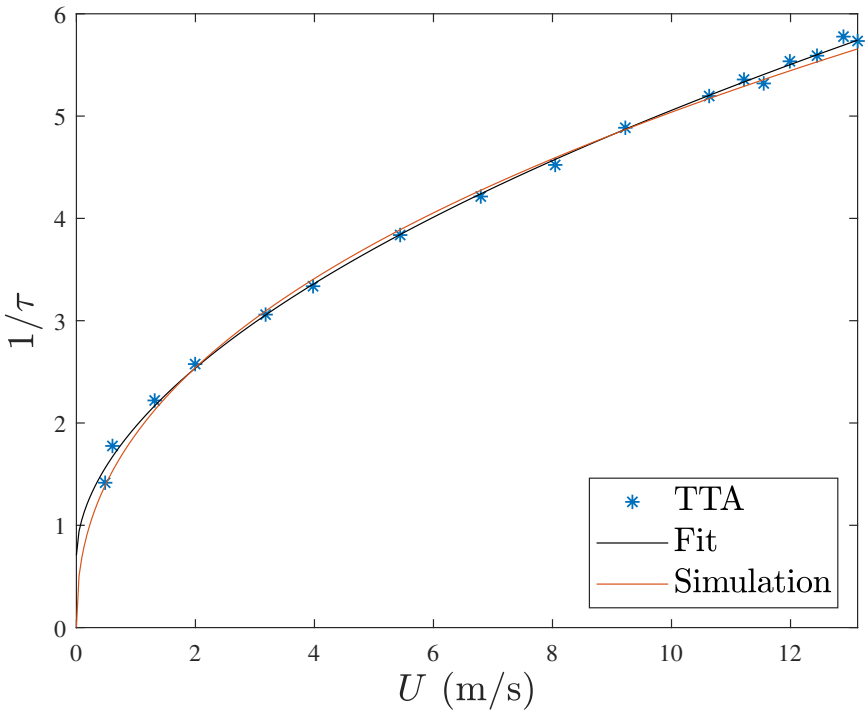

Figure 4.2: Cell 13 experimental and simulated calibration

Cell Number	c	m	Uncertainty (m/s)
13	0.778	0.425	0.1579
14	0.784	0.422	0.1202
15	0.785	0.424	0.1897

Table 4.2: Constants in Nusselt correlation for cells 13 - 15

4.2.2 Numerical and Analytical Methods for Determining the Time Constant

Two methods for computing the time constant are available; numerical and analytical. In the numerical approach, the dimensionless resistance from Equation 1.1 is used to compute the time constant. This process involves plotting the dimensionless resistance, R^*, as a function of time, to identify the rate of decay as the time constant (likewise the slope in the evaluation of $log(R^*)$ is also characteristic of the time constant). In the analytical approach, the governing equation (Equation 4.1) is used to write the thermal properties as a function of the time constant to directly solve for the time constant, τ.

For the simulations, the numerical approach is utilized to compute the time constant. However, the validation of the simulation is done by computing the time constant for uniform flow both numerically and analytically to ensure they are equivalent.

In uniform flow, the thermophysical properties along the wire are approximately constant, thus the governing equation simplifies to,

$$1/\tau = ln\left(\frac{4h(t)}{\rho C_p D}\right). \tag{4.9}$$

The derivation of Equation 4.9 is in Appendix B.3.

Uniform velocities ranging from 0.1 to 15 m/s are simulated and the time constants are determined numerically and analytically. This is shown in Figure 4.3. The calculated percent difference between the numerical and analytical computations is nominally $\pm 0.5\%$. The small difference is due to the analytical time constant being evaluated at the final instant only. The agreement in the numerical and analytical solutions serves as a validation of the simulation.

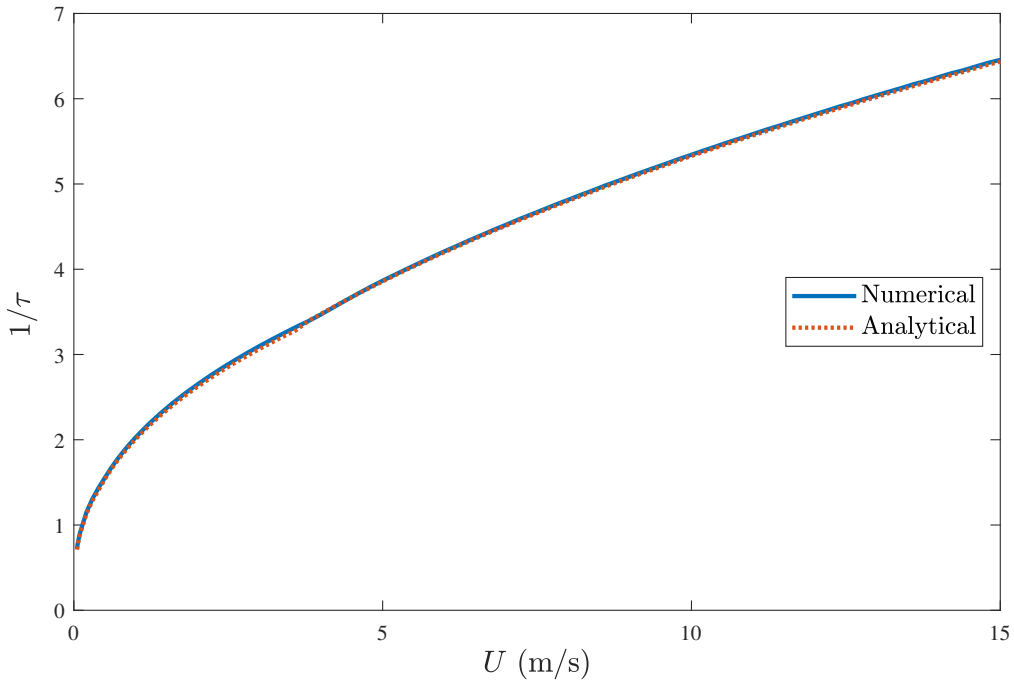

Figure 4.3: Comparison of numerical and analytical methods of solving for the time constant

4.2.3 Natural and Forced Convection

Traditional heat transfer classifies convection as either natural (also referred to as free) or forced, based on how the fluid motion is initiated. In forced convection the fluid motion is initiated by an outside source such as a pump, moving body, etc. In the case of the TTA, the velocity passing over from an outside source is forced. Natural convection is driven by outside factors such as buoyancy (hot fluid rising while cooler fluids fall). Natural convection is always present when there is a temperature gradient, however it is often neglected in the presence of the more dominant forced convection. Cengel and Ghajar [5] suggest that natural convection can be neglected when $Gr/Re^2 < 0.1$, where Gr and Re represents the Grashof and Reynolds number. This ratio, Gr/Re^2, is referred to as the Richardson number.

The Richardson number for the TTA with velocities ranging from 0 to 15 m/s is shown in Figure 4.4, where the threshold Richardson number for consideration of free convection effects ($Gr/Re^2 = 0.1$) is noted. For velocities ≤ 0.06 m/s, the Richardson number suggests that both natural and forced convection should be considered. However, since the range of interest for the TTA is between 0.1 m/s to 15 m/s, the effects of free convection are neglected in the simulation.

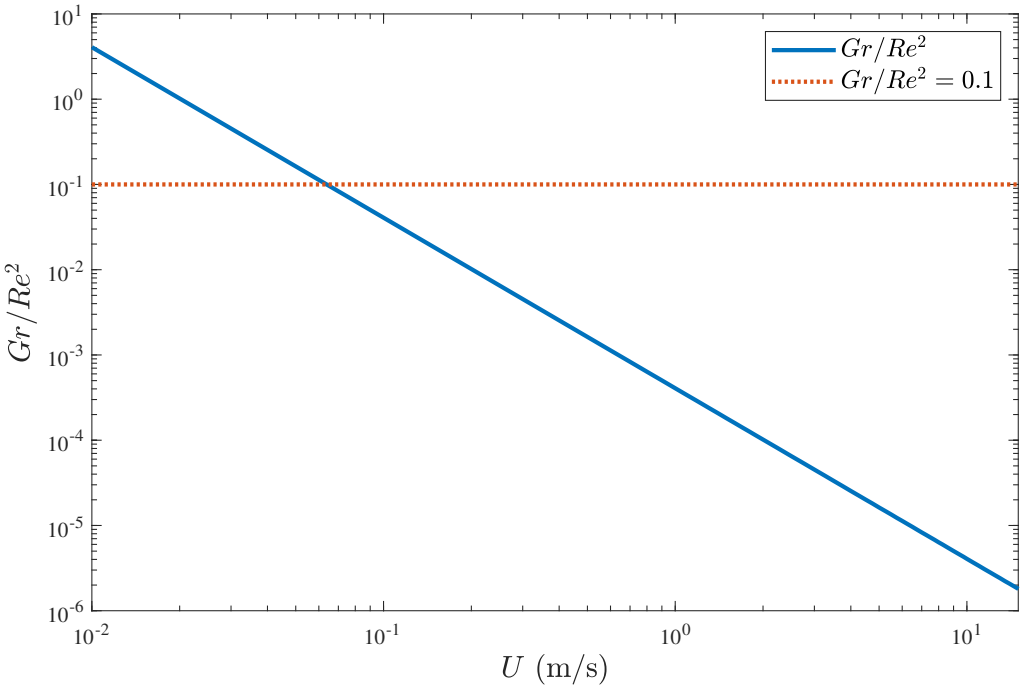

Figure 4.4: Richardson number for velocities ranging from 0 m/s to 15 m/s

CHAPTER 5

PERFORMANCE OF TTA WITH LINEAR VELOCITY GRADIENTS

The response of the sensing wire in a TTA cell when exposed to a linear velocity profile (uniform gradient) is evaluated through numerical simulations and experimentation. The TTA is calibrated with a set of uniform velocities, in which the temperature and thermal properties along the wire are approximately uniform. With the imposition of a linear velocity profile, the temperature and thermal properties along the wire are nonuniform, impacting the temporal response of the sensing wire to the nonuniform flow. It is of interest to study whether the TTA device subjected to nonuniform flow will return the correct mean velocity using the uniform velocity calibration. The performance of the TTA device is characterized by the error between the mean velocity it measures and that which is imposed, with and without a velocity gradient.

5.1 Defining the Velocity Gradient

It is expected that nonuniformities in the flow will be more impactful on the TTA response at low mean velocities than at higher mean velocities. Thus, it is of interest to scale the velocity gradient to obtain a dimensionless parameter to reflect the relative strength of the gradient. A linear velocity profile is considered such that there is some minimum and maximum velocity at either end of the cell, with some mean velocity ($U_{mean} = (U_{min} + U_{max})/2$). This mean velocity is compared to the inferred velocity provided by the TTA measurement. The dimensionless uniform velocity gradient, dU^*/dx^*, is defined as,

$$\frac{dU^*}{dx^*} = \frac{U_{max} - U_{min}}{U_{mean}}. \tag{5.1}$$

The derivation of the gradient is shown in Appendix B.4.1. For the present TTA frame, each cell contains the same length sensing wire, of 1.6 m. A schematic of the linear velocity profile is shown in Figure 5.1. Note that the velocity profile varies uniformly in the x-

direction; there is no variation in the y-direction. Therefore, the portion of the wire which is strung vertically does not vary in velocity magnitude.

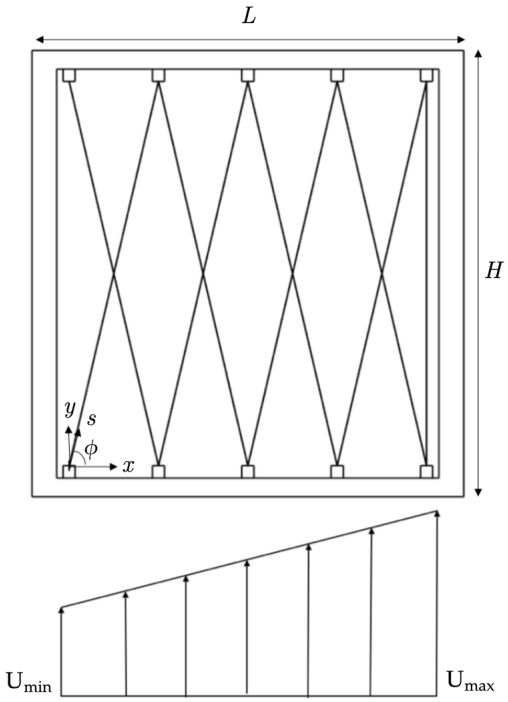

Figure 5.1: Schematic of linear velocity profile imposed on the TTA cell

Mean velocities ranging from 0.1 to 15 m/s with dimensionless gradients ranging from 0 to 1.9 are simulated for cells 13 - 15. The range of gradients simulated correspond with the measurement capabilities of the TTA; reverse or negative flow is not considered since the TTA cannot determine the flow direction. It should be noted that dimensionless gradients exceeding 1.0 are considered extreme and are not expected to be encountered in typical applications.

5.2 Simulating a Linear Velocity Gradient

The effects of the linear velocity gradient are explored for cells 13 - 15, but for illustration purposes the figures presented in this section are representative of cell 13.

To observe how the gradient affects the resistance decay and time constant, mean veloc-

ities of 1, 5, and 10 m/s with and without gradients of 0.5, 1.0, and 1.9 are simulated. The temperature decay for the following scenarios is shown in Figure 5.2. For a gradient of 0.5 (Figure 5.2a), the wire decay is slightly faster with a gradient than without. As the strength of the gradient increases to 1.0 and 1.9, the wire starts to decay at a slower rate (Figures 5.2b - 5.2c). This is most evident with the gradient of 1.9 in Figure 5.2c. This generally holds true regardless of mean velocity.

The computed time constants, inferred velocities, and percent differences for the simulated flow conditions in Figure 5.2 are listed in Table 5.1. The percent difference refers to the difference between the inferred velocity from the TTA calibration (from the time constant and Equation 1.2) and the mean velocity imposed in the simulation.

In the existence of smaller gradients (demonstrated by a gradient of 0.5), the inferred mean velocity is nominally 1.25% higher than the simulated mean velocity for the cases of 1, 5, and 10 m/s. With the existence of larger gradients ($dU^*/dx^* \geq 0.5$), the percent difference approaches 13% due to the under-prediction of the mean velocity. The higher mean velocities are most affected by the strong gradient, as noted by the percent difference. The percent difference ranges from 10.10% for the mean velocity of 1 m/s to 12.30% for the mean velocity of 10 m/s.

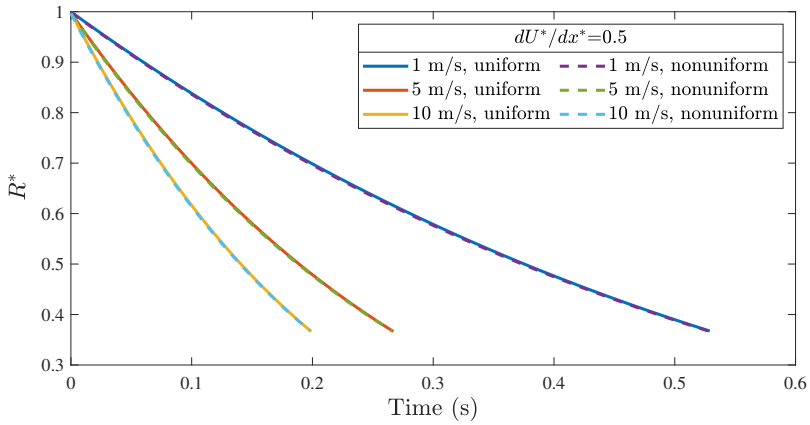

(a) Gradient of 0.5

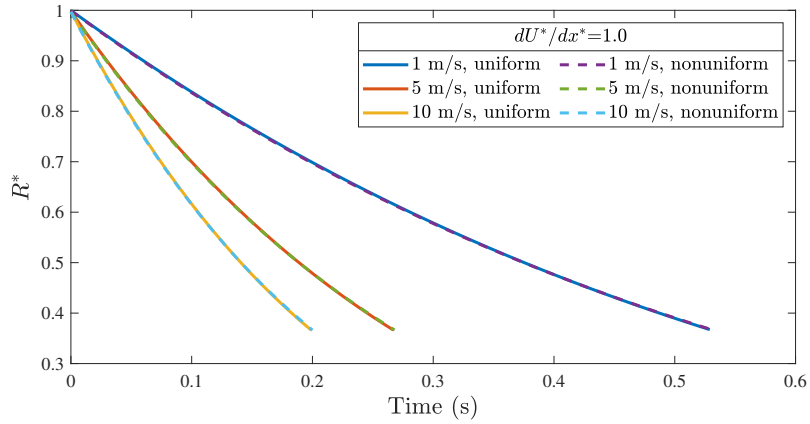

(b) Gradient of 1.0

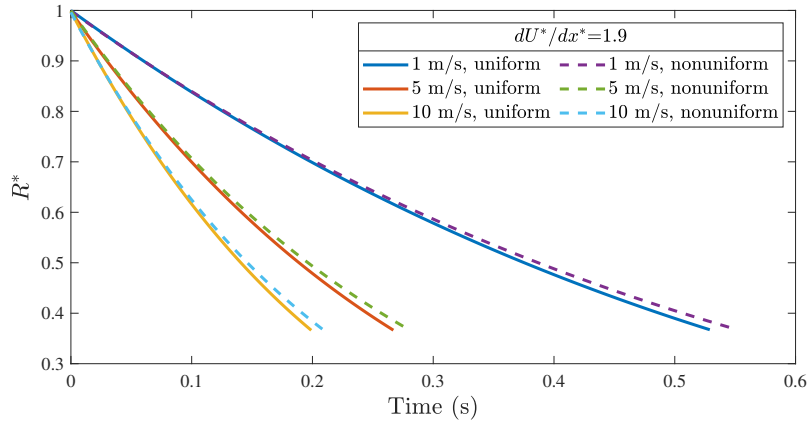

(c) Gradient of 1.9

Figure 5.2: Resistance decay of wire with and without various gradients for mean velocities of 1, 5, and 10 m/s

Mean Velocity (m/s)	Gradient	Inverse Time Constant (1/s)	Inferred Mean Velocity (m/s)	Percent Difference (%)
1	0	1.89	-	-
	0.5	1.90	1.01	1.34
	1.0	1.88	0.98	1.90
	1.9	1.81	0.89	10.10
5	0	3.75	-	-
	0.5	3.77	5.06	1.28
	1.0	3.72	4.92	1.54
	1.9	3.57	4.44	11.24
10	0	5.04	-	-
	0.5	5.06	10.12	1.16
	1.0	4.99	9.80	1.94
	1.9	4.78	8.77	12.30

Table 5.1: Time constants and computed velocities for uniform and nonuniform cases

The slow temperature decay with the existence of a velocity gradient is evident based on the varying temperature distribution. Using the simulation, mean velocities of 1 and 5 m/s with gradients of 0.5, 1.0, and 1.5 are evaluated to observe the temperature distribution during the cooling period. The temperature distribution along the wire at various time steps is shown in Figure 5.3. The initial time stage (0 ms) represents the wire after it has been heating and is about to begin the cooling process. The final time stage represents the time at which $R^* = e^{-1}$, which varies depending on the case. Each time step is spaced evenly apart. Areas of high relative velocity are in the 'center' of the wire, noted by lower temperature values, while areas of low relative velocity are on either endpoint, noted by higher temperature values.

In Figures 5.3a - 5.3b a gradient of 0.5 is simulated for mean velocities of 1 and 5 m/s respectively. The effect of the dimensionless gradient is approximately the same for both mean velocities simulated. At the initial time step, the temperature variation along the wire (difference between maximum and minimum temperature at a given time) is 2.3°C and 4.6°C for the mean velocities of 1 and 5 m/s. At the final time step, the temperature variation along the wire for 1 and 5 m/s is 15.3°C and 16.2°C. At this gradient magnitude, the temperature

distribution along the wire takes an approximately linear profile as it cools for both mean velocities. In Figure 5.3c, the mean velocity is 5 m/s with a gradient is 1.0. At this gradient, the temperature takes a nonlinear distribution as it continues to cool, most evident in the final time step. At the final stage, the temperature variation along the wire is 34.3°C. This effect is more pronounced as the gradient increases as shown in Figure 5.3d (mean velocity of 5 m/s with a gradient of 1.5). The temperature distribution is immediately nonlinear, with the final temperature variation being 57.9°C. As the magnitude of the dimensionless gradients increase, the total temperature variation increases. In the existence of strong gradients, the temperature distribution becomes nonlinear and the temperature variation increases. This generally holds true for all mean velocities.

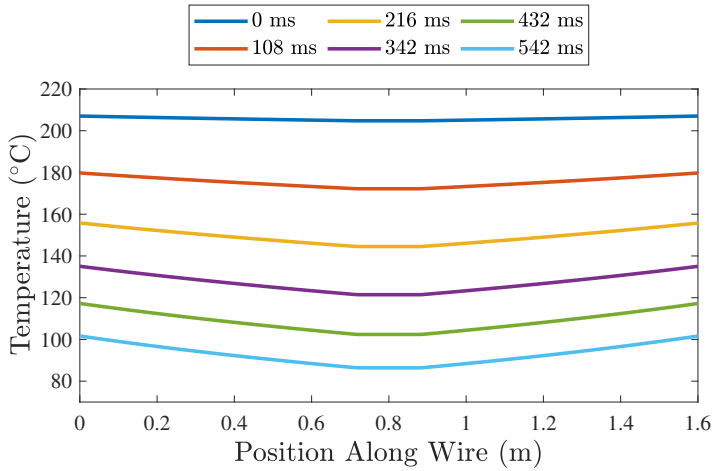

(a) Mean velocity of 1 m/s and gradient of 0.5

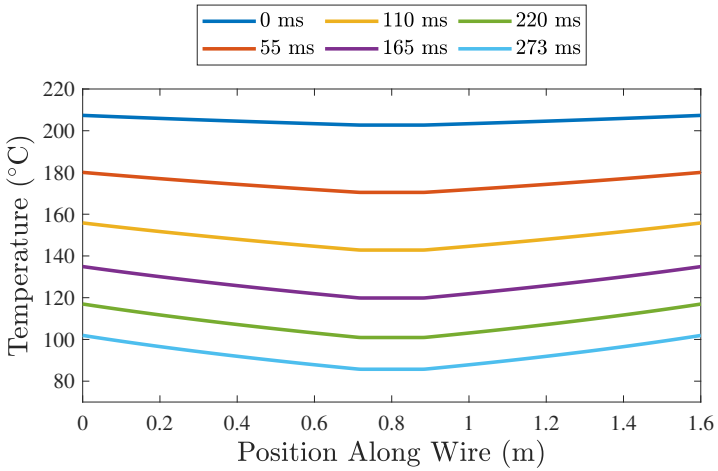

(b) Mean velocity of 5 m/s and gradient of 0.5

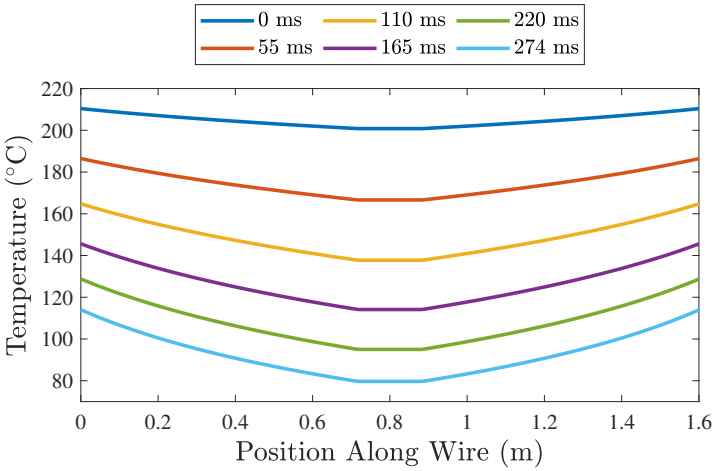

(c) Mean velocity of 5 m/s and gradient of 1.0

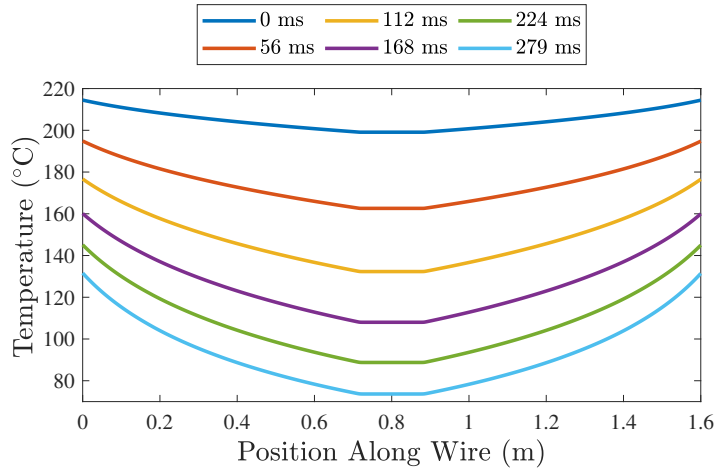

(d) Mean velocity of 5 m/s and gradient of 1.5

Figure 5.3: Temperature distribution along wire at subsequent time steps for various mean velocities and gradients

The percent error due to the uniform velocity gradient for all mean velocities (0.1 to 15 m/s) and gradients (0 to 1.9) is shown in Figure 5.4. The percent difference is noted by the color, with blue being a low percent difference and yellow being a high percent difference. For small gradients between 0.4 to 0.5, the percent difference is around 1% for all mean velocities. The error increases as the strength of the gradient increases. At extreme gradients between 1.5-1.9, the error goes from 4% to above 12%, with the higher mean velocities having the largest error. The error starts to propagate when the dimensionless velocity gradient surpasses a magnitude of 0.4 for most mean velocities ($U \geq 4$ m/s).

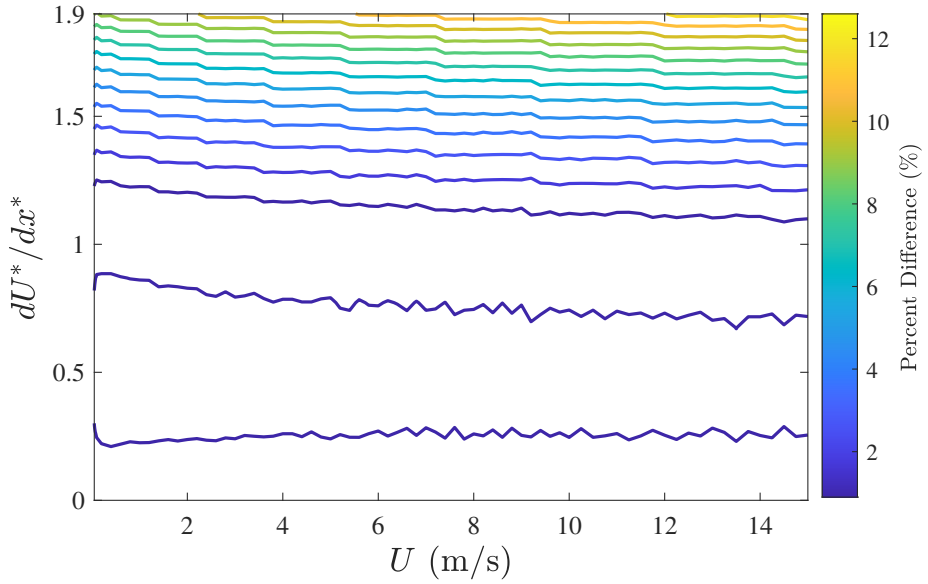

Figure 5.4: Percent difference in TTA measurements for various mean velocities and gradients

The resistivity of the TTA sensing wire is temperature dependent. The resistivity varies linearly with temperature and is used directly in the computation of resistance (Equation 4.3). For this reason, the resistivity profiles for a mean velocity of 5 m/s at various velocity gradients (0, 0.5, 1.0, 1.5) are simulated. Contour plots of the resistivity profiles along the wire during the cooling period are in Figure 5.5. When the velocity is perfectly uniform, the resistivity profile is constant as observed and expected in Figure 5.5a. With a dimensionless velocity gradient of 0.5, the resistivity profile is nominally linear, as seen in Figure 5.5b. At

this stage, the error is just above 1% for the mean velocity of 5 m/s. When the gradient reaches 1.0 and 1.5, the resistivity profile is extremely nonlinear due to the imposed velocity profile as seen in Figures 5.5c - 5.5d.

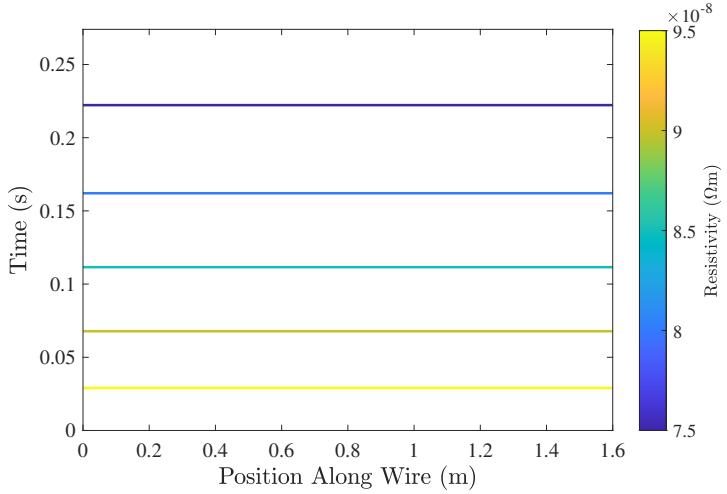

(a) Perfectly uniform case

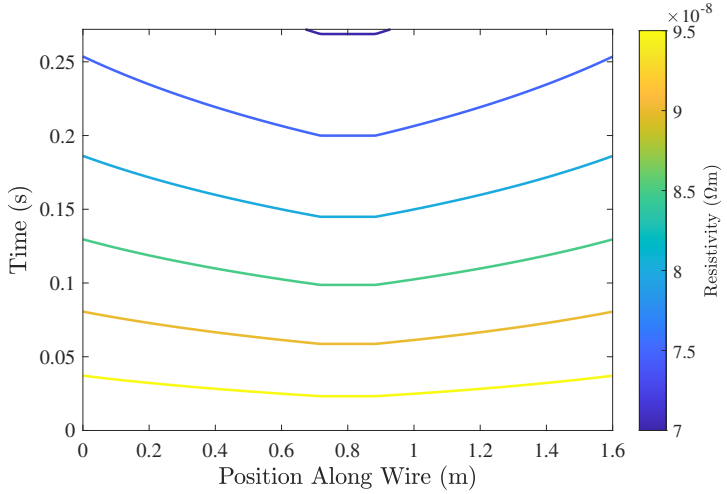

(b) Gradient of 0.5

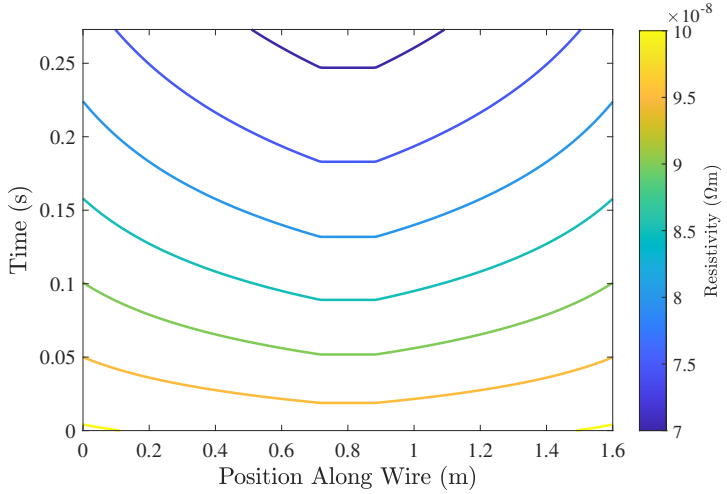

(c) Gradient of 1.0

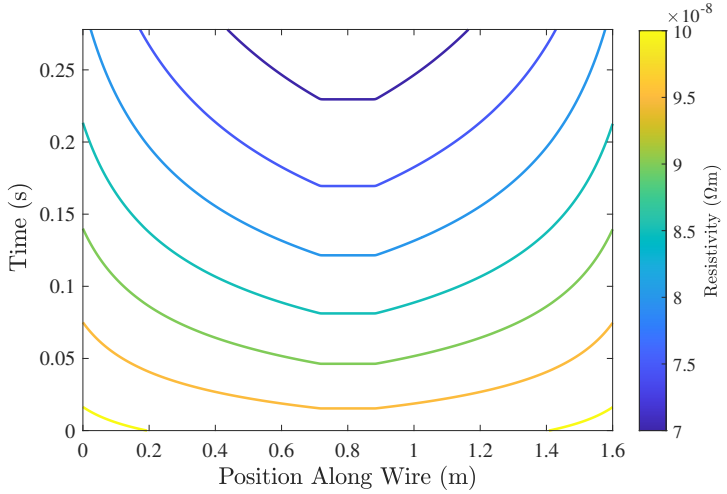

(d) Gradient of 1.5

Figure 5.5: Resistivity along wire as it convectively cools for a mean velocity of 5 m/s with various velocity gradients

5.3 Simulating a Linear Velocity Gradient Along the Height of the TTA Cell

The velocity gradient, dU^*/dx^*, in Section 5.2, considers a velocity profile with variation along the cell length (horizontal velocity gradient). The same linear velocity profile is considered with variation along the cell height instead of the length. This vertical velocity gradient, dU^*/dy^*, is defined as,

$$\frac{dU^*}{dy^*} = \frac{(U_{max} - U_{min})}{U_{mean}}. \tag{5.2}$$

The derivation of the vertical velocity gradient is shown in Appendix B.4.2. A schematic of the vertical velocity gradient is shown in Figure 5.6.

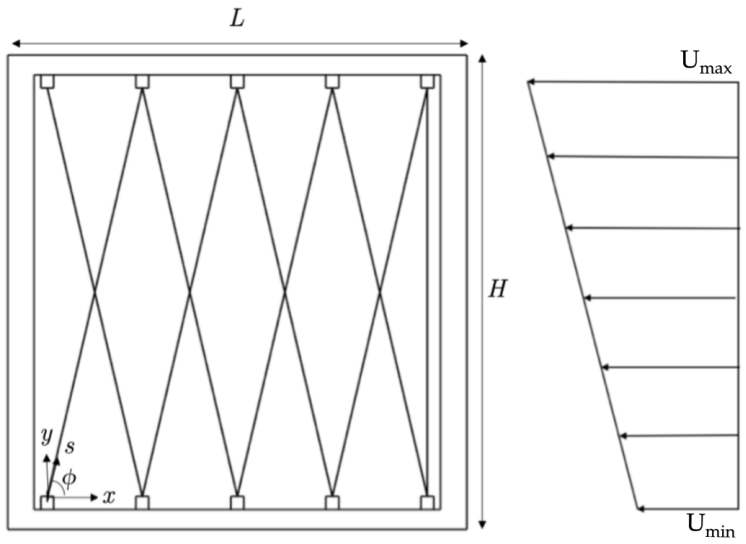

Figure 5.6: Schematic representation of linear velocity profile imposed on the TTA cell (varying along the height)

The same mean velocity and gradient range is considered (mean velocities ranging from 0.1 to 15 m/s, gradients ranging from 0 to 1.9). The velocity along the wire length, s, when the horizontal and vertical gradients are imposed is shown in Figure 5.7 (mean velocity of 10 m/s, gradient of 0.5 simulated). Note that the maximum and minimum velocities are the same, since the same magnitude gradient is imposed. The velocity along the wire when the

gradient dU^*/dy^* is imposed, varies in accordance to the vertical positioning of the wire. It reflects the multi-X pattern in which the wire is strung.

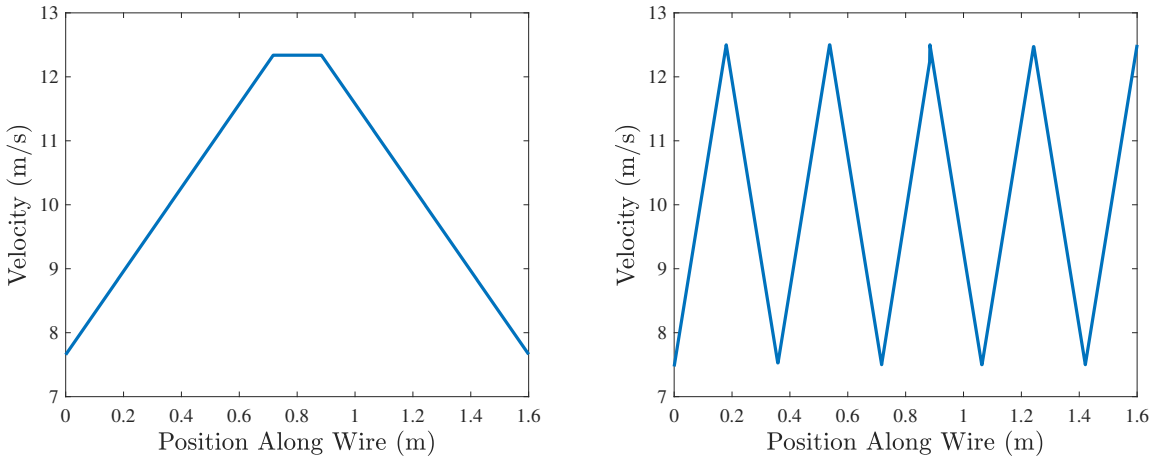

(a) Velocity gradient imposed along the length of TTA cell (dU^*/dx^*)

(b) Velocity gradient imposed along the height of TTA cell (dU^*/dy^*)

Figure 5.7: Velocity along the sensing wire for a mean velocity of 10 m/s and gradient of 0.5

Let ξ represent the gradient (in the horizontal or vertical orientation). For the TTA cell (length of 154 mm and height of 166 mm), the relative velocity along the sensing wire varies based on the gradient orientation. Consider a position along the sensing wire, s, such that,

$$0 \leq s \leq \frac{H}{\sin(\phi)} \tag{5.3}$$

where $\phi = 78.38°$. When a gradient, ξ, is imposed, the relative velocity, U, based on the position along the wire, s, is,

$$U = \begin{cases} U_{min} + \xi \dfrac{U_{mean}}{L} s\cos(\phi) & \text{horizontal gradient} \\ U_{min} + \xi \dfrac{U_{mean}}{H} s\sin(\phi) & \text{vertical gradient} \end{cases} \tag{5.4}$$

where the relative velocity at the position along the wire (when the gradients and mean velocities are equivalent) is always larger when a vertical gradient is imposed than when a horizontal gradient is. This indicates that there are larger velocity fluctuations within a given segment of the sensing wire when a vertical gradient is imposed (see Figure 5.7). Note that for a given mean velocity gradient, the minimum and maximum velocities across the

cell are equivalent for both horizontal and vertical positions. The relative velocities vary between the minimum and maximum velocity ($U_{min} \leq U \leq U_{max}$).

The percent error due to the vertical velocity gradient for all mean velocities (0.1 to 15 m/s) and gradients (0 to 1.9) is shown in Figure 5.8. For small gradients, less than 0.4, the percent difference is less than 1%. This error increases as the gradients increase to 1.9, where the error approaches 24%. The percent error is higher when the velocity gradient is imposed along the height of the TTA cell due to the pattern in which the sensing wire is strung and the resulting velocity along the wire.

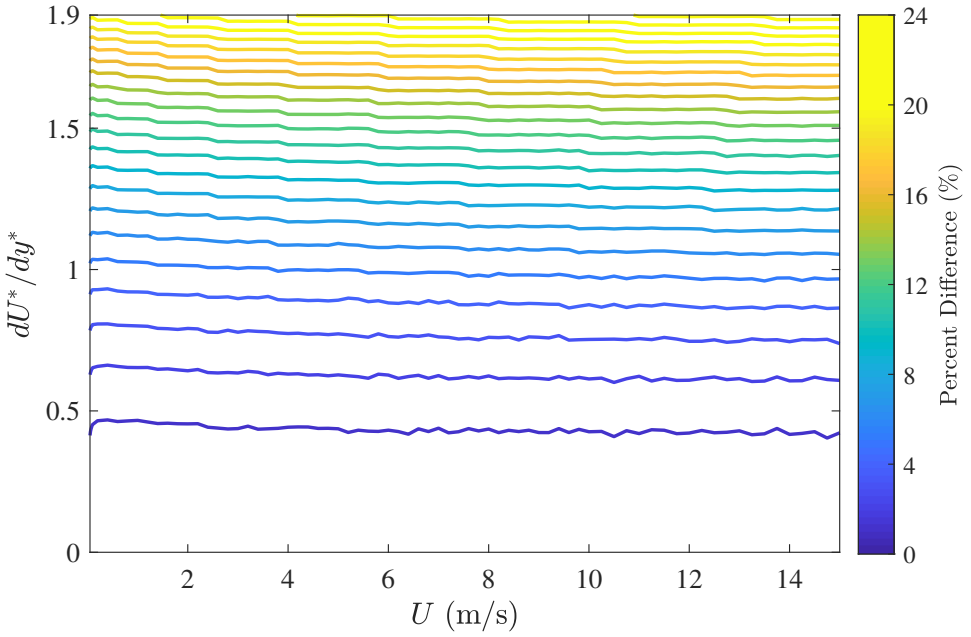

Figure 5.8: Percent difference in TTA measurements for various mean velocities and vertical gradients

In Figures 5.9a - 5.9d horizontal and vertical gradients of 0.5 and 1.0 are simulated for a mean velocity of 5 m/s. At a gradient of 0.5, the temperature distribution is linear for the horizontal gradient case (as established in Section 5.2). The temperature profile for the vertical gradient of 0.5 is nominally linear as shown in Figure 5.9b. At the final time step, the temperature variation along the wire for the horizontal and vertical gradients are 15.3°C and 17.5°C respectively. As observed with the horizontal gradient, the temperature distribution

starts to become nonlinear as the gradient increases. This is shown in Figure 5.9d, where the vertical gradient is 1.0. For the horizontal and vertical gradients of 1.0, the final temperature variation is 34.3°C and 37.4°C respectively. The larger temperature variation corresponds with a higher percent difference for a given gradient and mean velocity as shown in Figure 5.8. This generally holds true for all gradients and mean velocities.

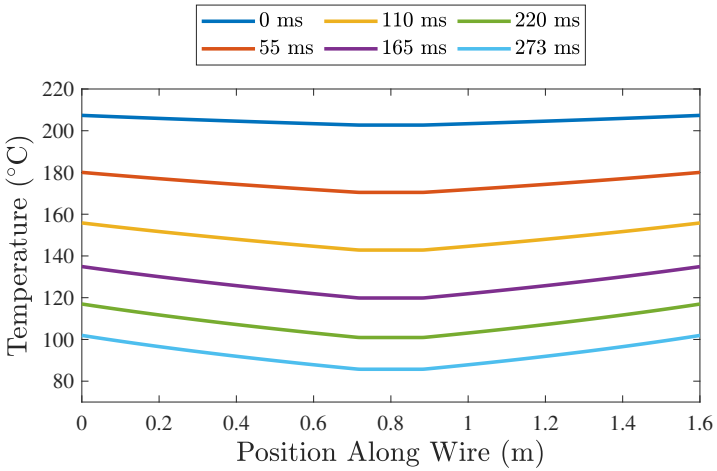

(a) Mean velocity of 5 m/s and horizontal gradient of 0.5

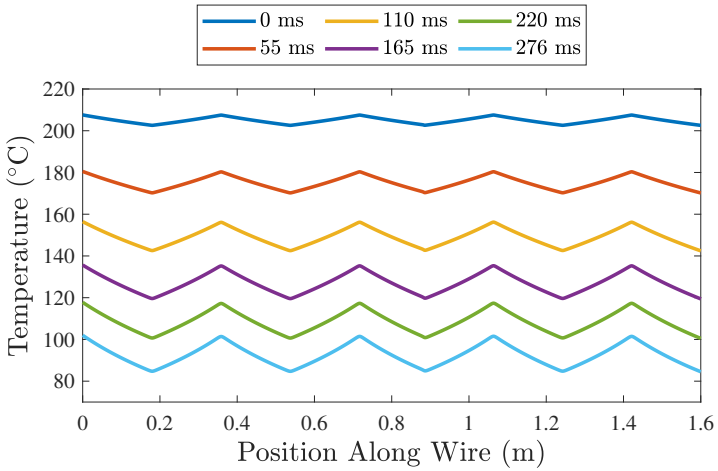

(b) Mean velocity of 5 m/s and vertical gradient of 0.5

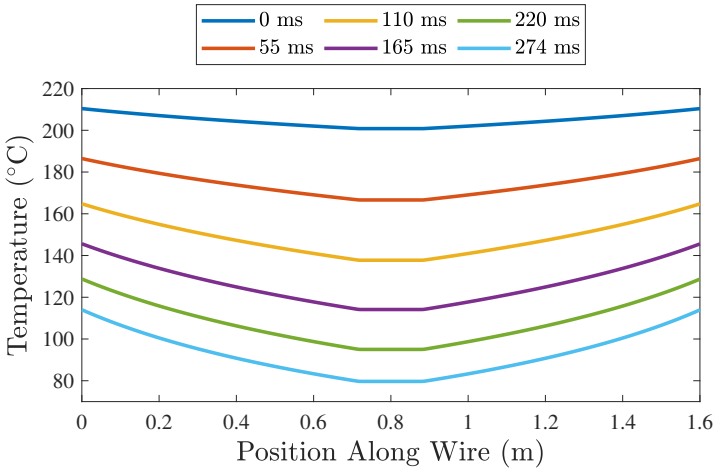

(c) Mean velocity of 5 m/s and horizontal gradient of 1.0

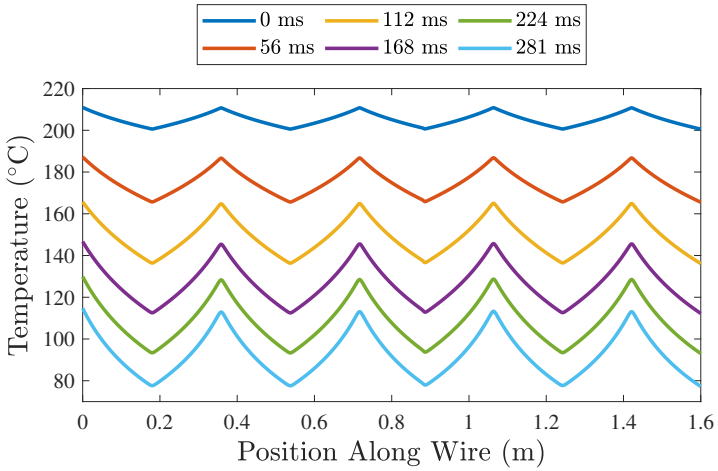

(d) Mean velocity of 5 m/s and vertical gradient of 1.0

Figure 5.9: Temperature distribution along wire at subsequent time steps for various mean velocities and gradients

5.4 Correction Scheme

The imposition of a uniform velocity gradient on the TTA cell introduces error of 1% in the mean velocity measurements when the gradient surpasses 0.4. This error reaches 24% with a mean velocity of 15 m/s and extreme vertical gradient of 1.9.

A correction scheme, developed using the numerical simulations, is implemented to reduce the error when large gradients are present. The nonuniform time constant can be decomposed into a uniform component and an incremental components,

$$\tau_n = \tau_u + \Delta\tau \tag{5.5}$$

where subscripts n and u denote the nonuniform and uniform time constants. By quantifying the value of the incremental component, $\Delta\tau$, the measured nonuniform component can be used to determine the uniform component in Equation 5.5. It is hypothesized that incremental component, $\Delta\tau$ is a function of the dimensionless gradient and mean velocity, $\Delta\tau = f(\xi, U)$. A proposed correlation scheme is,

$$\Delta\tau = \left[\alpha_1 * U^{\beta}1\xi^2 + \alpha_2 * U^{\beta}2\xi + \alpha_3 * U^{\beta}3\right]^{-1} \tag{5.6}$$

where constants α_i and β_i $(i = 1, 2, 3)$ are dependent on the cell number. The specific constants for the simulated cells are shown in Table 5.2. The uniform component of the time constant can be computed as,

$$\tau_u = \tau_n - \Delta\tau \tag{5.7}$$

and used with the uniform calibration to determine the mean velocity within ±1%.

Cell Number	Gradient Orientation	α_1	β_1	α_2	β_2	α_3	β_3
13	Horizontal	0.0491	0.4816	-0.0575	0.4488	0.0044	0.4920
13	Vertical	0.0605	0.4797	-0.0304	0.4912	0.0073	0.4951
14	Horizontal	0.0489	0.4784	-0.0572	0.4466	0.0042	0.5037
14	Vertical	0.0602	0.4782	-0.0303	0.4916	0.0072	0.4990
15	Horizontal	0.0496	0.4801	-0.0581	0.4465	0.0044	0.4894
15	Vertical	0.0611	0.4781	-0.0312	0.4840	0.0076	0.4772

Table 5.2: Correction constants

The correction scheme is applied over the entire test range of mean velocities and gradients considered (mean velocities from 0.1 to 15 m/s and gradients from 0 to 1.9). The calculated error with and without the correction is shown in Figure 5.10. Note the scales for the percent difference vary (the scale without the correction goes to 12% for the horizontal gradient and 24% for the vertical gradient, while the scale with the correction only goes to 3%). With the correction implemented, the TTA measurement error is within 1% for the majority of mean velocities and gradients considered, with the exception of low mean velocities (0.1 to 1 m/s with gradients exceeding 1.5) at 3%.

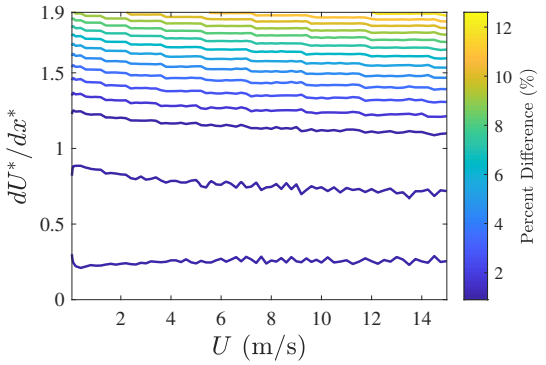

(a) Without correction (horizontal gradient, dU^*/dx^*)

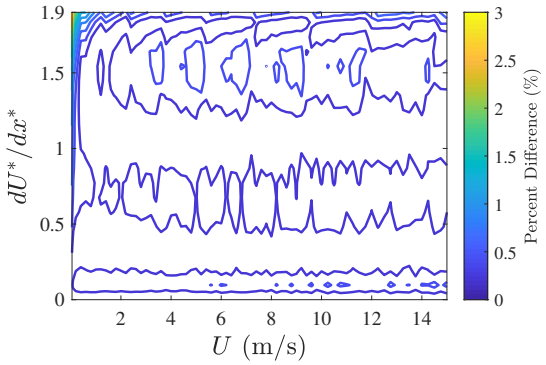

(b) With correction (horizontal gradient, dU^*/dx^*)

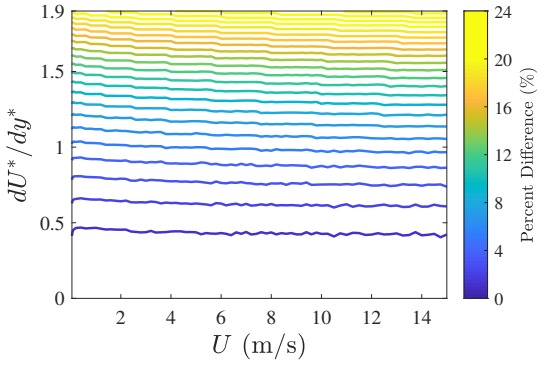

(c) Without correction (vertical gradient, dU^*/dy^*)

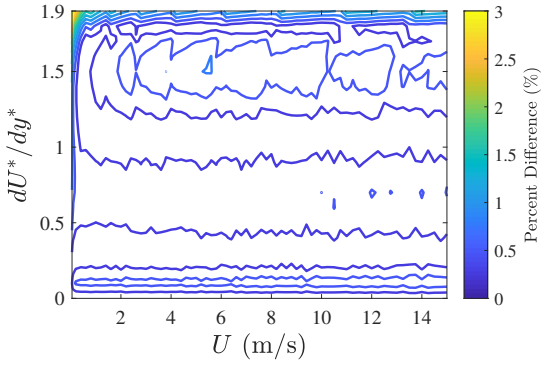

(d) With correction (vertical gradient, dU^*/dy^*)

Figure 5.10: Percent difference in TTA measurements with and without the correction for cell 13

5.4.1 Implementing the Correction Scheme

In practical applications, the TTA can be used to accurately determine the mean velocity with the existence of large velocity gradients, using the correction scheme. The protocol for implementing the correction scheme and determining the mean velocity is as follows:

1. Utilize the TTA frame to obtain the time constant for each cell with a specific flow condition
2. Determine the corresponding inferred mean velocities using the calibration equation (Equation 1.2)
3. Plot the inferred mean velocities obtained from each cell against their relative position to estimate a horizontal or vertical gradient
4. Plug the time constant (nonuniform) into the correction scheme (Equations 5.6 - 5.7) to determine the uniform component of the time constant based on the estimated gradient and inferred mean velocity
5. Repeat steps 2 - 4 until the time constant converges

This is easily carried out using an iterative script.

5.5 Experimental Response of the TTA Cell with an Imposed Velocity Gradient

A linear velocity profile is imposed over the length of a TTA cell to validate the correction scheme proposed in the numerical simulation in Section 5.4. For the purpose of validation, three TTA cells are evaluated. These cells are selected based on the following criteria: (i) central location for ease of access and setup and (ii) excellent calibration fit, with a high root mean square fit ($R^2 \geq 0.998$). The chosen cells are cells 13, 14, and 15 (refer to Figure 3.2 for cell locations). Each cell is tested at three different mean velocities with respective horizontal gradients.

A thin, 3D printed mesh is used to impose a velocity profile across the TTA cell. The mesh is designed to create a linearly increasing velocity profile across the cell. The entire mesh is the size of a TTA cell and features several rectangular holes with corresponding areas, A, spaced across the entire mesh. The area of each hole, A, determines the imposed velocity upon exit of the mesh. Thus spacing the holes across the mesh in order of descending area creates the desired linear velocity profile. The velocity distribution from the mesh creates dimensionless gradients between 0.4 - 1.0 based on the incoming flow speed. Before experimental testing, a model of the mesh is first designed and the profile is evaluated using computational fluid dynamics (CFD) software. The mesh is then printed and tested in the AFRD facility. Following the observation of an approximately linear velocity profile through CFD evaluation and experimentation, the mesh is placed upstream of a TTA cell. An image of the mesh is shown in Figure 5.11.

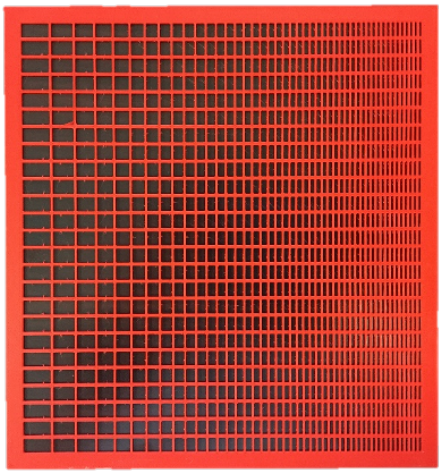

Figure 5.11: Mesh used to impose a linear velocity profile (uniform horizontal gradient)

5.5.1 Determining the Velocity Profile

Ansys Fluent is utilized for the CFD analysis. The oncoming velocity is imposed normal to the mesh at a distance of 5.08 cm (2") away from the mesh. The velocity profile after passing through the mesh is observed at distances of 5.08 - 10.16 cm (2" - 4") downstream.

Contours of the velocity distribution are shown in Figure 5.12. The velocity magnitude (in the x-direction) of the mesh is shown in Figure 5.13.

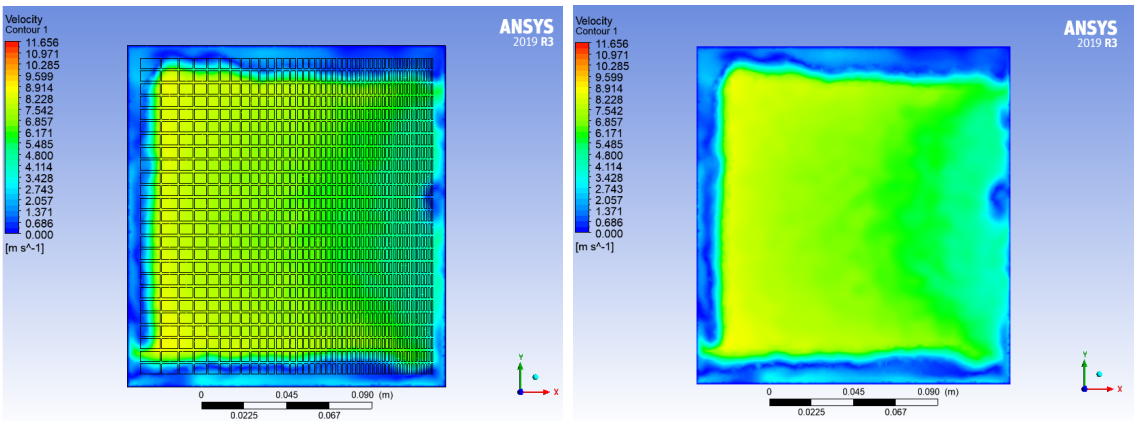

(a) With mesh outline displayed (b) Without mesh outline displayed

Figure 5.12: Fluent analysis of velocity contour 2.08 cm downstream of mesh

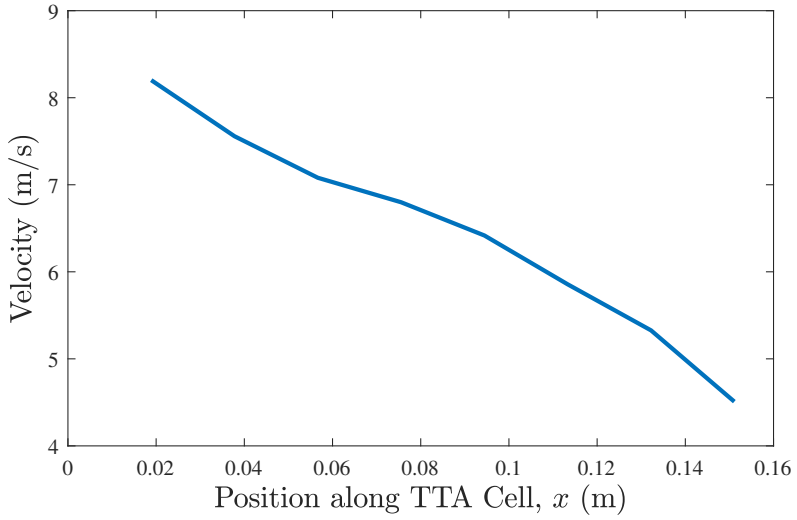

Figure 5.13: Fluent analysis of velocity magnitude 2.08 cm downstream (vertical distance at midpoint height)

From the CFD analysis, the mesh exhibits a near-linear profile. The mesh is then printed using a Prusa 3D printer (with Prusament PLA filament) and tested in the AFRD facility without the TTA. The purpose of testing the mesh alone is to determine the optimal distance downstream which produces the linear velocity profile.

To test the mesh alone, MDF (medium-density fiberboard) with a cutout the size of the mesh (155 mm x 165 mm) is placed at the inlet of the AFRD. Surrounding the mesh, is a sectioned 10.16 cm (4") diameter PVC pipe constructed into a quarter-round to guide ambient air uniformly to the mesh. Underneath the mesh in the upper receiver, a pitot tube is set up to traverse across the length of the mesh. Since the opening at the inlet is so small, the door to the AFRD is cracked to avoid surging. The incoming air from the door did not have an effect on the airflow passing through the mesh, as it is positioned far enough away. The setup of the mesh and pitot tube traverse is shown in Figure 5.14.

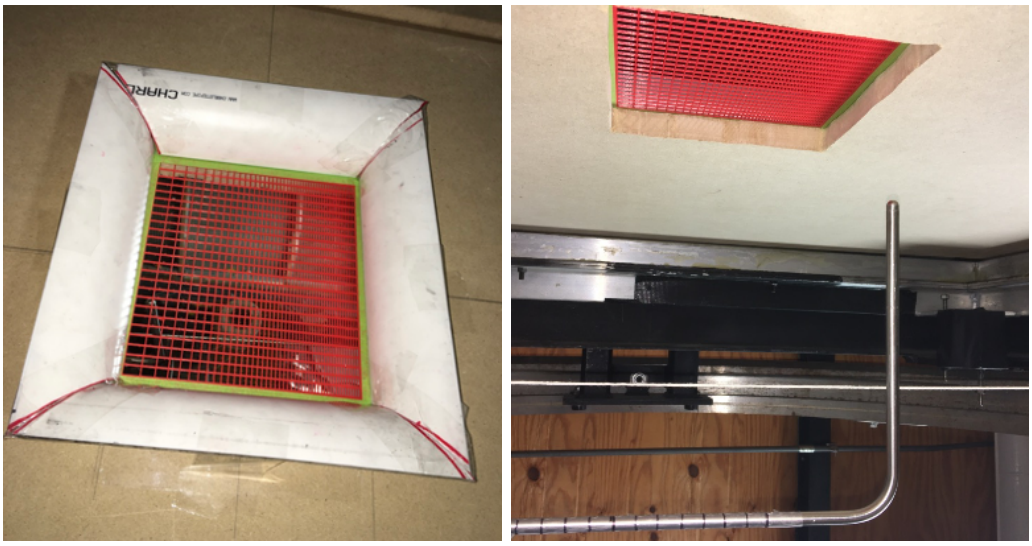

(a) View from top of AFRD (b) View from upper receiver of AFRD

Figure 5.14: Setup for mesh velocity profile measurements using pitot tube

Two velocity settings are tested with the mesh. That is, a high and low inlet velocity with mean velocities of 8.2 and 4.6 m/s respectively. The two velocities are tested at distances of 2.54 - 7.62 cm (1" - 3") away from the mesh. The results from the survey are shown in Figure 5.15.

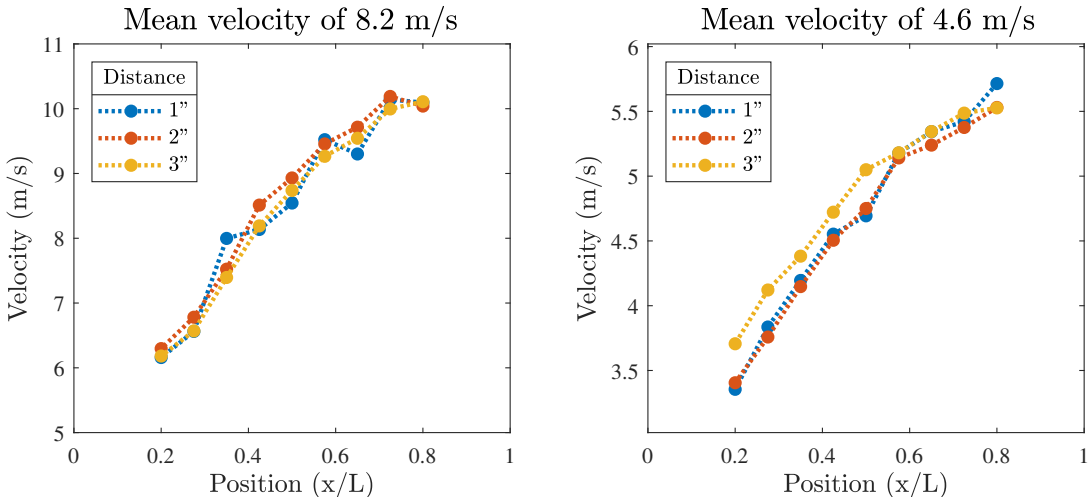

Figure 5.15: Pitot tube determined mesh velocity profile at different distances downstream

Following the pitot tube survey, the results indicate that the mesh produces a stable and a nominally uniform velocity gradient at a distance of 5.08 cm downstream.

5.5.2 Procedure and Results of Experimental Evaluation

For the measurements with the TTA, the setup used in calibration (Section 3.1) is used. The mesh is placed 5.08 cm above a designated TTA cell (13, 14, or 15) with a quarter-round to uniformly guide the air. A cardboard cutout is placed between the TTA and mesh and any gaps are sealed to ensure mass is not lost to leakage. The pitot tube is then placed underneath the assembly to measure the velocity and determine the gradient at the respective inlet condition. The setup is shown in Figure 5.16. Note that the mesh is placed above one TTA cell at a time and not all three cells simultaneously.

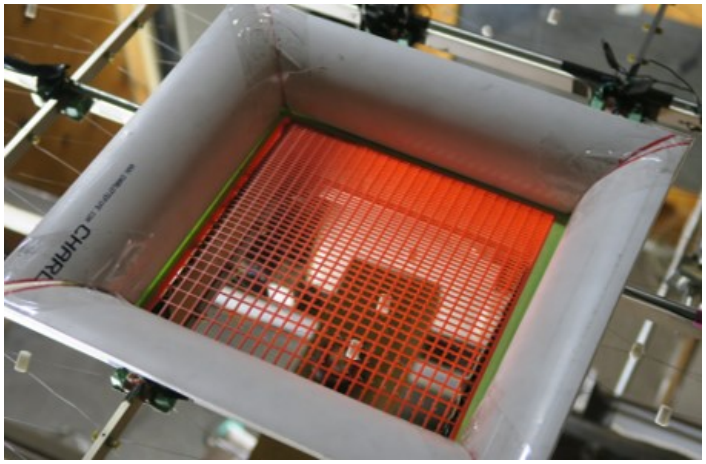

Figure 5.16: TTA with mesh mounted 2.08 cm above tested cell

With the mesh placed above one of the three chosen cells (cells 13 - 15), three different velocities (with respective gradients) are tested. At each velocity, ten successive TTA measurements are taken for each cell. The three mean velocities tested are 3.27 m/s, 6.21 m/s, and 8.93 m/s with respective dimensionless gradients of 0.742, 0.632, and 0.707. The velocity profiles are shown in Figure 5.17.

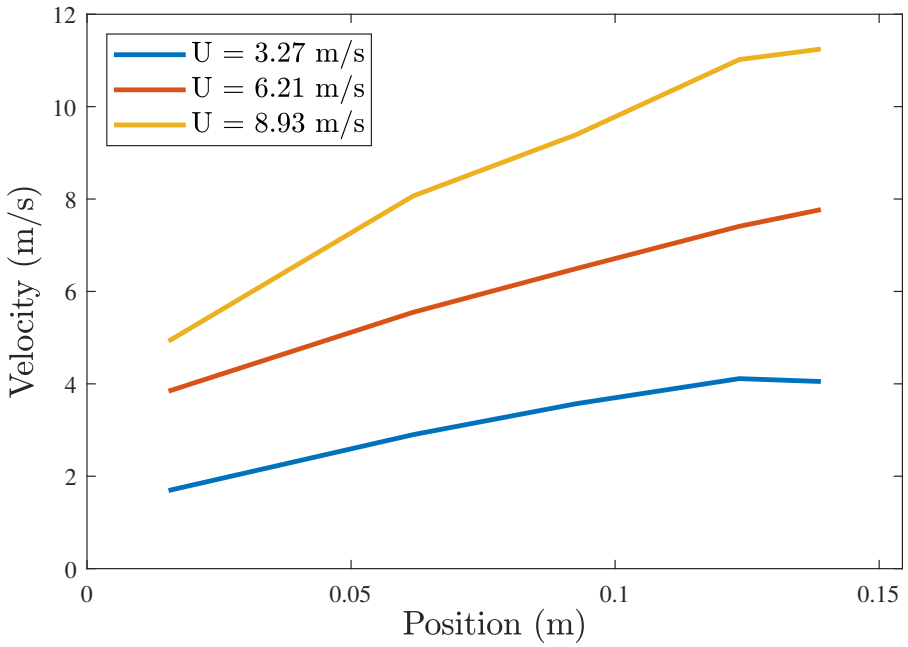

Figure 5.17: Velocity profiles with mesh used for validation of TTA correction scheme

The TTA gradient validation results are listed in Table 5.3. The inferred mean velocity is

calculated using the corresponding time constant and the corresponding calibration equation (Equation 1.2) for the cell. The correction equation (Equation 5.6) is implemented due to the large gradients observed in the three cases. The result is the corrected mean velocity (using the uniform TTA calibration) within 1% of the mean velocity measured using the pitot tube. The application of the correction scheme for all three cells and three different velocity conditions demonstrates the validity of the correction scheme that was formulated using numerical simulations.

Mean Velocity (m/s)	Cell Number	Corrected Inverse Time Constant (1/s)	Inferred Mean Velocity (m/s)	Standard Deviation (10 measurements)	Percent Difference (%)
	13	3.09	3.29	0.040	0.904
3.27	14	3.09	3.28	0.040	0.230
	15	3.18	3.29	0.050	0.605
	13	4.07	6.24	0.146	0.349
6.21	14	4.06	6.19	0.156	0.437
	15	4.16	6.23	0.131	0.279
	13	4.78	8.89	0.153	0.463
8.93	14	4.77	8.91	0.628	0.716
	15	4.87	8.95	0.175	0.229

Table 5.3: Results from gradient validation after correction scheme is applied for all three cells and mean velocities tested

CHAPTER 6

NONUNIFORM VELOCITY DISTRIBUTION AT THE EXIT PLANE OF A RADIATOR

The TTA frame is utilized to interrogate the velocity distribution at the exit plane of an automotive radiator with various installation configurations. The three installation configurations explored are: (i) radiator in the horizontal position, (ii) radiator inclined at 8° with respect to the horizontal, and (iii) radiator inclined at 8° with the shroud attached. These installation configurations are tested with uniform base flow conditions provided by the AFRD facility, ranging from 0.26 to 9.57 m/s.

The horizontal configuration is used as the reference condition. It is used to evaluate the exit velocity distribution when the radiator is installed in a vehicle. The inclined configuration is of interest since it mimics the mounting configuration for the specific vehicle in which the radiator is installed. The packaging constraints for that vehicle require an 8° inclination between the plane of the grill and the plane of the radiator. The inclined and horizontal configurations are compared to observe and quantify the effect of tilting the radiator. For the final configuration, the shroud is attached and the radiator is mounted in the same inclined position. The effect of attaching the shroud is determined by comparing its results to those of the inclined configuration without the shroud.

6.1 Experimental Setup and Procedure

The experimental setup within the AFRD is shown in Figure 6.1. The TTA frame is attached to the back face of the radiator and secured with four 8 mm (5/16") screws (see Figure 1.1a for TTA attached to radiator). A metal frame constructed with 3.81 cm (1.5") aluminum beams is used to support the radiator and TTA frame. The frame and radiator are positioned horizontally with respect to the inlet, facing downward. Sectioned 10.16 cm (4") diameter PVC piping is placed around the perimeter of the radiator as a quarter-round

inlet, to ensure uniform flow. Foam insulation is placed around the frame to seal any gaps and prevent air leakage.

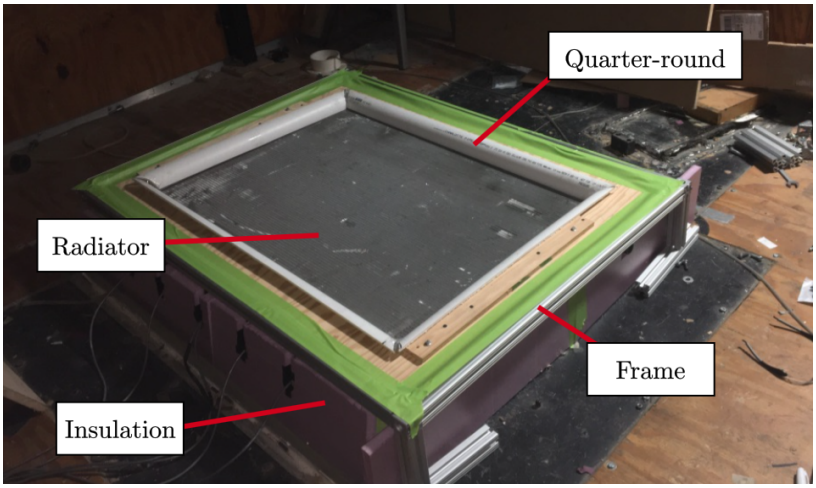

(a) View from on top of AFRD roof

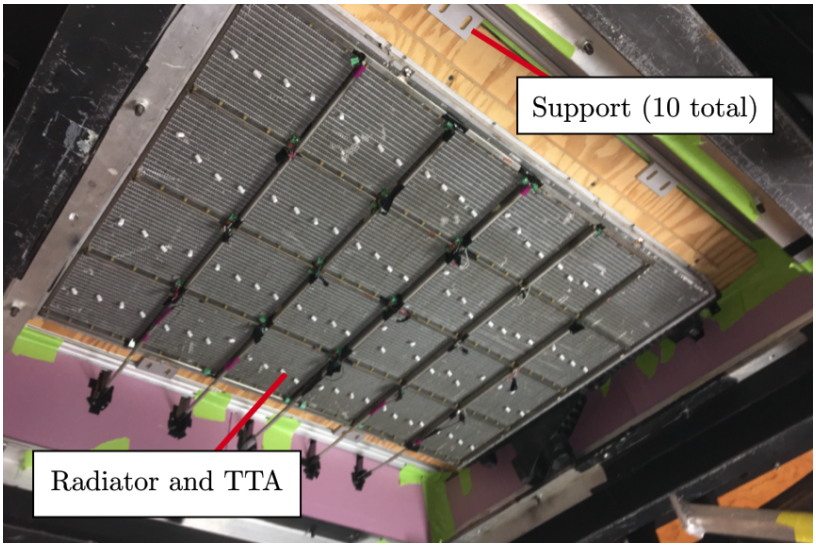

(b) View looking up from upper receiver

Figure 6.1: Radiator and TTA frame installation

In the vehicle, the radiator is hinged along its length to create the 8° inclination angle. Instead of physically inclining the radiator, an inlet channel is utilized to mimic this effect. The inlet channel redirects the flow with respect to the desired position in the vehicle. The central axis on the inlet channel is inclined 8° with respect to horizontal. A honeycomb flow straightener with inner diameter, D, and thickness, L, such that $L/D = 8$ is placed

at the channel inlet. The distance from the honeycomb exit to the radiator (at midpoint) inlet agree with the installation condition of the vehicle, that is a distance of 16.6 cm. The channel design is shown in Figure 6.2.

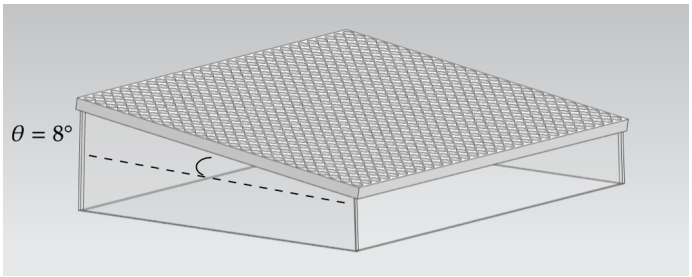

(a) Model of inlet channel

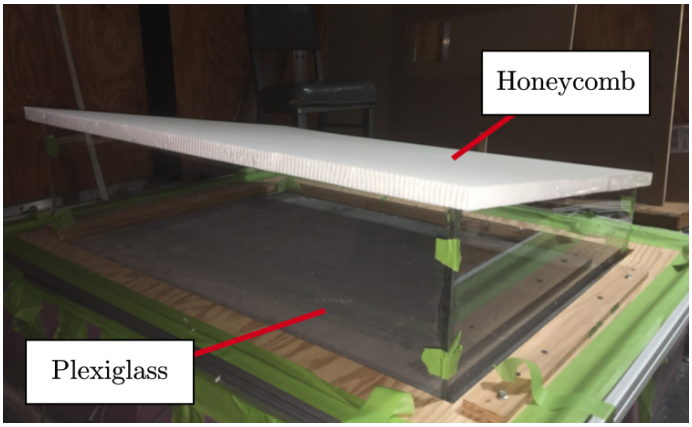

(b) Channel mounted on top of automobile radiator

Figure 6.2: 8° inclination inlet channel

The shroud is attached to the back of the TTA using four screws (8 cm or 5/16"). There is a small gap between the radiator and shroud due to the protruding TTA electrical wires. This along with other gaps are sealed using tape to prevent any leakage. The setup with the shroud is shown in Figure 6.3.

The AFRD fan is utilized to establish a base flow condition. This is measured using the TTA output. For each flow rate, the TTA is used to survey the radiator plane exit distribution. Ten TTA measurements at each velocity are taken. This procedure is repeated for each inlet condition. The inlet velocities tested range from 0.26 m/s to 9.6 m/s, with an emphasis on the lower velocities.

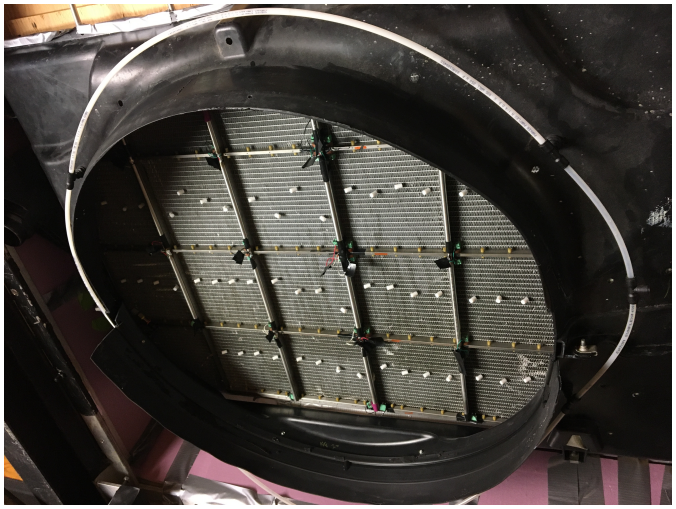

Figure 6.3: Radiator with shroud attached with a view looking up from AFRD upper receiver

Measurements for the horizontal and inclined configurations are taken at each inlet condition by adding and removing the inlet channel. This provides a similar set of inlet velocities in the test range. The results with the addition of the shroud are done separately, after mounting the shroud on the radiator.

6.2 Results

The TTA provides a velocity survey at the exit face of the radiator. The results are analyzed for the three installation configurations (horizontal, inclined, inclined with shroud).

The addition of the inclined entry channel introduces a subtle pressure drop between the atmosphere and honeycomb, not present in the horizontal study. This results in a small reduction in flow rate. Likewise, measurements with the shroud are not taken with the same base flow conditions. When comparing the measured cell velocity to the inlet mean velocity, the difference is normalized by the mean inlet velocity to give a percent difference from the mean as,

$$\Delta_{ijk} = \frac{U - U_{cell}}{U} * 100 \tag{6.1}$$

where the indices *i,j,k* refer to the row ($i = 1, ..., 4$), column ($j = 1, ..., 6$), and installation configuration ($k = 1$ for horizontal, $k = 2$ for inclined, and $k = 3$ for inclined with shroud

attached), U is the inlet mean velocity and U_{cell} is the measured cell velocity. A positive value indicates the cell velocity is higher than the inlet velocity, while a negative value indicates the cell velocity is lower than the inlet velocity.

The standard deviation of the percent difference (Δ_{ij}) for a given installation condition, σ_k reflects the variation of the distribution for a given inlet condition. The standard deviation is calculated using,

$$\sigma_k = \sqrt{\frac{1}{N-1}\sum \Delta_{ijk}^2} \tag{6.2}$$

where N refers to the number of cells ($N = 23$). A large standard deviation indicates large amounts of variation while a low standard deviation indicates less variation (more homogeneous flow distribution).

6.2.1 Horizontal Position

The radiator is tested in the horizontal configuration with inlet velocities ranging from 0.26 to 9.57 m/s.

The results for the radiator exit plane survey for inlet mean velocities (0.26, 5.04, and 9.57 m/s) are shown in Figures 6.4 - 6.6. The results for the full range of velocity conditions is shown in Appendix C.1.1. Note that in the velocity figures, blue refers to a low velocity and yellow refers to a high velocity, while in the percent difference figures, pink refers to a negative percent difference and yellow refers to a positive percent difference.

The cases represent the radiator at three respective inlet conditions. At low speeds (0.26 m/s), the left portion of the radiator has minimal flow, with a flow decrease of 10% up to 60%. At higher speeds ($\geq$5 m/s) the velocity distribution in the radiator center is more homogeneous, since most percent differences are 7% or less of the inlet velocity. At these speeds, there are still areas of high and low velocity around the perimeter of the radiator. Eventually (at 9.57 m/s), the areas around the perimeter of the radiator start to homogenize as well.

This is also reflected in the standard deviation. The standard deviation for the range of inlet velocities is shown in Figure 6.7 (the exact standard deviation values are shown in Table C.1 in Appendix C.1.2). At extremely low velocities ($\leq$ 1 m/s), there is a large amount of variation in the flow distribution. As the inlet velocity increases from 2.02 m/s to 9.57 m/s, the flow distribution slowly becomes more homogeneous. From Figures 6.4 - 6.6, this occurs first in the radiator center, then outwards.

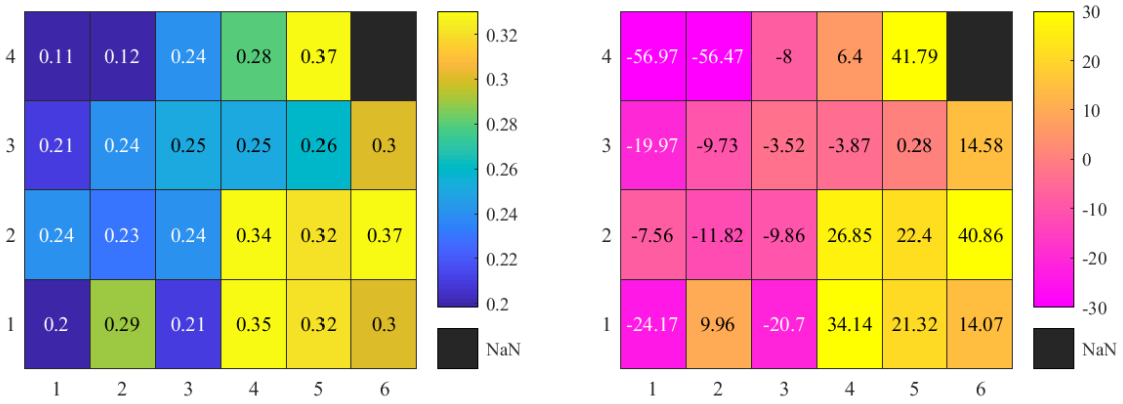

(a) Velocity (b) Percent difference

Figure 6.4: Radiator exit plane flow distribution in the horizontal configuration with inlet velocity of 0.26 m/s

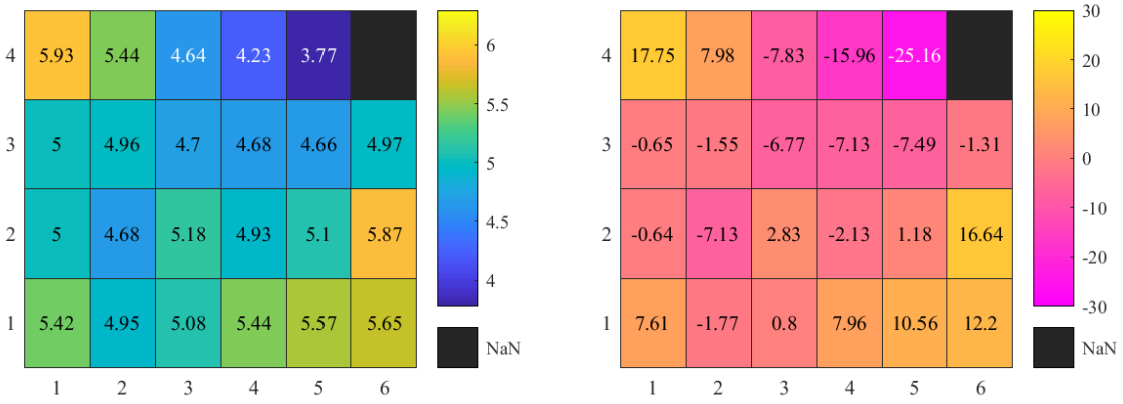

(a) Velocity (b) Percent difference

Figure 6.5: Radiator exit plane flow distribution in the horizontal configuration with inlet velocity of 5.04 m/s

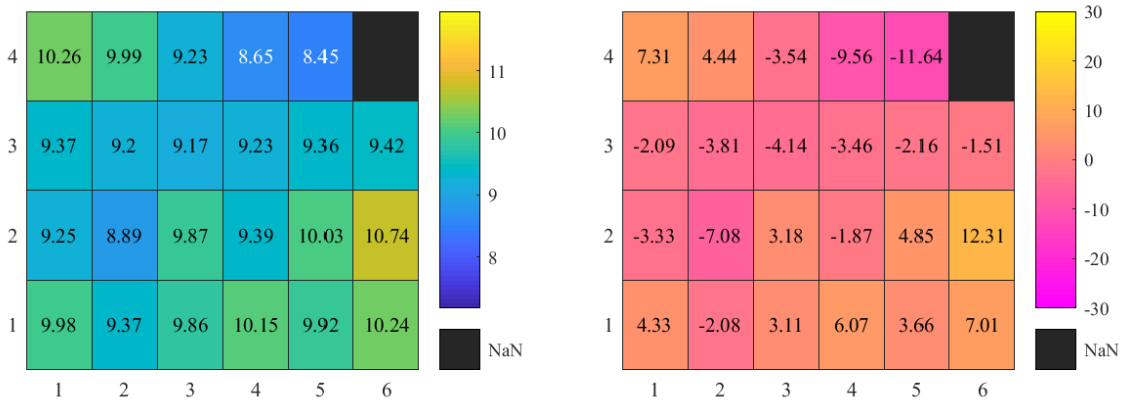

(a) Velocity (b) Percent difference

Figure 6.6: Radiator exit plane flow distribution in the horizontal configuration with inlet velocity of 9.57 m/s

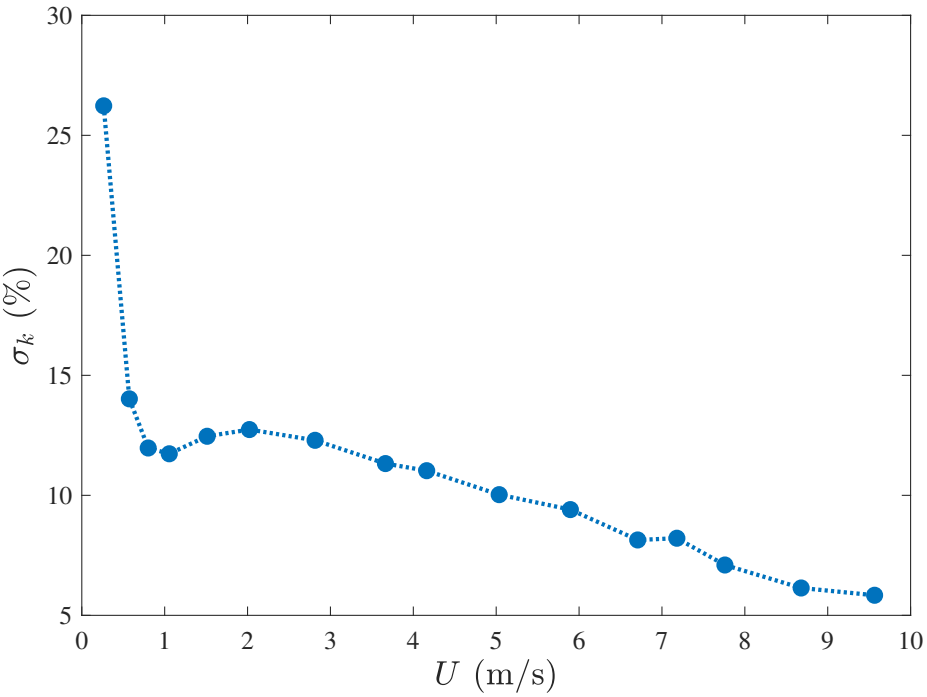

Figure 6.7: Standard deviation of velocity distribution in horizontal configuration

In the horizontal configuration, the gradients are between $0 \leq \xi \leq 0.2$. Therefore the correction scheme is not necessary.

6.2.2 Inclined Position

The inlet entry channel is placed on the radiator to evaluate the inclined configuration. Sixteen velocity conditions ranging from 0.26 to 9.28 m/s are evaluated.

The results for the radiator exit plane survey for inlet velocities (0.26, 4.93, and 9.28 m/s) are shown in Figures 6.8 - 6.10. The data for the full range of inlet conditions is shown in Appendix C.2.1. The velocity distribution is similar to the horizontal configuration, implying that the effect of the 8° inclination on the flow distribution is subtle. The standard deviation for the range of inlet conditions is shown in Figure 6.11 (the exact standard deviation values are shown in Table C.2 in Appendix C.2.2). The same effect observed in the horizontal configuration (Figure 6.7) is present in the inclined configuration.

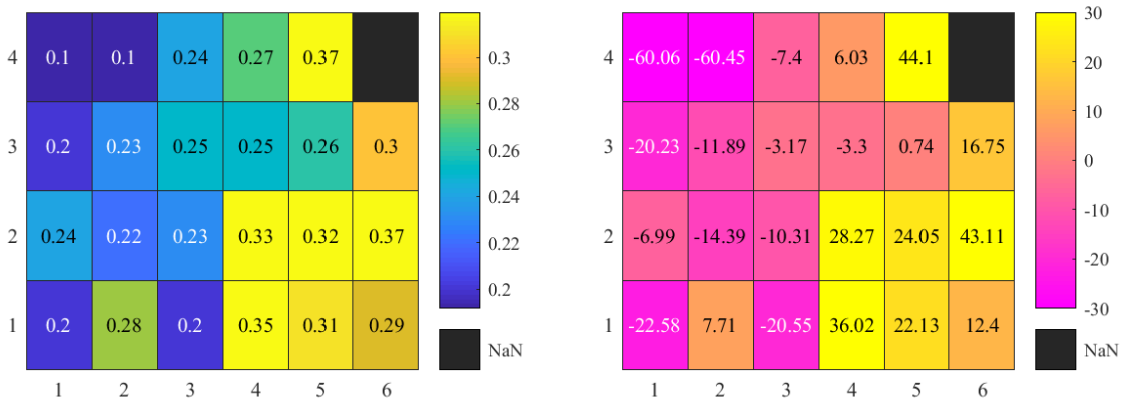

(a) Velocity

(b) Percent difference

Figure 6.8: Radiator exit plane flow distribution in the inclined configuration with inlet velocity of 0.26 m/s

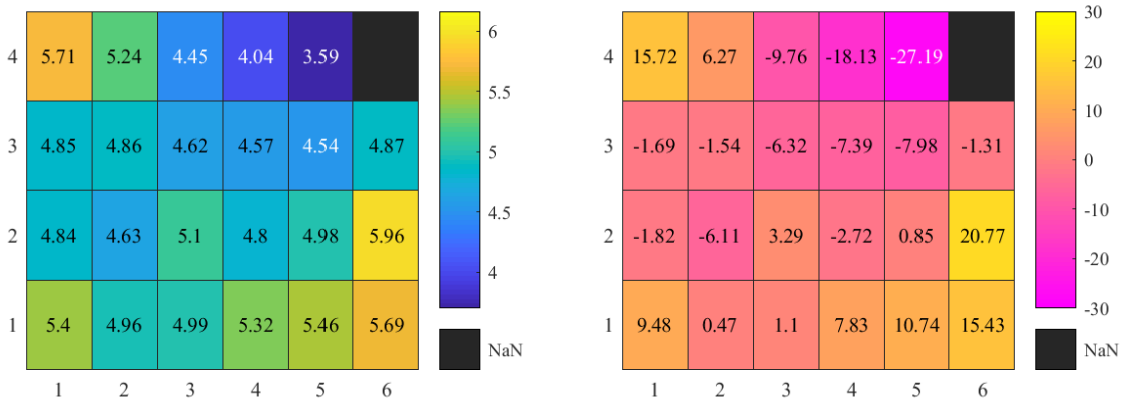

(a) Velocity (b) Percent difference

Figure 6.9: Radiator exit plane flow distribution in the inclined configuration with inlet velocity of 4.93 m/s

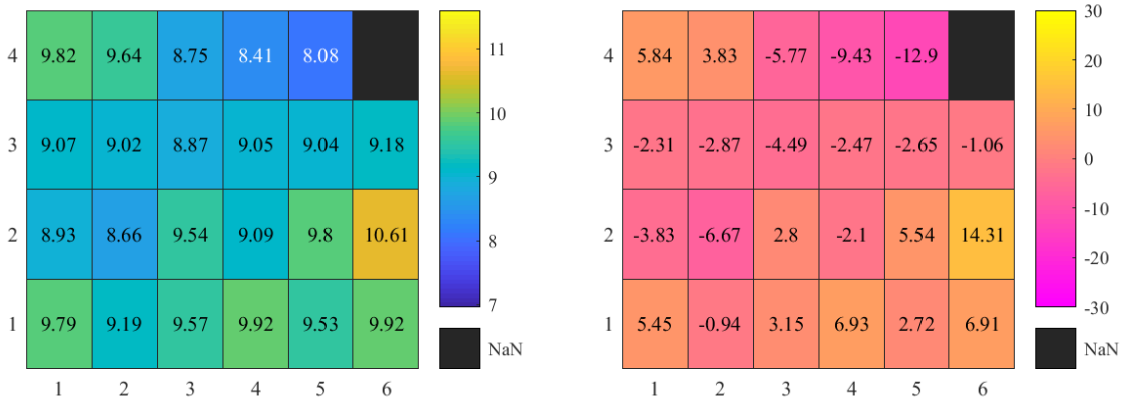

(a) Velocity (b) Percent difference

Figure 6.10: Radiator exit plane flow distribution in the inclined configuration with inlet velocity of 9.28 m/s

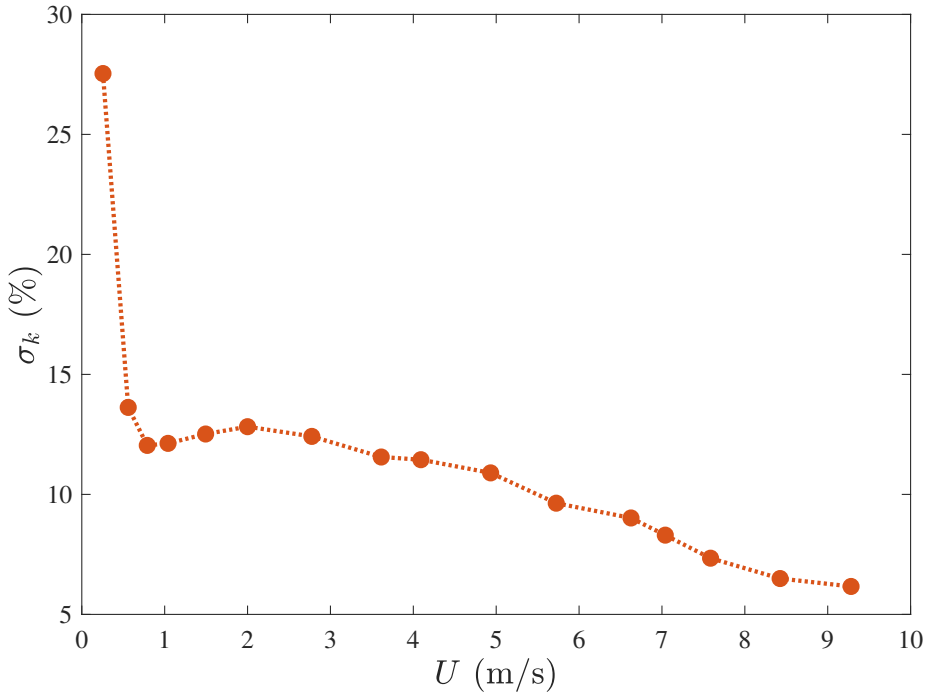

Figure 6.11: Standard deviation of velocity distribution in inclined configuration

To validate the proposition that the inclined configuration has a minimal effect on the flow distribution through the radiator, the horizontal cell velocity is plotted against the inlet velocity as a linear model with 95% confidence intervals. Then the data points from the inclined configuration are added to the plot. The results for cell 1 are shown in Figure 6.12. The results for the rest of the cells are shown in Appendix C.2.3. All the inclined data points are within or near the 95% confidence band over the range of inlet mean velocities tested, implying that there is a minimal effect from inclining the radiator at 8°. This is consistent for all 23 cells as reflected in Table 6.1.

Table 6.1 shows the percentage of inclined data points that lie within the established 95% confidence intervals. For the majority of cells 90-100% of the data points lie within these intervals, with the exception of cell 13 at 81.25%. This indicates that the effect of inclining the radiator at an 8° angle has a minimal influence on the radiator flow distribution.

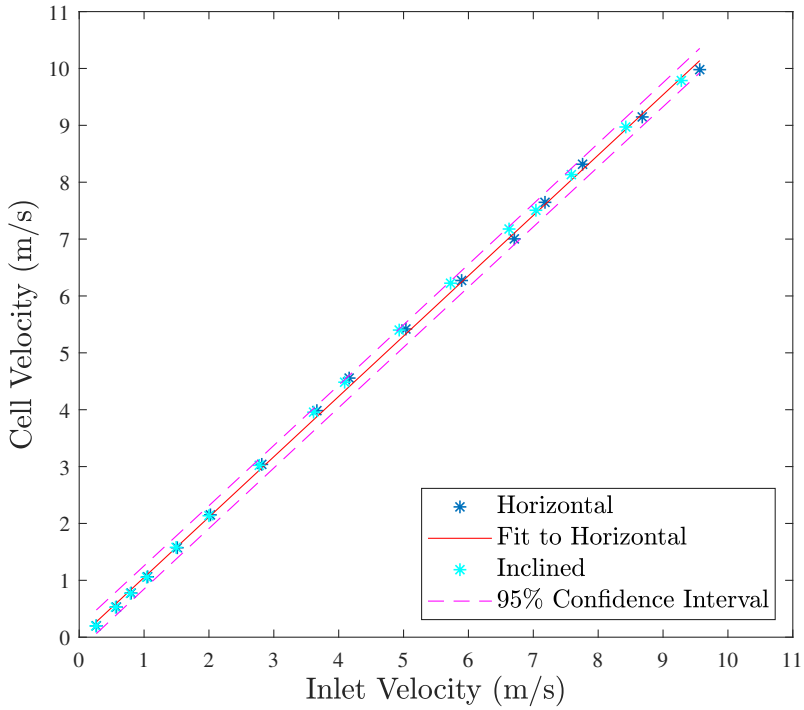

Figure 6.12: Cell velocity vs. inlet velocity with 95% confidence intervals for cell 1

Cell Number	Percent of data points within confidence interval
1	100 %
2	100 %
3	93.75 %
4	93.75 %
5	100 %
6	93.75 %
7	93.75 %
8	100 %
9	93.75 %
10	100 %
11	100 %
12	93.75 %
13	81.25 %
14	93.75 %
15	100 %
16	100 %
17	93.75 %
18	100 %
19	100 %
20	100 %
21	100 %
22	100 %
23	93.75 %

Table 6.1: Percentage of inclined data points within the 95% confidence intervals

Another means for exploring the difference in flow distribution is by examining the change in percent difference, Δ, between the horizontal and inclined configurations. This is given as,

$$\Delta_{ij2} - \Delta_{ij1} \tag{6.3}$$

where subscripts for for k are 1 and 2 denoting the inclined and horizontal percent differences, respectively.

Since the radiator inclination is with respect to its length (variation in the flow angle with respect to the 'row'), its velocity distribution is expected to vary for each row. Thus, the change in percent difference is evaluated as the average for each row. The change percent

difference for five selected velocities over the range of inlet velocities tested is shown in Figure 6.13a. Regardless of the inlet velocity, the general observation is an increase in velocity for rows 1-2 and a decrease in velocity for rows 3-4. To represent the effect of inclining the radiator over all the inlet velocities, the average change in percent difference (for all inlet conditions) is evaluated. This is shown in Figure 6.13b. The average change in percent difference is marginal, ranging from -0.98% to 0.52%. For an inlet velocity of 10 m/s, a -1.0% change in percent difference would correspond to a 0.1 m/s loss in velocity due to the incline. The top of the radiator, row 4, is most affected with a 0.98% loss in velocity. This is balanced out by an increase in velocity from 0-0.5% for rows 1-3.

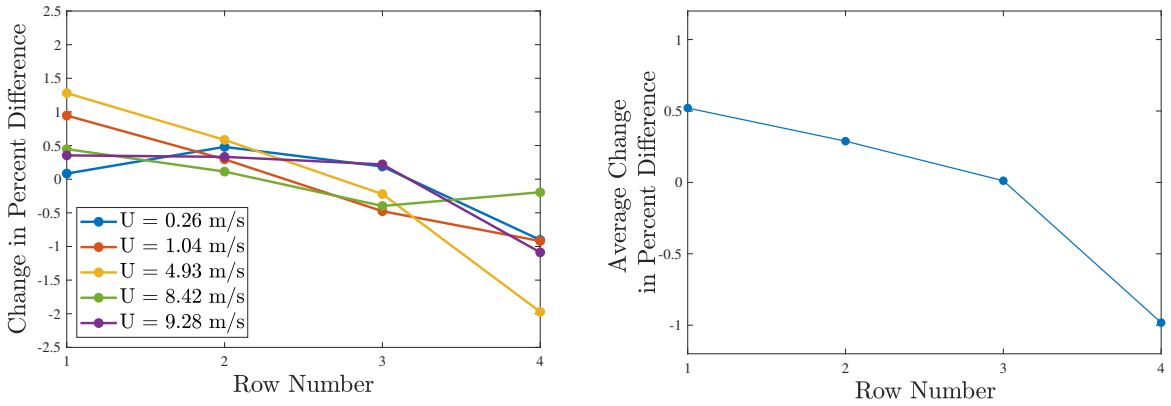

(a) Change for selected velocities

(b) Average change for all velocities

Figure 6.13: Change in percent difference by row

Similar to that for the horizontal position, the correction scheme is not necessary due to the low gradients ($0 \leq \xi \leq 0.2$).

6.2.3 Inclined Configuration with Shroud Attached

With the shroud attached, flow exiting the radiator is directed toward the shroud opening (see Figure 6.3). A schematic depiction of the TTA frame position with respect to the shroud opening is shown in Figure 6.14.

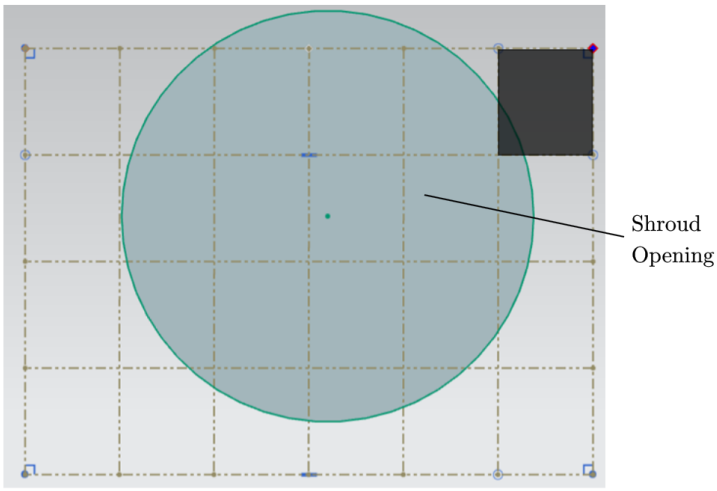

Figure 6.14: Schematic representation of TTA frame position with respect to the shroud opening

With the shroud attached, the blockage around the perimeter causes a larger variation in flow distribution among the neighboring cells. Velocity gradients range from $0 \leq \xi \leq 0.4$. The gradient correction scheme from Chapter 5.4 is implemented. In instances where the dimensionless gradient is $0.3 \leq \xi \leq 0.4$ the correction curve is implemented. The inlet velocities where this gradient range is observed is between 6.40 to 8.85 m/s (see Appendix C.3.1 for all corrected velocity distributions). The velocity distributions before and after the correction for an inlet velocity of 8.85 m/s is shown in Figure 6.15. The cells eligible for correction are the cells blocked by the shroud in the left portion (first column) and lower right portion of the radiator (last column). Note that there is not a large velocity change between corrected and uncorrected velocities, even with velocity gradients between 0.3-0.4.

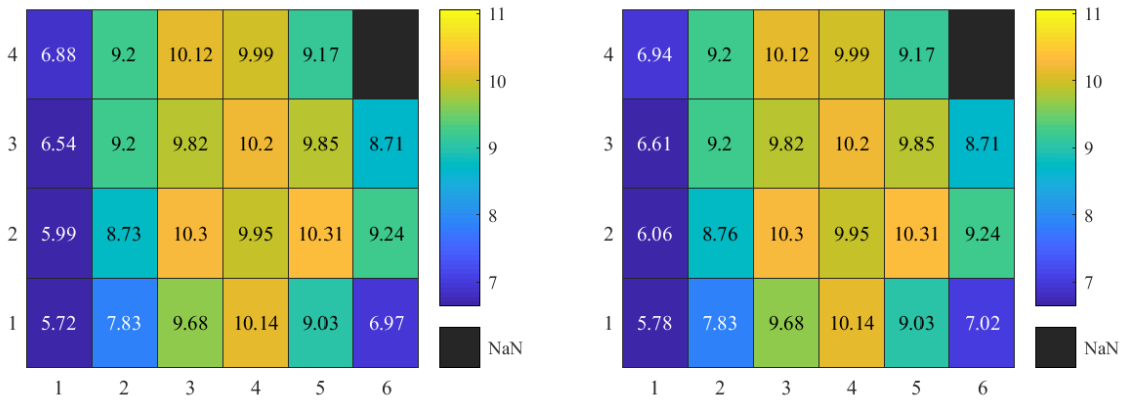

(a) Before correction

(b) After correction

Figure 6.15: Radiator exit plane flow distribution with shroud attached before and after correction for inlet velocity of 8.85 m/s

Following the correction of selected cells, the velocity distribution and percent differences are evaluated.

The radiator configuration including the shroud is tested at velocities ranging from 0.26 to 8.85 m/s. The results for the radiator exit plane survey for inlet velocities of 1.03 and 8.29 m/s are shown in Figures 6.16 and 6.17. The data for the full range of inlet conditions are shown in Appendix C.3.2. For both inlet velocities shown, the region with the greatest mass flow (largest local velocity) is in the center, near the shroud opening. Likewise, the lowest velocities are observed in the left region of the radiator, where the shroud strongly blocks the TTA cells. In the left column of TTA cells, the velocity is nominally 21% lower for the inlet condition of 1.03 m/s. This velocity deficit increases as the inlet condition increases to 8.29 m/s, where the measured cell velocity is nominally 28% lower than the mean inlet velocity.

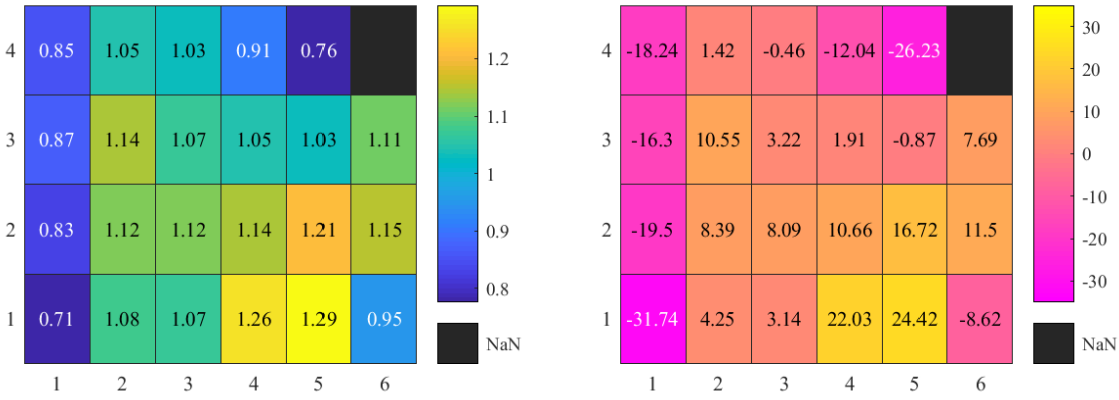

(a) Velocity (b) Percent difference

Figure 6.16: Radiator exit plane flow distribution with shroud attached and inlet velocity of 1.03 m/s

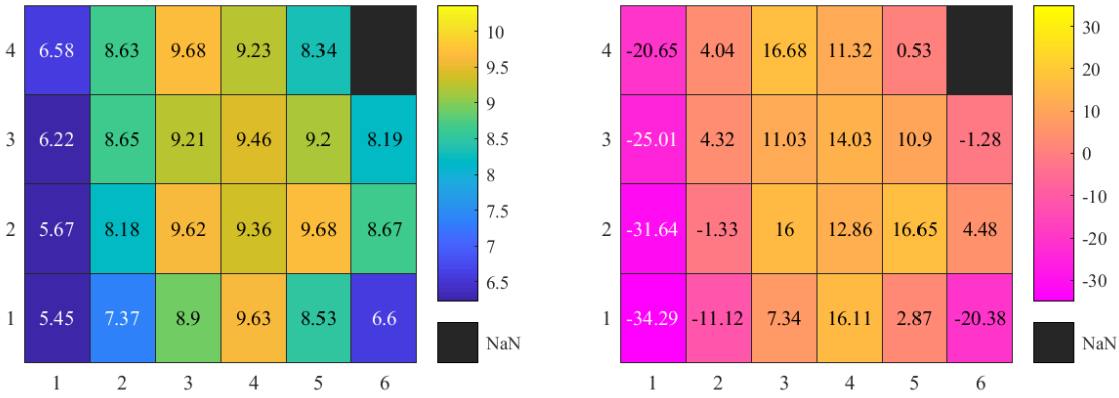

(a) Velocity (b) Percent difference

Figure 6.17: Radiator exit plane flow distribution with shroud attached and inlet velocity of 8.29 m/s

To evaluate the effect of the shroud on the flow distribution, the radiator and shroud are taken to be a control volume with the exiting flow as a curved streamline. The flow kinetic energy along the streamline ($\rho U^2/2$) is integrated over the radiator exit control surface,

$$\int_{CS} \rho \frac{U^2}{2} \left(\vec{U} \cdot \vec{n} \right) dA. \tag{6.4}$$

The kinetic energy flux for a given cell velocity represents the pressure drop from the atmosphere to the below the radiator over the given area. The significance of the kinetic

energy flux is that it is related to the fan power requirement to deliver a specified mass flux across the radiator. The term U^3 in the kinetic energy flux is summed over all the cells and is denoted by κ,

$$\kappa = \sum_{i=1}^{23} U_i^3 \tag{6.5}$$

where κ is proportional to the kinetic energy flux. The evaluation of κ is done for the radiator with and without the shroud (inclined configuration). The results are plotted as a function of inlet mean velocity to illustrate the 'cost' of adding the shroud. These results are in Figure 6.18. κ with the shroud is larger than without, particularly observable for inlet velocities ≥ 5 m/s. This indicates that a larger fan power is required to provide a given mass flow rate.

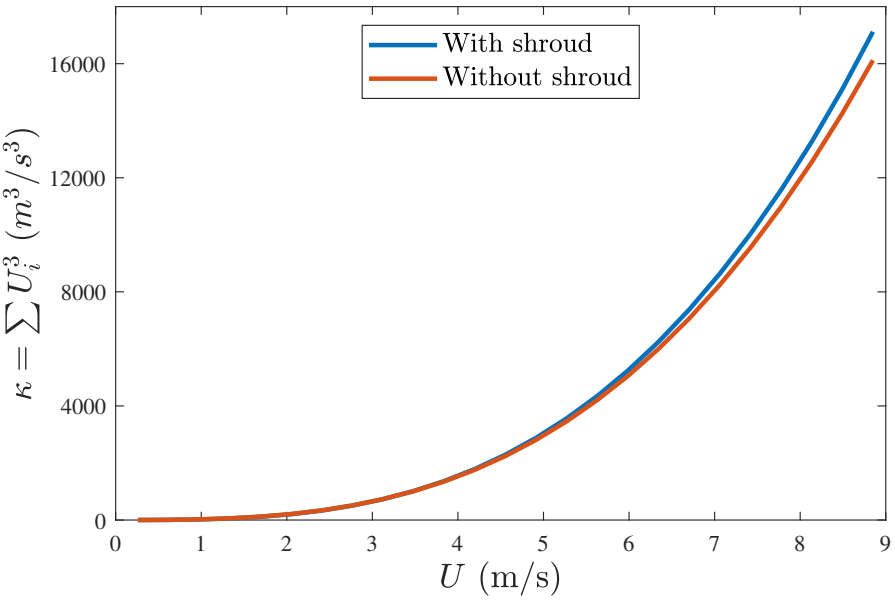

Figure 6.18: Kinetic energy flux with and without the shroud attached

The difference in κ with and without the shroud illustrates the cost of adding the shroud. This is shown in Figure 6.19. For low inlet velocities (≤ 4 m/s), the difference is negligible. For inlet velocities > 4 m/s the difference becomes significant, indicating the impact of the shroud is experienced at higher velocities.

It is notable that when the vehicle is in motion, which corresponds to higher inlet velocities, the radiator fan is shut off. While the nonuniform flow distribution induced by the shroud may have an impact on the radiator heat transfer performance, the presence of the shroud has minimal impact on the radiator fan power consumption.

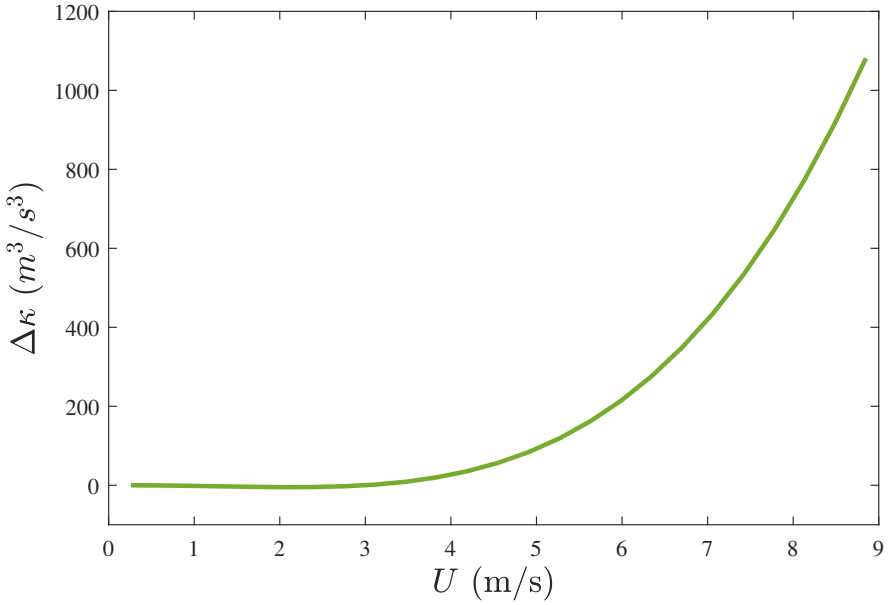

Figure 6.19: Difference between kinetic energy flux with and without the shroud

CHAPTER 7

SUMMARY AND CONCLUSIONS

The novel airflow measurement device, the thermal transient anemometer (TTA), has been described and presented herein.

Each of the cells in the TTA were calibrated in the AFRD wind tunnel facility. The cells were calibrated with uniform velocities ranging from 0.1 to 13 m/s as determined using a calibrated hot-wire probe along with the TTA frame. The average uncertainty from the calibration was ± 0.19 m/s.

Numerical simulations were utilized to observe the transient convective effects of the sensing wire in one TTA cell. The numerical simulations were adjusted to represent selected calibrated TTA cells by adjusting the constants in the Nusselt number (see Chapter 4.2.1). Inlet mean velocities ranging from 0.1 to 15 m/s with uniform dimensionless gradients, dU^*/dx^* and dU^*/dy^*, (see Sections 5.2 - 5.3) ranging from 0 to 1.9 were simulated. The gradients were imposed along both the length and height of a TTA cell to provide a horizontal and vertical gradient. For a given mean velocity, the wire cooled more slowly with the existence of a velocity gradient, particularly over 0.5. This was due to the nonuniform, nonlinear temperature distribution along the wire caused by the velocity gradient, thus affecting the wire resistivity and resistance decay. This resulted in a difference of 1% with a gradient of 0.4 to 13% and 24% with horizontal and vertical gradients of 1.9 respectively, when using the uniform calibration to calculate the mean velocity. The relative effect of the vertical velocity gradient is stronger than that of the horizontal gradient, due to the variation in the velocity along the sensing wire.

A correction scheme was developed to address the large error observed at high gradients. After implementing the correction scheme, the error in mean velocity was within 1% for most gradients. The correction scheme was validated by empirical data collected with the TTA (cells 13 - 15). Three different mean velocities (3.27, 6.21, and 8.93 m/s) with respective

horizontal gradients (dU^*/dx^* of 0.742, 0.632, and 0.707) were imposed on the selected TTA cells as determined in Chapter 5.5.

The TTA was utilized to measure the velocity distribution at the exit face of a radiator in various installation configurations: horizontal, inclined (8° angle), and inclined with a shroud attached. The following radiator configurations were tested with several inlet base conditions (between 16 - 18) ranging from 0.26 to 9.57 m/s, as provided by the AFRD facility. In the horizontal configuration, the velocity distribution at the exit of the radiator was extremely nonuniform at low velocities ($U \leq 1$ m/s) more than a 10% decrease in airflow in the left portion of the radiator. As the inlet base velocity was increased, the airflow distribution homogenizes first in the center of the radiator, then outwards. The effect of tilting the radiator at an 8° angle with respect to the plane of the grill is minimal, although the top row loses an average of 1% of flow as a result of the inclination (see Section 6.2.2). This is balanced by a small gain in flow (0% - 0.5%) for the other rows. The addition of the shroud blocks portions of the radiator, creating strong velocity gradients in the corners. The correction scheme was implemented to determine the correct velocity distribution. A term proportional to the kinetic energy flux was evaluated to observe the effect of adding the shroud. It was found that at low inlet velocities, the cost of adding the shroud is minimal, while at higher inlet velocities this cost is larger. This indicates that at higher inlet velocities (> 4 m/s) it requires more work for the flow to provide the same mass flux when the shroud is attached.

Future investigations with the TTA may include exploring the effects of different velocity profiles or testing with another TTA geometry configuration (different frame and/or cell dimensions with different wire).

APPENDICES

APPENDIX A

CALIBRATION OF TTA

A.1 Calibration Curves for all Cells

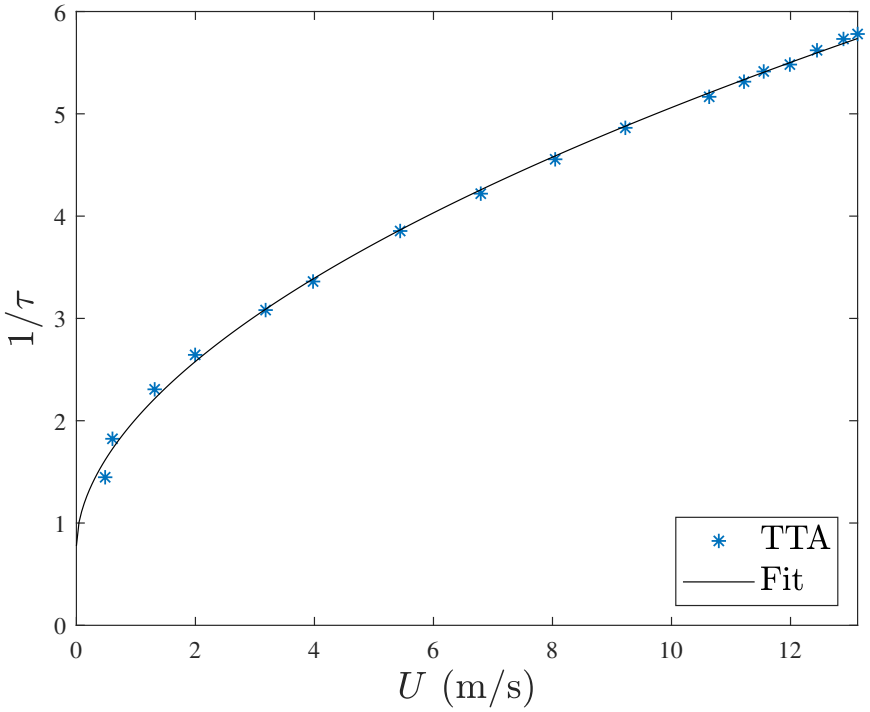

Figure A.1: TTA calibration curve for cell 1

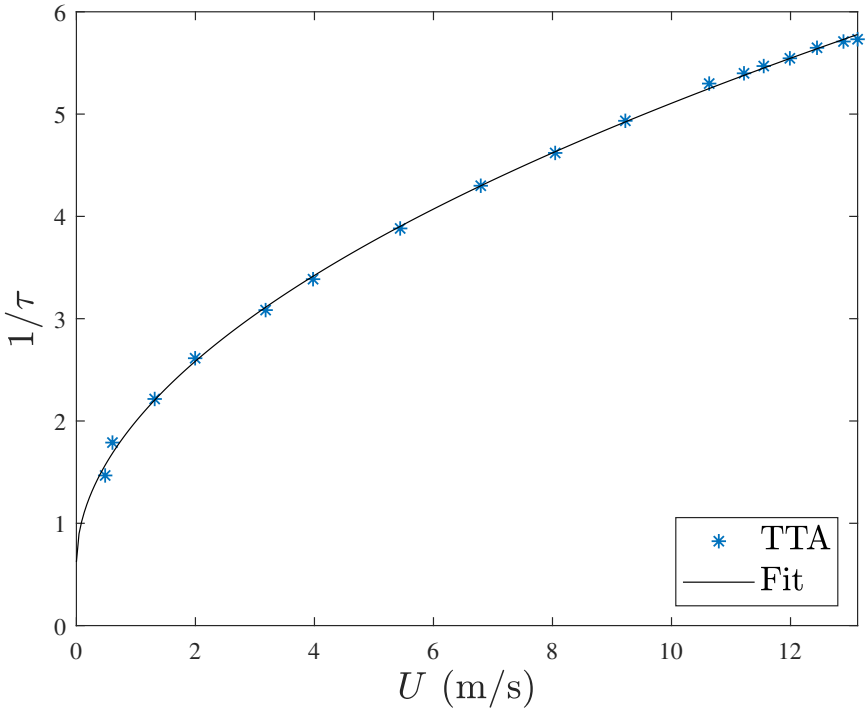

Figure A.2: TTA calibration curve for cell 2

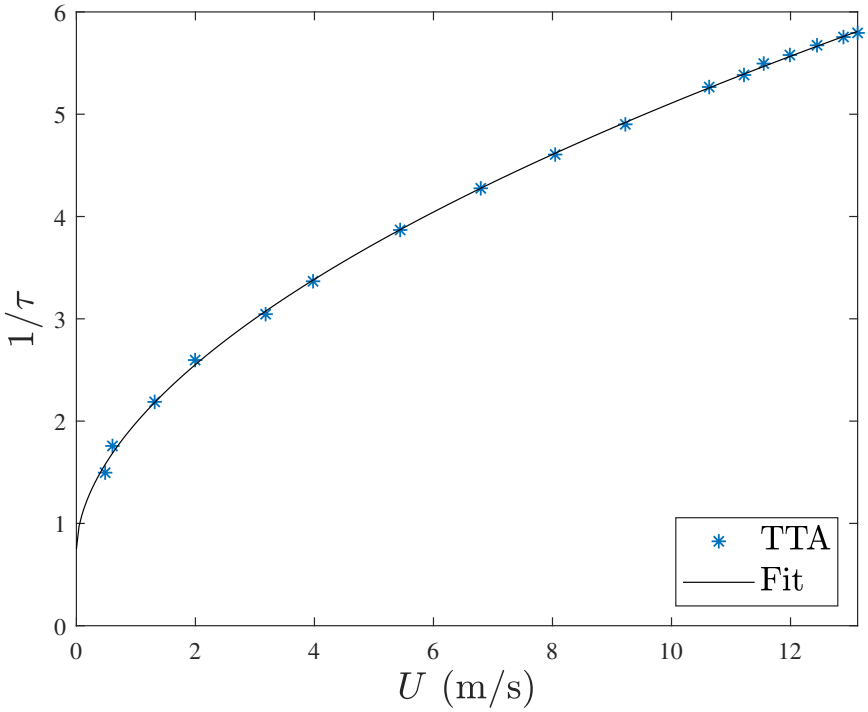

Figure A.3: TTA calibration curve for cell 3

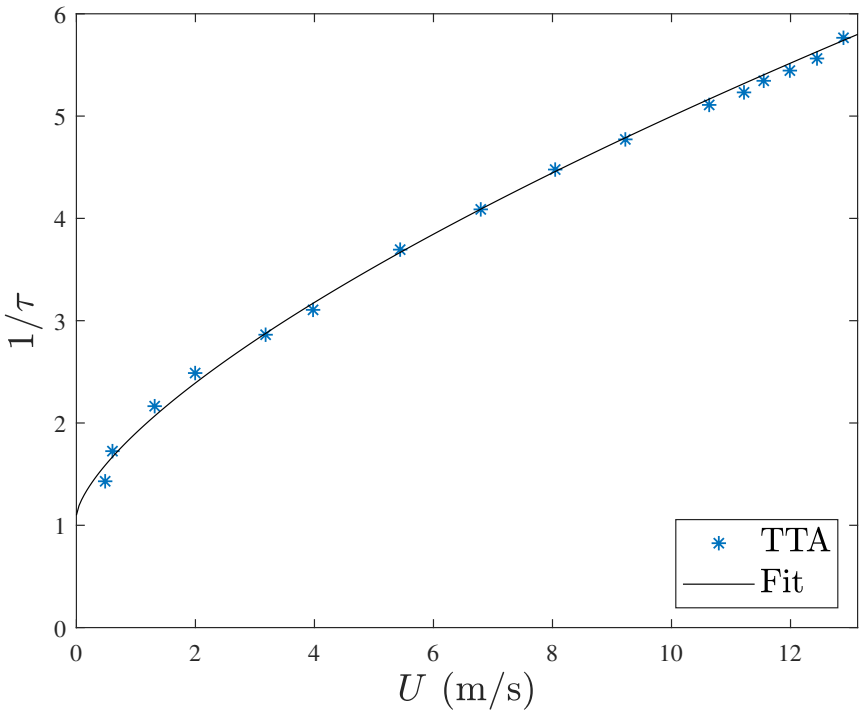

Figure A.4: TTA calibration curve for cell 4

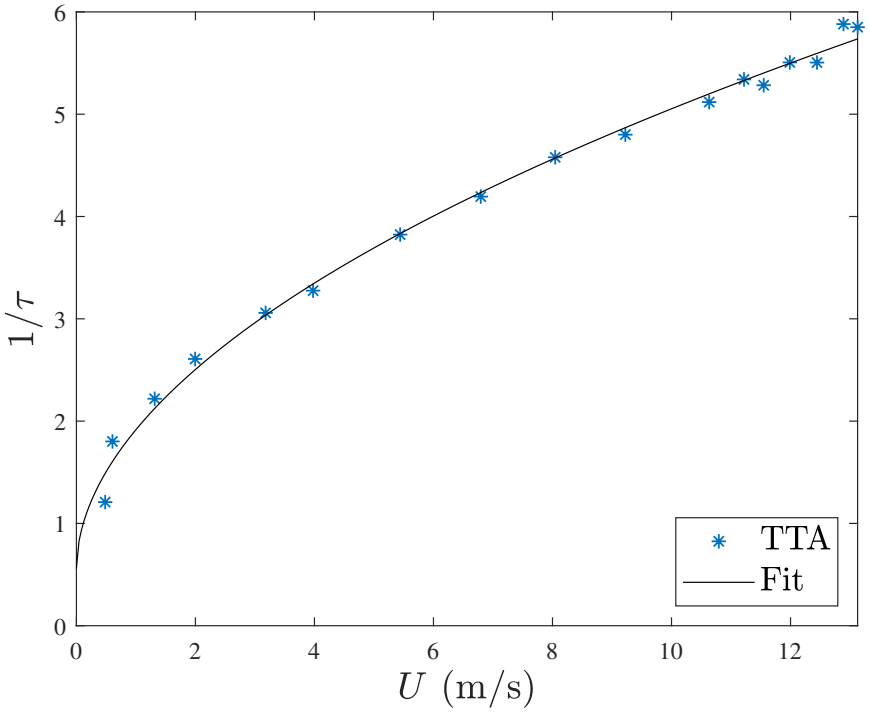

Figure A.5: TTA calibration curve for cell 5

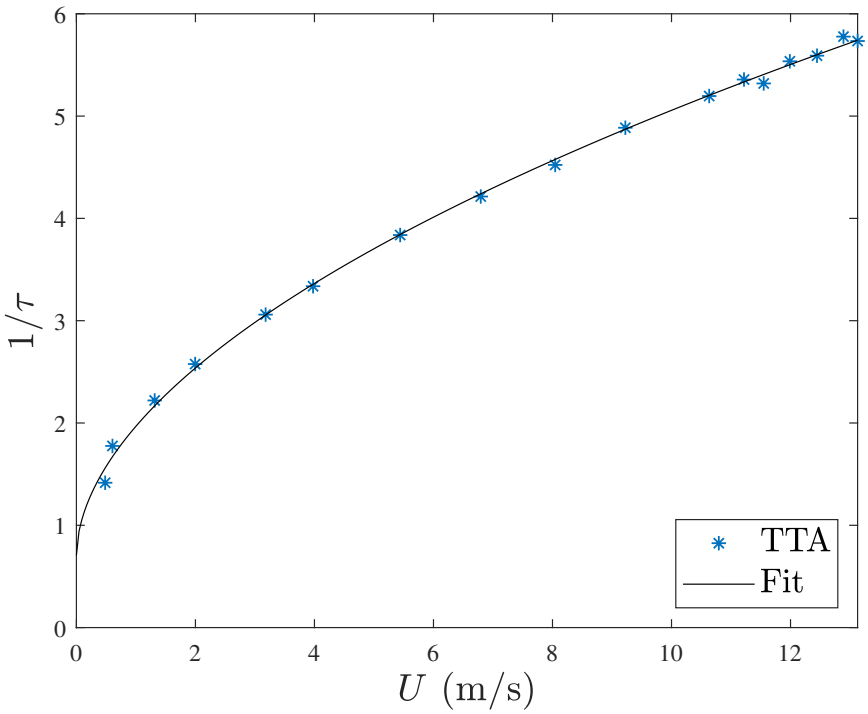

Figure A.6: TTA calibration curve for cell 6

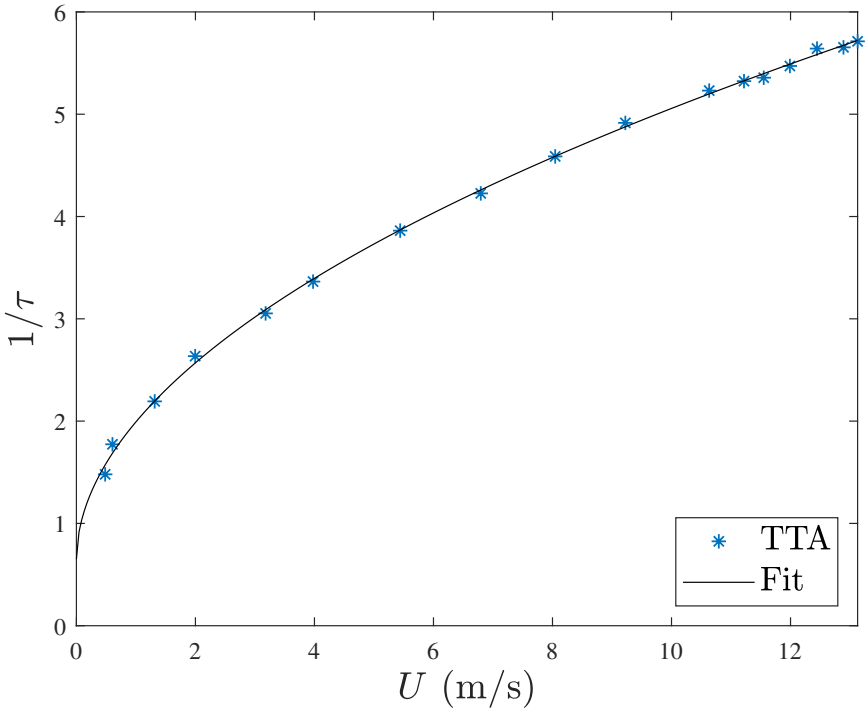

Figure A.7: TTA calibration curve for cell 7

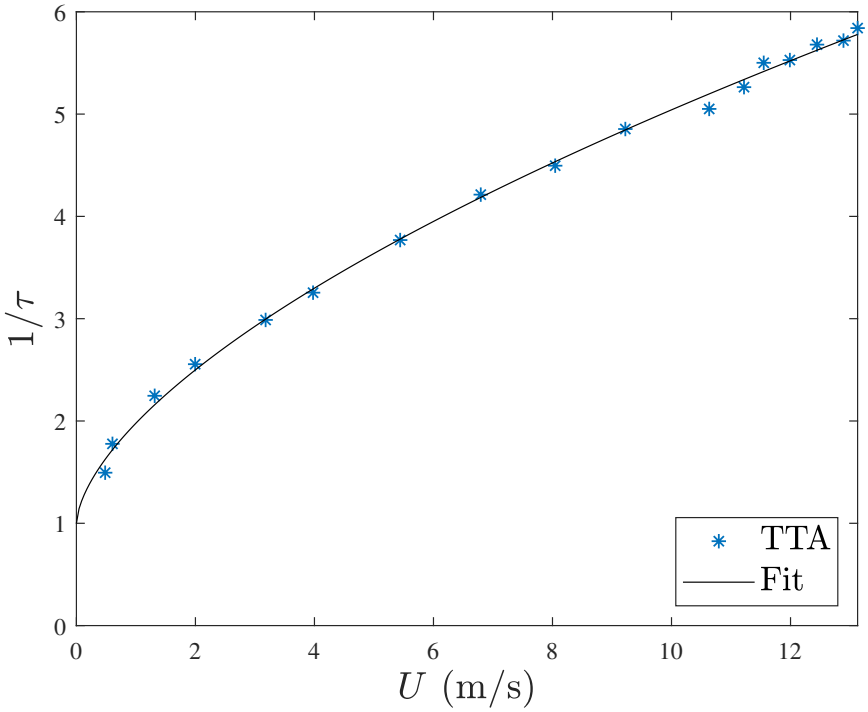

Figure A.8: TTA calibration curve for cell 8

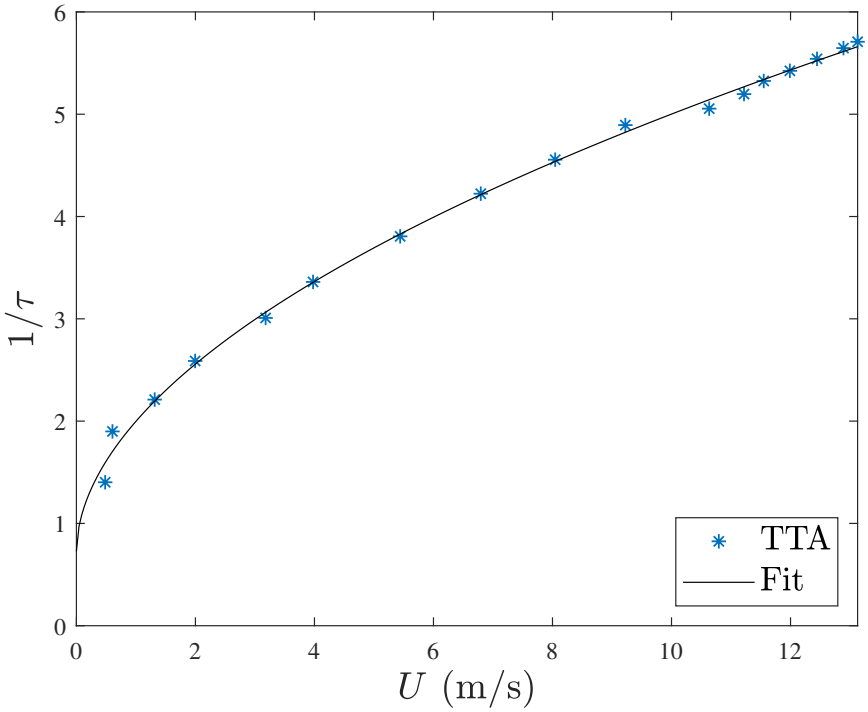

Figure A.9: TTA calibration curve for cell 9

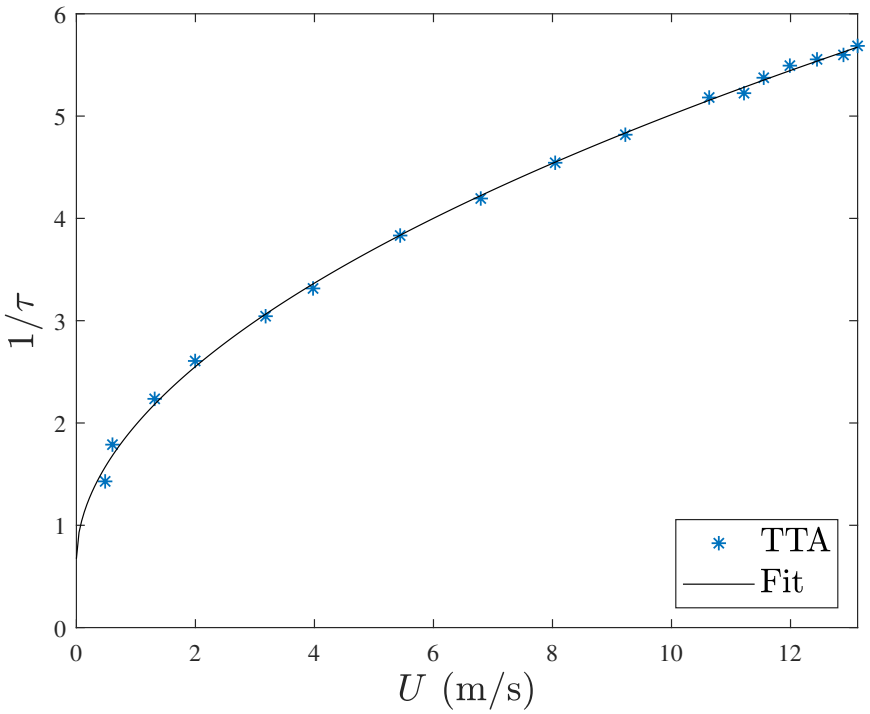

Figure A.10: TTA calibration curve for cell 10

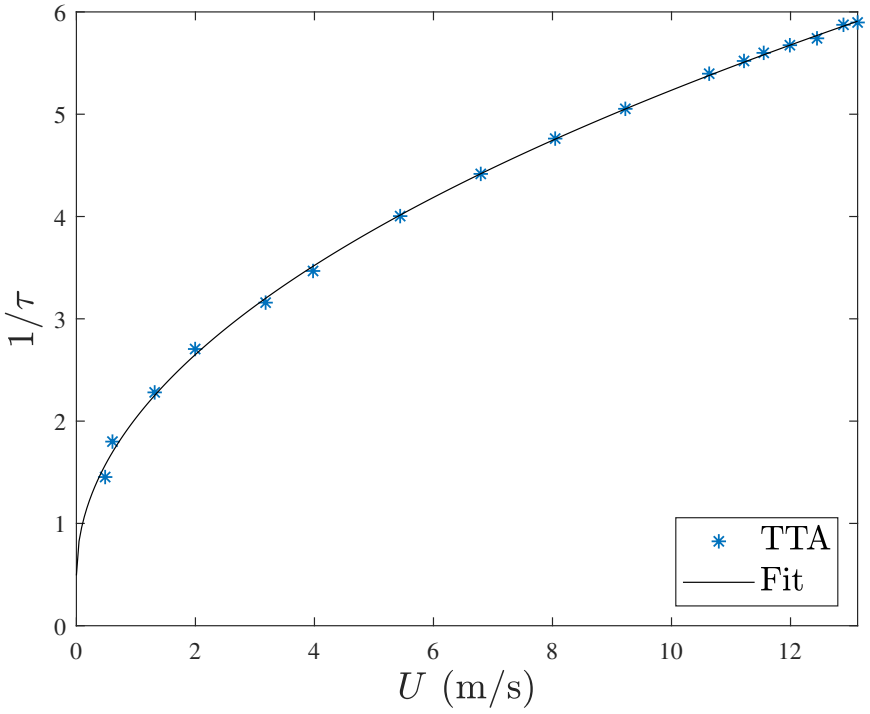

Figure A.11: TTA calibration curve for cell 11

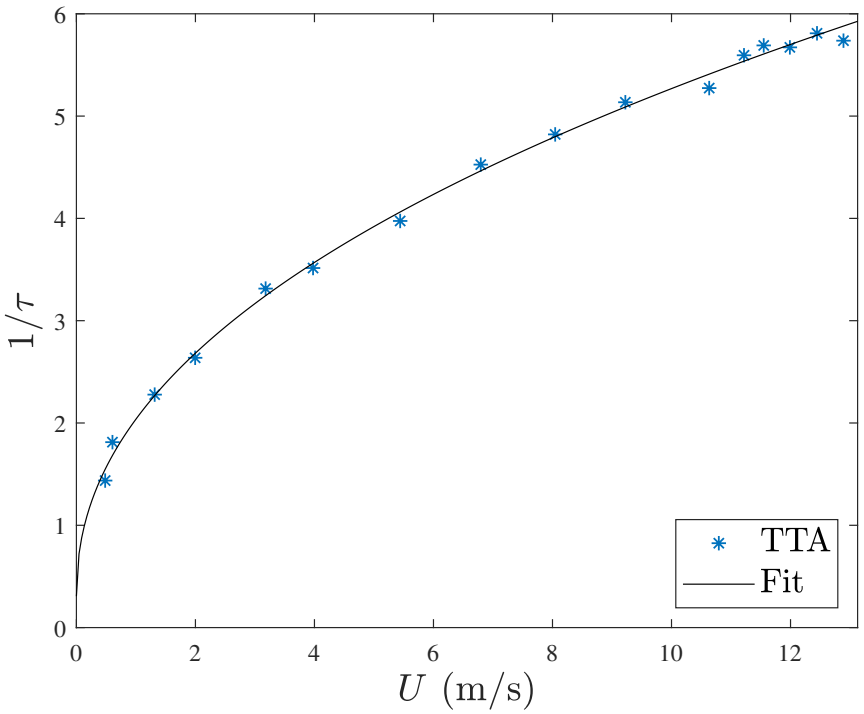

Figure A.12: TTA calibration curve for cell 12

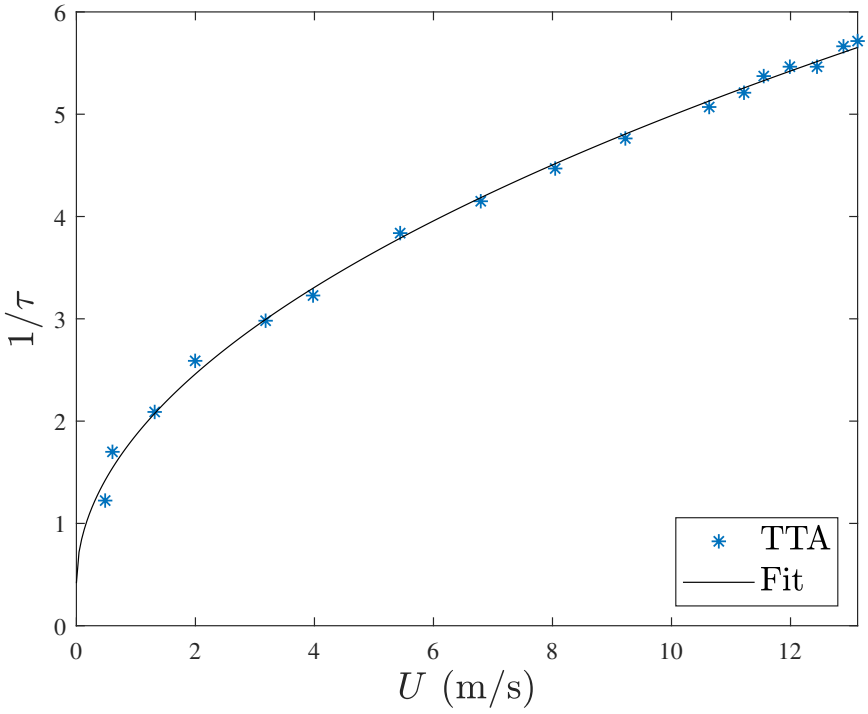

Figure A.13: TTA calibration curve for cell 13

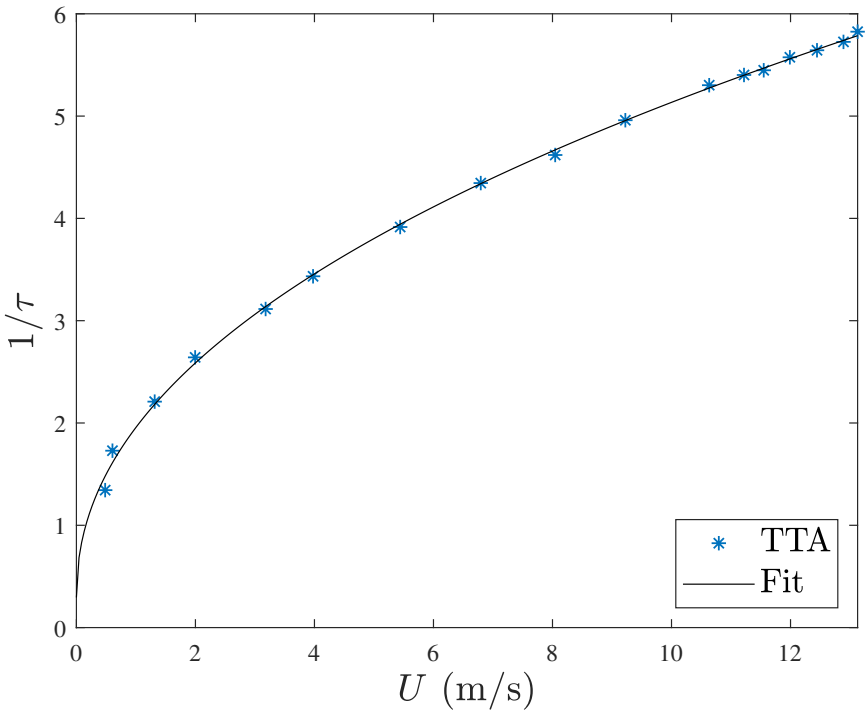

Figure A.14: TTA calibration curve for cell 14

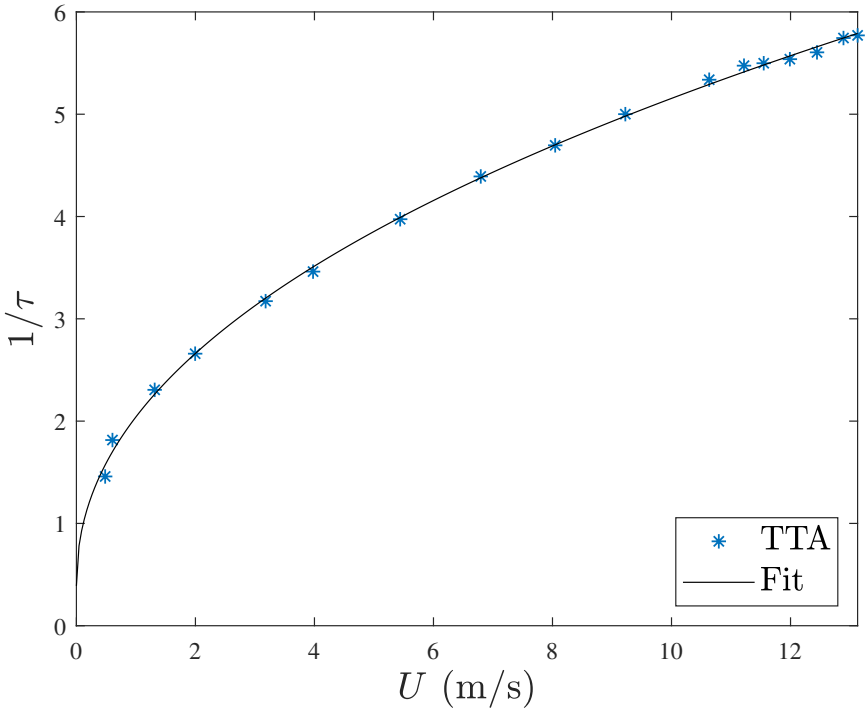

Figure A.15: TTA calibration curve for cell 15

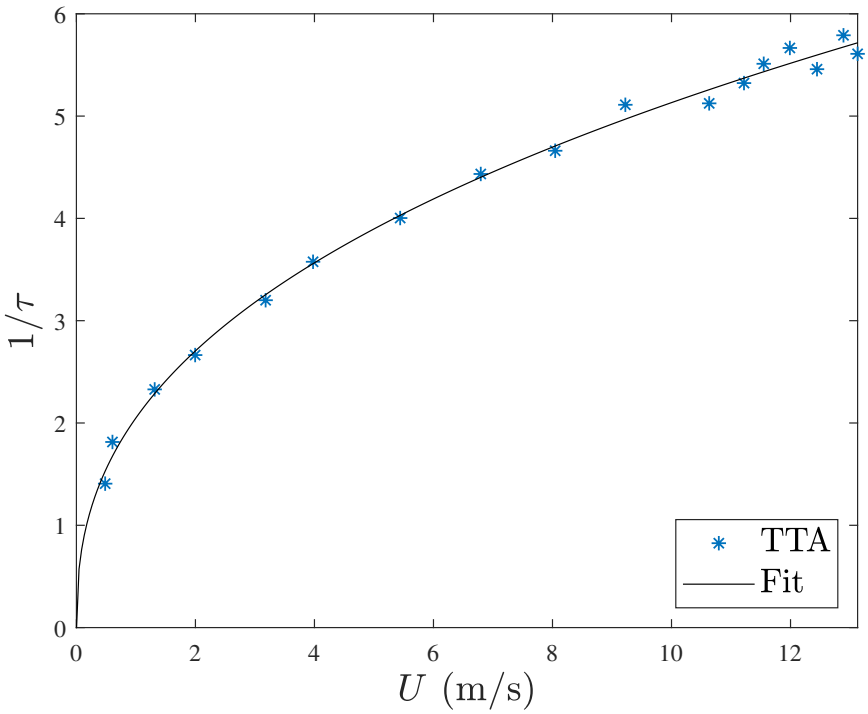

Figure A.16: TTA calibration curve for cell 16

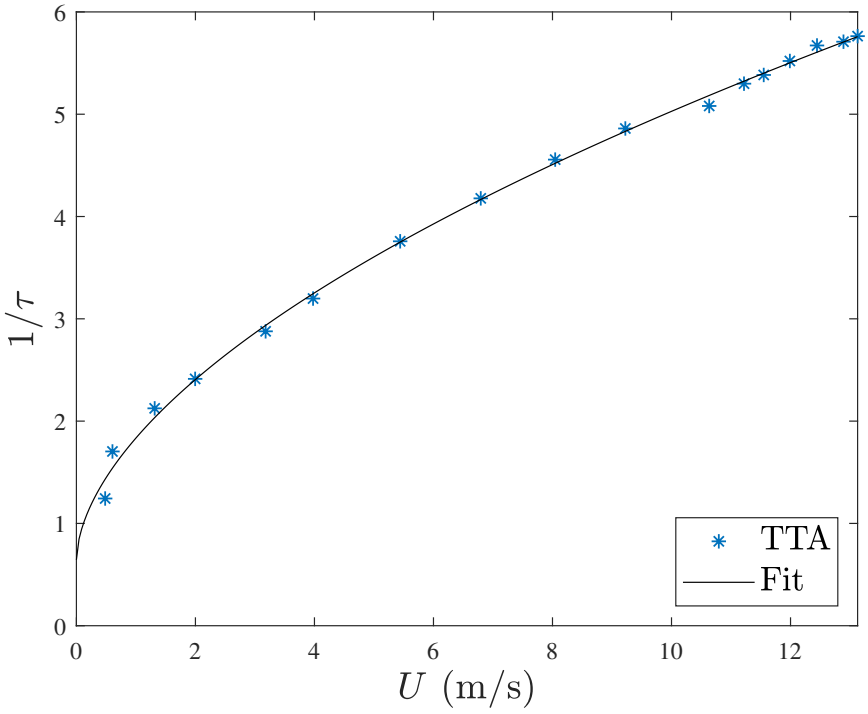

Figure A.17: TTA calibration curve for cell 17

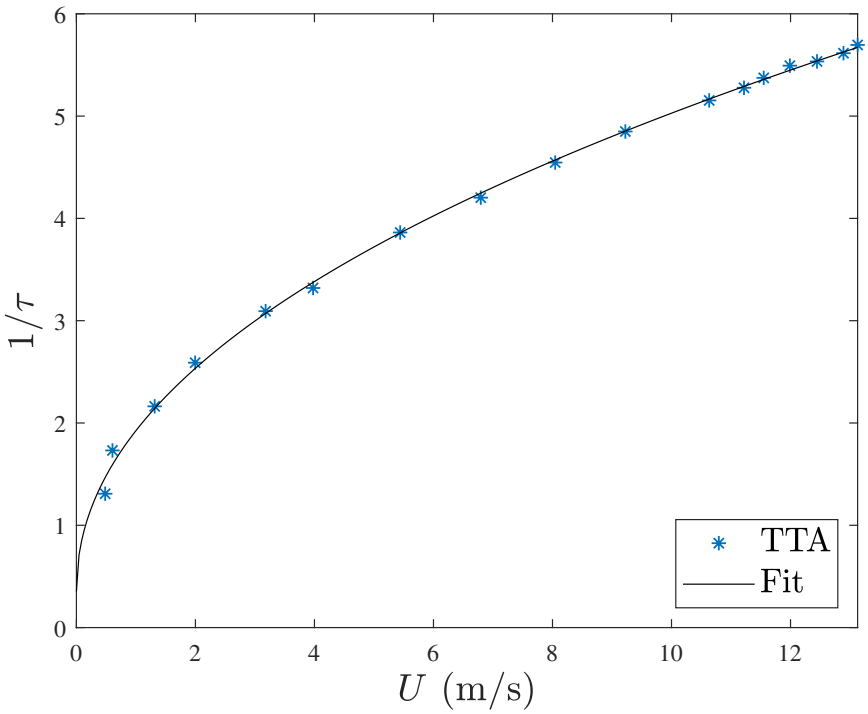

Figure A.18: TTA calibration curve for cell 18

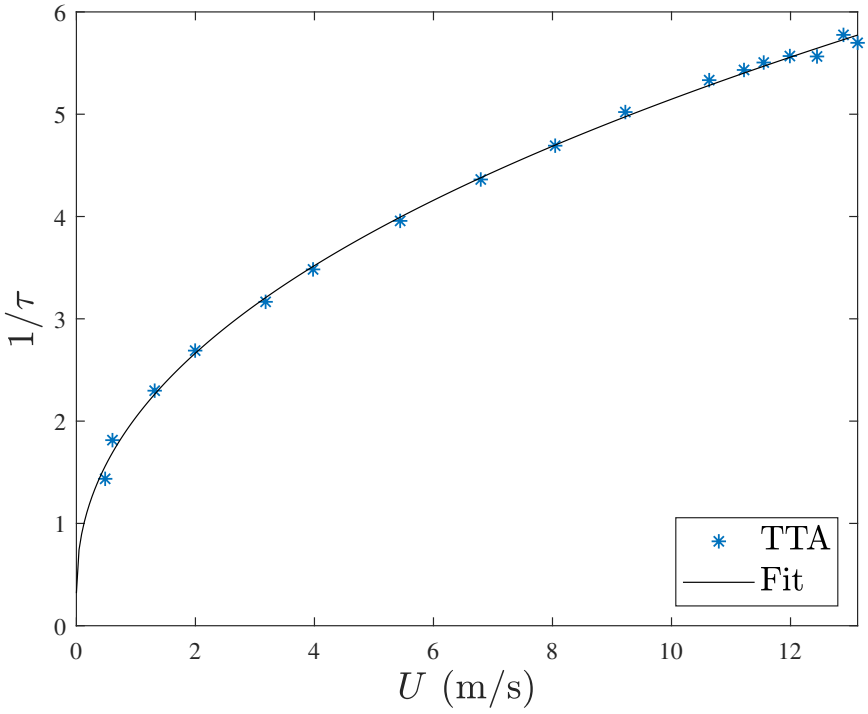

Figure A.19: TTA calibration curve for cell 19

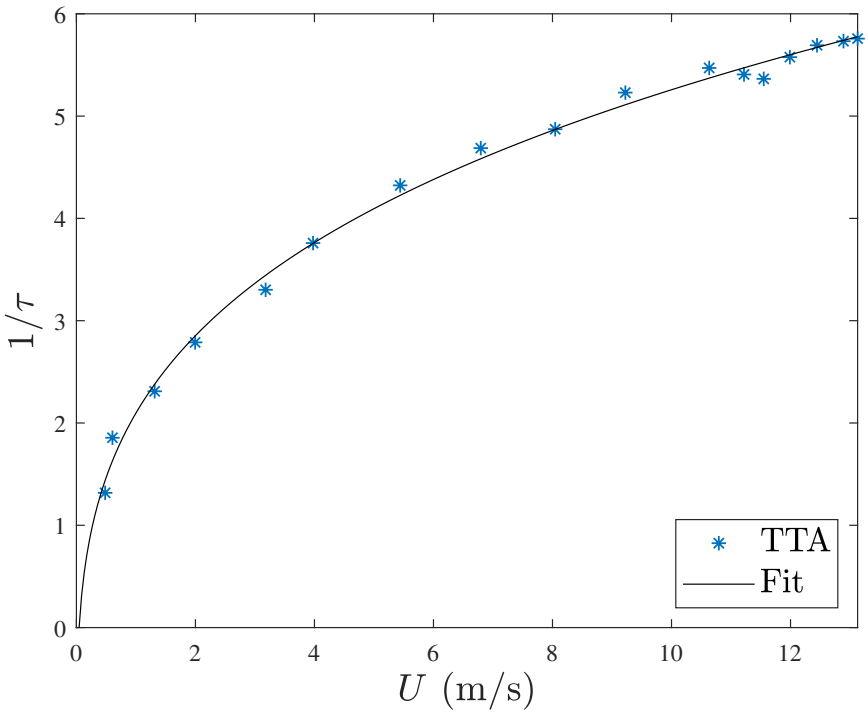

Figure A.20: TTA calibration curve for cell 20

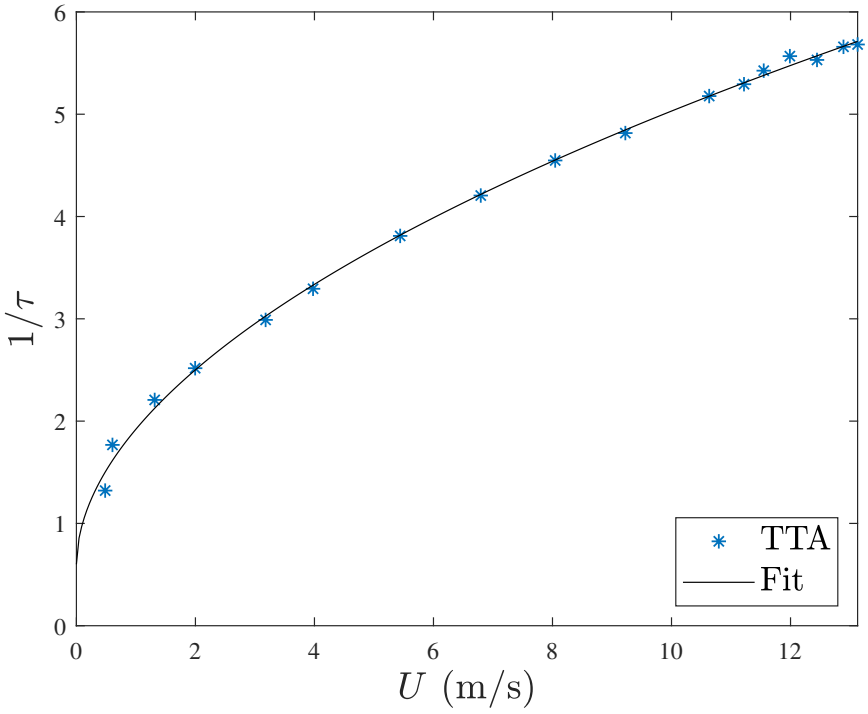

Figure A.21: TTA calibration curve for cell 21

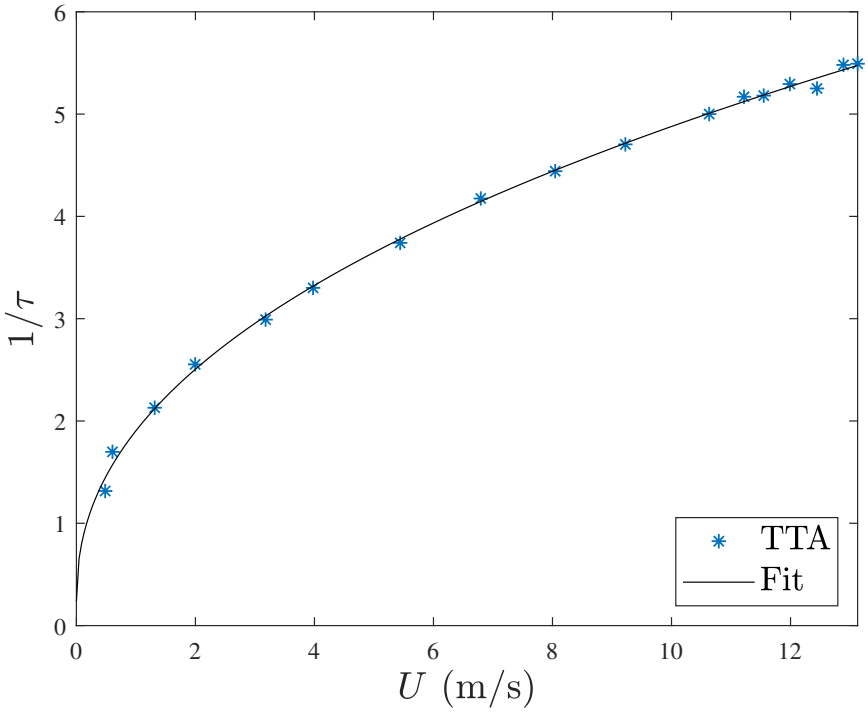

Figure A.22: TTA calibration curve for cell 22

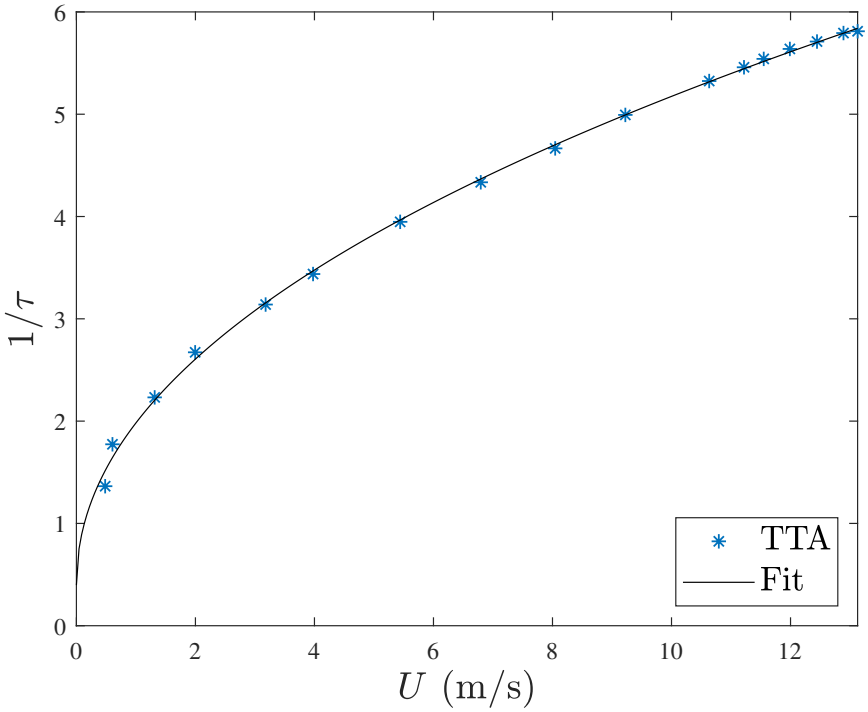

Figure A.23: TTA calibration curve for cell 23

Cell Number	A	B	C	R^2
1	0.804	0.686	1.098	0.996
2	0.979	0.616	0.999	0.998
3	1.730	0.458	0.307	0.997
4	2.088	0.394	-0.038	0.995
5	3.729	0.267	-1.632	0.995
6	1.234	0.548	0.748	1.000
7	1.342	0.516	0.650	0.999
8	1.539	0.489	0.492	0.999
9	1.652	0.460	0.389	0.999
10	1.719	0.448	0.318	0.998
11	1.585	0.479	0.397	0.999
12	1.375	0.513	0.621	0.950
13	1.261	0.538	0.707	0.998
14	1.310	0.520	0.672	0.999
15	1.662	0.464	0.295	0.999
16	1.572	0.473	0.352	0.998
17	1.668	0.445	0.237	0.998
18	1.242	0.538	0.776	0.998
19	1.355	0.520	0.560	0.994
20	1.270	0.527	0.727	0.997
21	1.446	0.500	0.416	0.997
22	1.190	0.566	0.644	0.998
23	1.320	0.526	0.601	0.998

Table A.1: Calibration constants for TTA cells

A.2 Calibration Curves with Simulation Fit

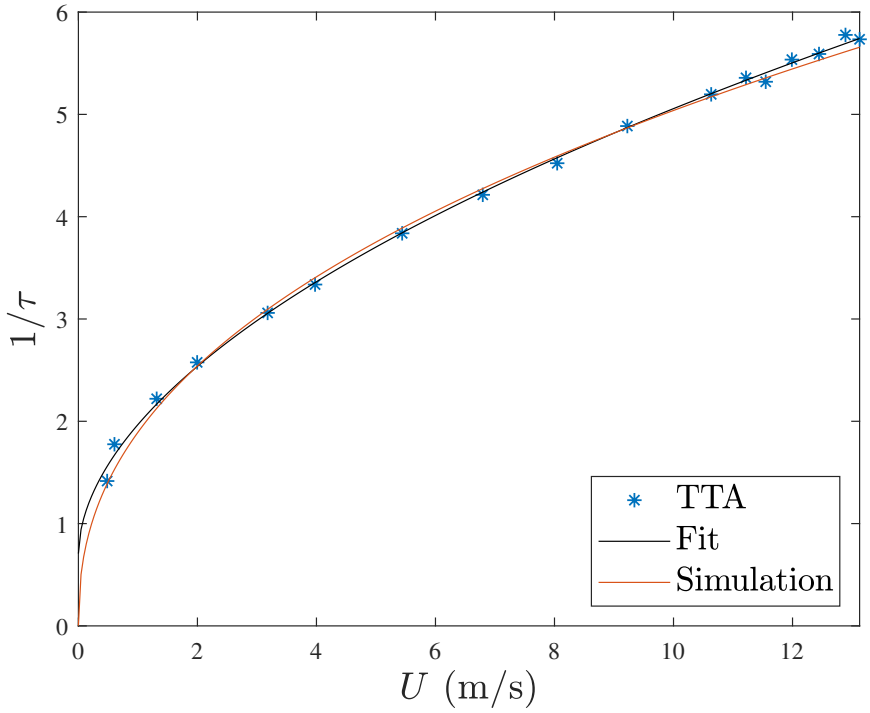

Figure A.24: Cell 13 experimental and simulated calibration

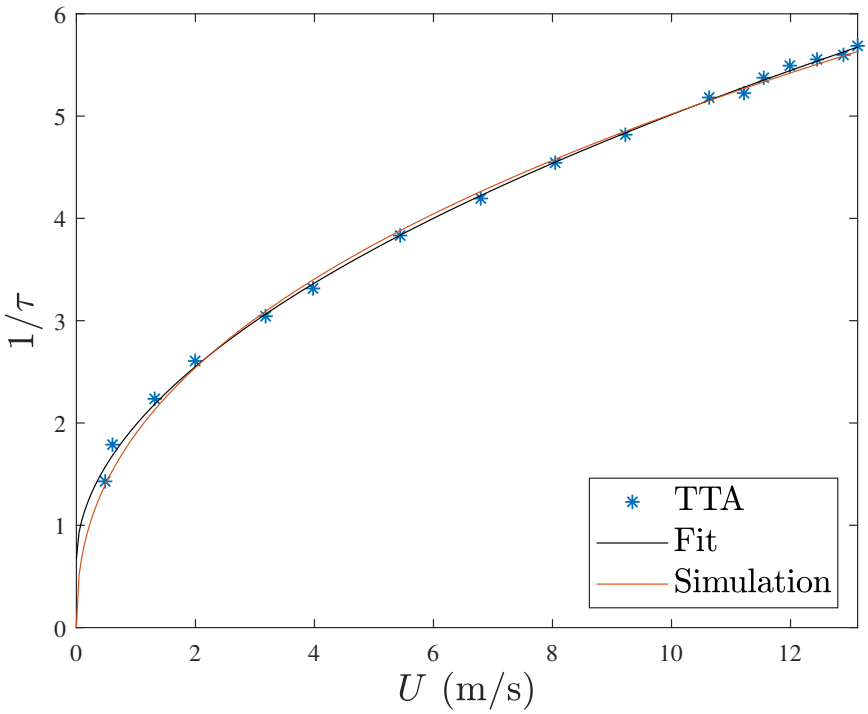

Figure A.25: Cell 14 experimental and simulated calibration

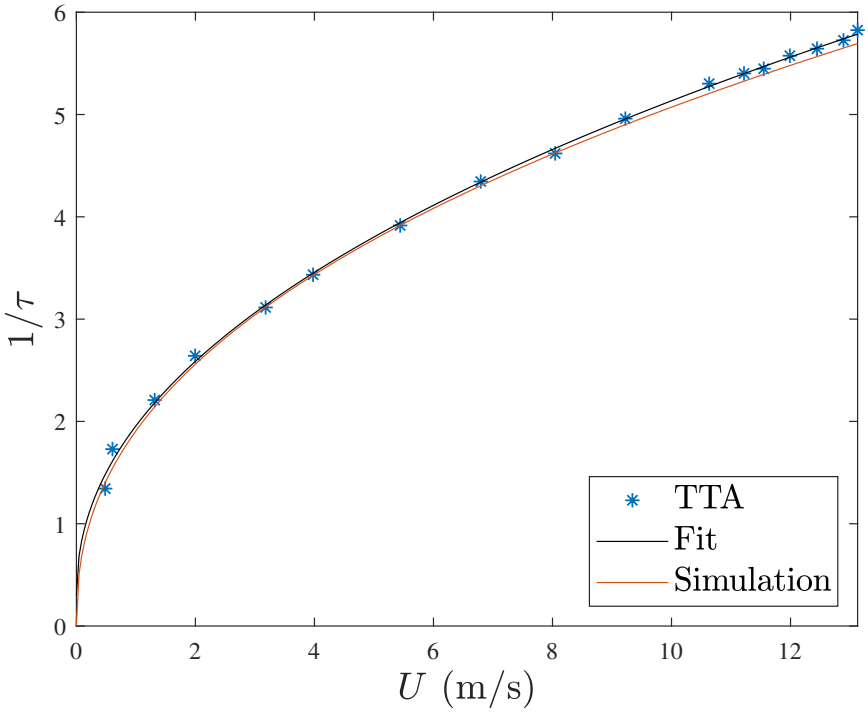

Figure A.26: Cell 15 experimental and simulated calibration

APPENDIX B

DERIVATION OF EQUATIONS

B.1 Conservation Energy Equation

Fundamental heat transfer principles are used to evaluate a segment of the wire. The energy moving through the control volume, CV, of the wire gives,

$$\dot{E_{in}} - \dot{E_{out}} + \dot{E_{gen}} = \dot{E_{stored}} \tag{B.1}$$

which is written in terms of the heat,

$$\dot{q_{conduction}} + \dot{q_{convection}} + \dot{q_{generated}} = \dot{q_{stored}}. \tag{B.2}$$

The conduction within the wire segment includes both the heat entering and exiting the wire segment, $\dot{q_{conduction,in}}$ and $\dot{q_{conduction,out}}$,

$$\dot{q_{conduction,in}} = -k(s,t)A\frac{\partial T_w(s,t)}{\partial s} \tag{B.3}$$

$$\dot{q_{conduction,out}} = -\left[k(s,t)A\frac{\partial T_w(s,t)}{\partial s} + \frac{\partial}{\partial s}\left[-k(s,t)A\frac{\partial T_w(s,t)}{\partial s}ds\right]\right] \tag{B.4}$$

where k is the thermal conductivity of the wire, A is the cross-sectional area of the wire, and T_w is the wire temperature. Combining Equations B.3 and B.4 characterizes the conduction entering and leaving the control volume,

$$\dot{q_{conduction}} = -k(s,t)A\frac{\partial T_w(s,t)}{\partial s} - \left[k(s,t)A\frac{\partial T_w(s,t)}{\partial s} + \frac{\partial}{\partial s}\left[-k(s,t)A\frac{\partial T_w(s,t)}{\partial s}ds\right]\right] \tag{B.5}$$

where k is the thermal conductivity.

The heat convection from the wire comes from the passing flow. Using Newton's law of cooling [10], the convection term is written as,

$$\dot{q_{convection}} = -h(s,t)\left[T_w(s,t) - T_a\right]dA \tag{B.6}$$

where h is the convective heat transfer coefficient and dA is the surface area of a wire segment. Substituting $dA = \pi D ds$ into Equation B.6 simplifies the convection term to,

$$\dot{q_{convection}} = -h(s,t)\pi D\left[(T_w(s,t) - T_a\right] ds. \tag{B.7}$$

The heat in the wire comes from the electrical control unit supplying a current to the wire. That is,

$$\dot{q_{generated}} = I^2 dR \tag{B.8}$$

where I is the current and dR is the resistance of the wire segment ds. The change in resistance is written in terms of the resistivity,γ, and cross-sectional area,

$$dR(s,t) = \frac{\gamma(s,t)ds}{A}. \tag{B.9}$$

This simplifies the heat generation term in Equation B.8 to,

$$\dot{q_{generated}} = \frac{I^2\gamma(s,t)ds}{A}. \tag{B.10}$$

The energy stored in the wire is,

$$\dot{q_{stored}} = mC_p\frac{\partial T_w(s,t)}{\partial t}ds \tag{B.11}$$

where m represents the mass. In terms of the density and cross-sectional area is,

$$\dot{q_{stored}} = \rho C_p A\frac{\partial T_w(s,t)}{\partial t}ds. \tag{B.12}$$

Combining all the terms together as in Equation B.2, gives Equation 4.1 (see Chapter 4.1) as,

$$\frac{1}{\rho C_p}\frac{\partial k(s,t)}{\partial s}\frac{\partial T_w(s,t)}{\partial s} + \frac{k(s,t)}{\rho C_p}\frac{\partial^2 T_w(s,t)}{\partial s^2} - \frac{4h(s,t)}{\rho C_p D}(T_w(s,t) - T_a) + 16\frac{I^2\gamma(s,t)}{\rho C_p \pi^2 D^4} = \frac{\partial T_w(s,t)}{\partial t}.$$

B.2 Thermophysical Properties of Air and Tungsten

The thermal properties for both air and tungsten are required for the simulation. The table for the tungsten properties is provided by the text *Fundamentals of Heat and Mass Transfer* [10]. A 6th and 8th order polynomial is fit thermal conductivity and specific heat,

$$\begin{aligned} k(s,t) = & \\ & -1.62*10^{-18}T_w(s,t)^6 + 7.18*10^{-15}T_w(s,t)^5 + 4.00*10^{-12}T_w(s,t)^4 \\ & -7.25*10^{-8}T_w(s,t)^3 + 1.56*10^{-4}T_w(s,t)^2 - 0.158T_w(s,t) + 175 \end{aligned} \tag{B.13}$$

$$\begin{aligned} C_p(s,t) = & \\ & -2.02*10^{-22}T_w(s,t)^8 + 1.44*10^{-18}T_w(s,t)^7 - 4.08*10^{-15}T_w(s,t)^6 \\ & +5.90*10^{-12}T_w(s,t)^5 - 4.66*10^{-9}T_w(s,t)^4 + 2.03*10^{-6}T_w(s,t)^3 \\ & -4.86*10^{-4}T_w(s,t)^2 + 81.9*10^{-3}T_w(s,t) + 131 \end{aligned} \tag{B.14}$$

where the properties are evaluated at the local temperature of the wire $T_w(s,t)$. The fitted curves along with the provided data are illustrated in Figures B.1 - B.2.

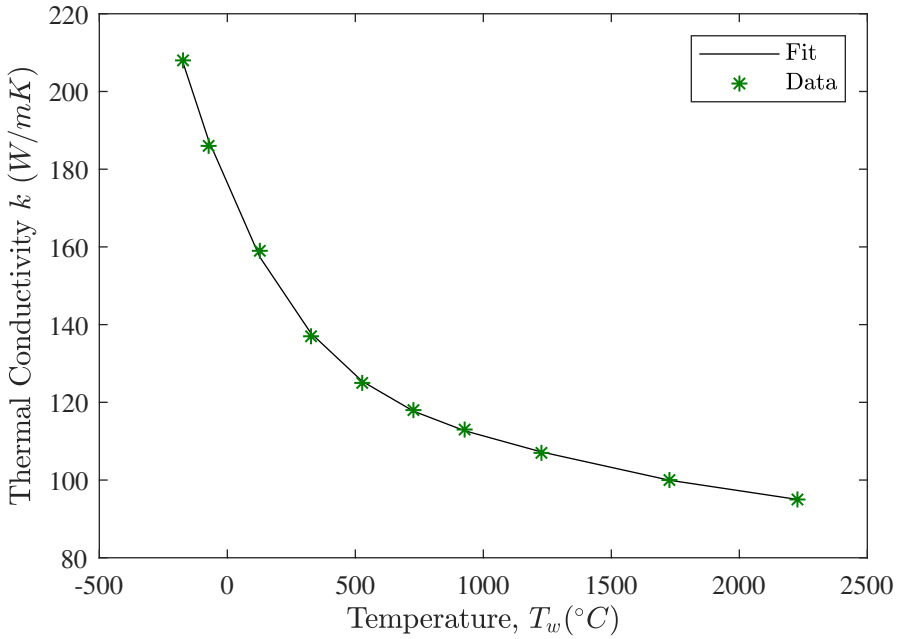

Figure B.1: Thermal conductivity fit

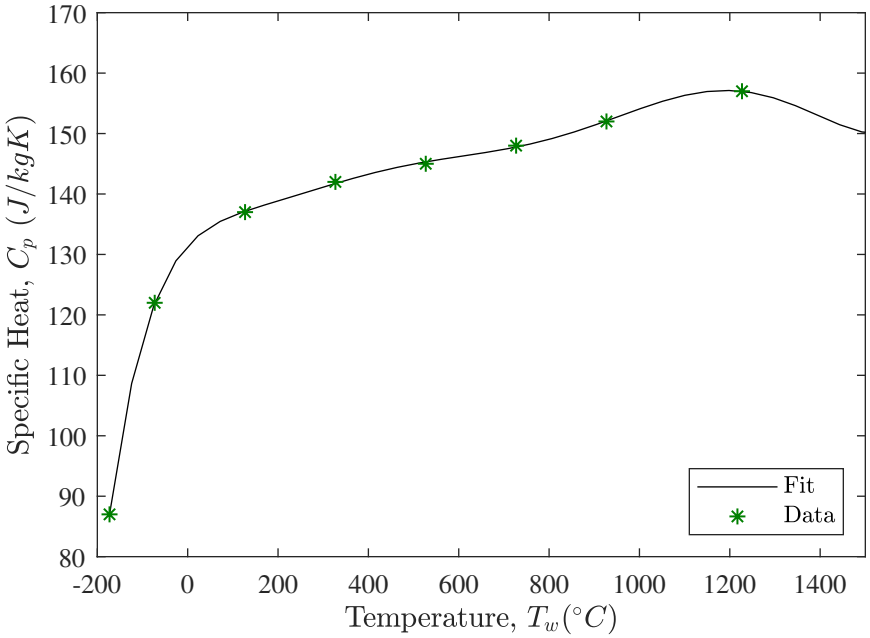

Figure B.2: Specific heat fit

A table provided by the text *Heat and Mass Transfer* [5] is used for the properties of air. A 5th and 6th order polynomial is fit to the kinematic viscosity and Prandtl numbers,

$$\begin{aligned}\nu(s,t) = \\ &2.96 * 10^{-24} T_f(s,t)^6 - 1.68 * 10^{-20} T_f(s,t)^5 + 3.88 * 10^{-17} T_f(s,t)^4 \\ &- 5.70 * 10^{-14} T_f(s,t)^3 + 1.06 * 10^{-10} T_f(s,t)^2 + 8.66 * 10^{-8} T_f(s,t) \\ &+ 1.34 * 10^{-5}\end{aligned} \tag{B.15}$$

$$\begin{aligned}Pr(s,t) = \\ &8.93 * 10^{-20} T_f(s,t)^7 - 1.70 * 10^{-16} T_f(s,t)^6 + 1.34 * 10^{-13} T_f(s,t)^5 \\ &- 5.59 * 10^{-11} T_f(s,t)^4 + 1.23 * 10^{-8} T_f(s,t)^3 - 7.57 * 10^{-7} T_f(s,t)^2 \\ &- 2.56 * 10^{-4} T_f(s,t) + 0.736\end{aligned} \tag{B.16}$$

where the properties are evaluated at the local film temperature of the wire, $T_f(s,t)$. The fitted curves along with the provided data are illustrated in Figures B.3 - B.4.

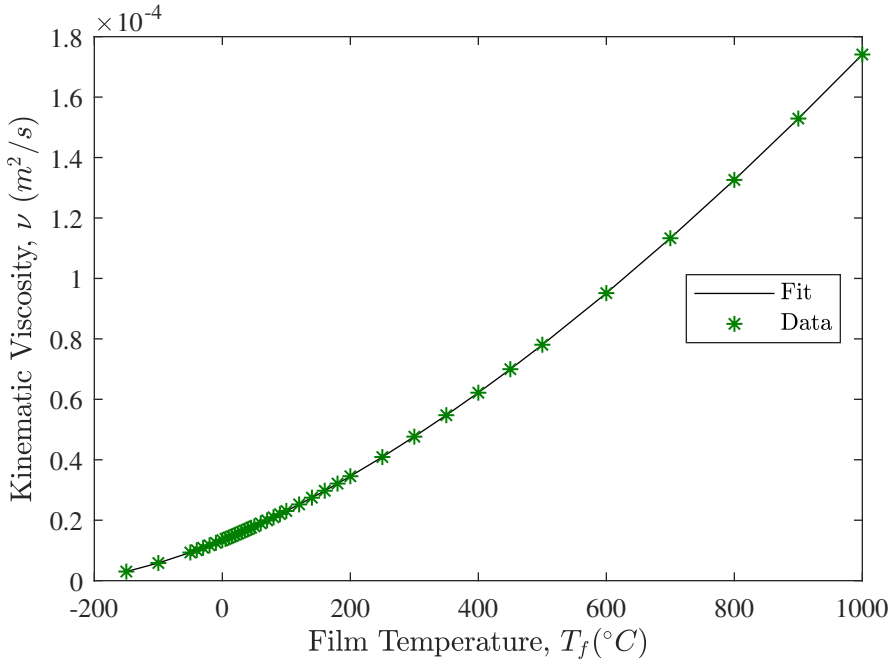

Figure B.3: Kinematic viscosity fit

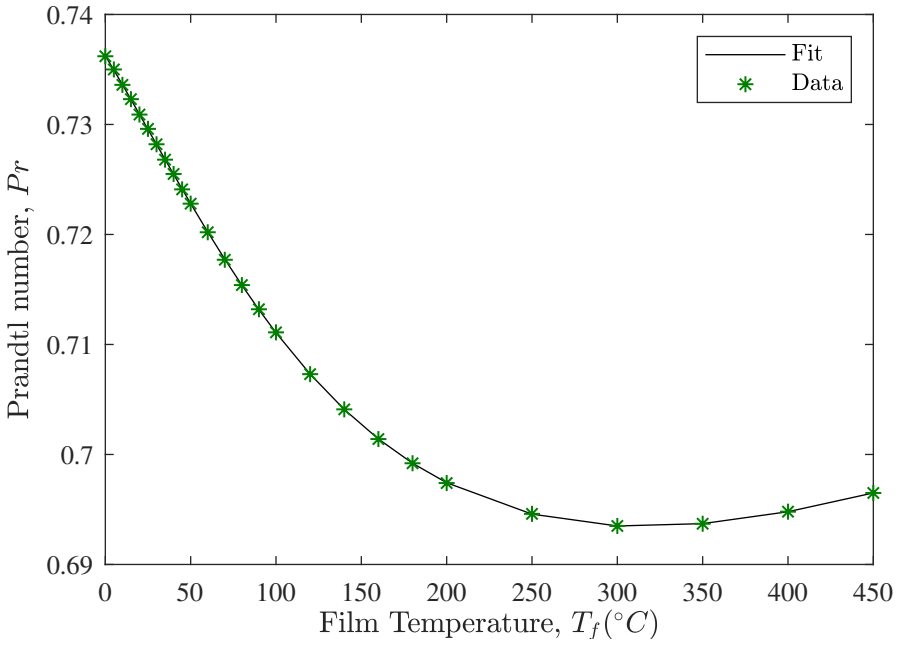

Figure B.4: Prandtl number fit

B.3 Analytical Time Constant for Uniform Flow

The conservation energy equation (Equation 4.1) can be simplified for uniform flow during the cooling period. Starting with the conservation energy equation,

$$\frac{1}{\rho C_p}\frac{\partial k(s,t)}{\partial s}\frac{\partial T_w(s,t)}{\partial s} + \frac{k(s,t)}{\rho C_p}\frac{\partial^2 T_w(s,t)}{\partial s^2} - \frac{4h(s,t)}{\rho C_p D}(T_w(s,t) - T_a) + 16\frac{I^2\gamma(s,t)}{\rho C_p \pi^2 D^4} = \frac{\partial T_w(s,t)}{\partial t}.$$

Under uniform flow, the conduction terms are removed, since the thermophysical properties are approximately constant along the wire. During the cooling process the current is approximately 0 (10 mA), thus removing the heat generation term. This leaves the conservation equation as,

$$-\frac{4h(s,t)}{\rho C_p D}(T_w(s,t) - T_a) = \frac{\partial T_w(s,t)}{\partial t}. \tag{B.17}$$

Evaluating at the initial time and rearranging gives,

$$-\frac{4h(t)}{\rho C_p D}(T_{w,0} - T_a) = T_w(t) - T_a \tag{B.18}$$

$$-\frac{4h(t)}{\rho C_p D} = \frac{T_w(t) - T_a}{T_{w,0} - T_a}. \tag{B.19}$$

The resistance varies linearly with temperature, making Equation B.19 equivalent to the dimensionless resistance (Equation 1.1). This gives,

$$-\frac{4h(t)}{\rho C_p D} = \frac{T_w(t) - T_a}{T_{w,0} - T_a} = \frac{R(t) - R_a}{R_0 - R_a} = e^{-t/\tau}. \tag{B.20}$$

Since R^* is evaluated when $e = ^{-1}$, this gives the following statement,

$$-\frac{4h(t)}{\rho C_p D} = e^{-t/\tau}. \tag{B.21}$$

Solving for the time constant by taking the natural log gives the time constant,

$$1/\tau = ln\left(\frac{4h(t)}{\rho C_p D}\right).$$

Rewriting in terms of the heat convection coefficient (Equation 4.7) gives,

$$1/\tau = ln\left(\frac{k_a c Re^m Pr^{1/3}}{\rho C_p D^2}\right). \tag{B.22}$$

B.4 Uniform Velocity Gradients

B.4.1 Horizontal Velocity Gradient

Consider the linear velocity profile imposed along the length, L, of a TTA cell (see Figure 5.1). At either end of the TTA cell, there is some minimum and maximum velocity. For a given horizontal position along the cell length, x, the relative velocity, U, is given by,

$$U = U_{min} + \frac{(U_{max} - U_{min})}{L} x. \tag{B.23}$$

Dimensionless parameters, U^* and x^*, are defined such that,

$$U^* = \frac{U}{U_{mean}} \tag{B.24}$$

$$x^* = \frac{x}{L}. \tag{B.25}$$

Substituting the dimensionless parameters U^* and x^* into Equation B.23,

$$U^* = \frac{U_{min}}{U_{mean}} + \frac{(U_{max} - U_{min})}{U_{mean}} x^*. \tag{B.26}$$

The derivative with respect to U^* and x^* is taken on either side of the Equation B.26,

$$dU^* = \frac{(U_{max} - U_{min})}{U_{mean}} dx^*. \tag{B.27}$$

Dividing both sides by dx^* gives the horizontal velocity gradient as defined in Equation 5.1,

$$\frac{dU^*}{dx^*} = \frac{(U_{max} - U_{min})}{U_{mean}}.$$

B.4.2 Vertical Velocity Gradient

The derivation of the vertical velocity gradient is similar to that of the horizontal velocity gradient. Consider the linear velocity profile imposed along the height, H, of the TTA cell (see Figure 5.6). At either end of the TTA cell, there is some minimum and maximum velocity. For a given vertical position along the cell height, y, the relative velocity, U, is given by,

$$U = U_{min} + \frac{(U_{max} - U_{min})}{H} y. \tag{B.28}$$

The dimensionless parameters are U^* and y^*, where U^* is defined in Equation B.24 and y^* is defined as,

$$y^* = \frac{y}{H}. \tag{B.29}$$

The dimensionless parameters, U^* and y^*, are substituted into Equation B.28,

$$U^* = \frac{U_{min}}{U_{mean}} + \frac{(U_{max} - U_{min}).}{U_{mean}} y^* \tag{B.30}$$

Taking the derivative (with respect to U^* and y^*) on either side of Equation B.30 and dividing both sides by dy^* (similar to Appendix B.4.1), gives the vertical velocity gradient as defined in Equation 5.2,

$$\frac{dU^*}{dy^*} = \frac{(U_{max} - U_{min})}{U_{mean}}.$$

APPENDIX C

TESTING WITH RADIATOR

C.1 Results with Radiator in Horizontal Position

C.1.1 Radiator exit plane distribution

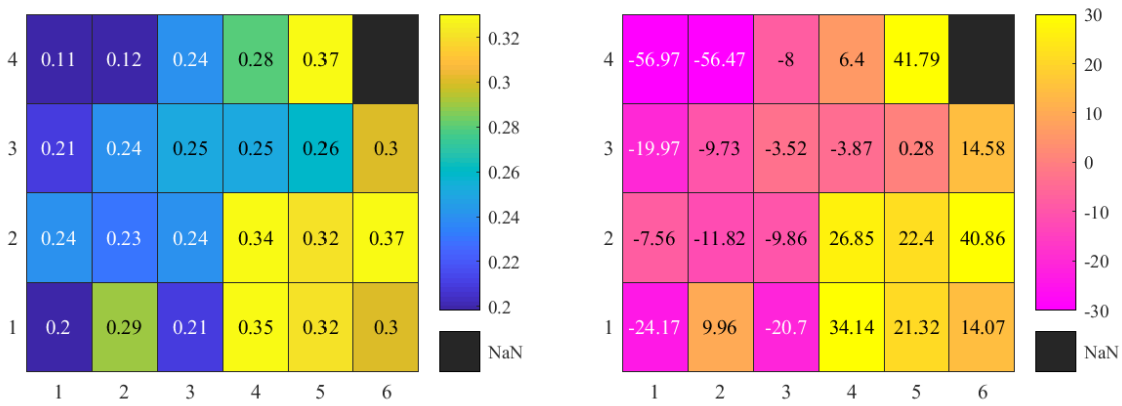

(a) Velocity (b) Percent difference

Figure C.1: Radiator exit plane flow distribution in the horizontal configuration with inlet velocity of 0.26 m/s

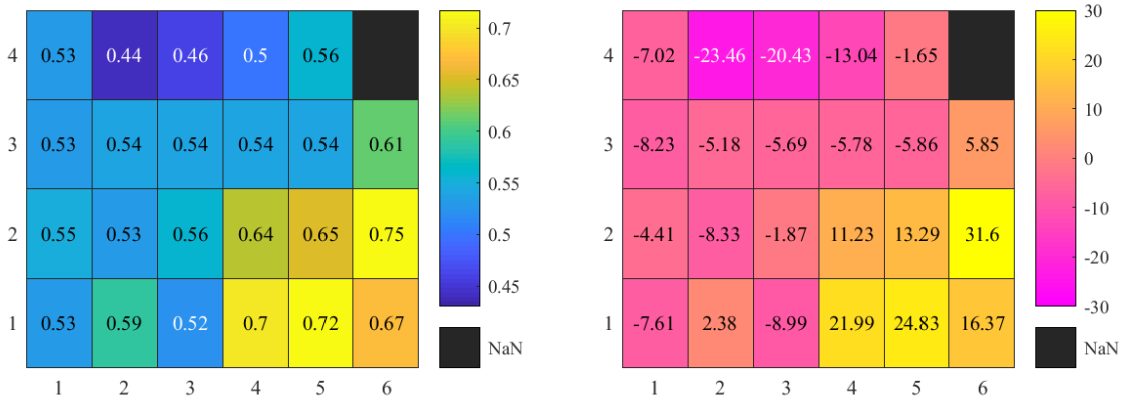

(a) Velocity (b) Percent difference

Figure C.2: Radiator exit plane flow distribution in the horizontal configuration with inlet velocity of 0.57 m/s

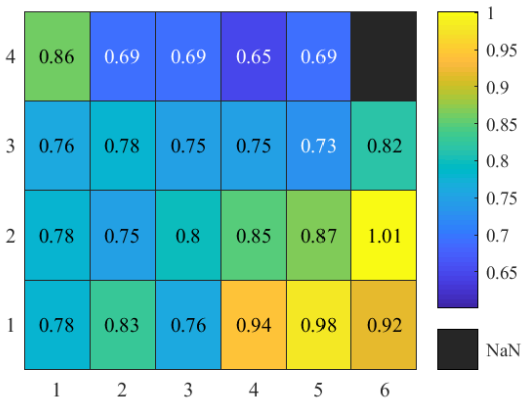

(a) Velocity

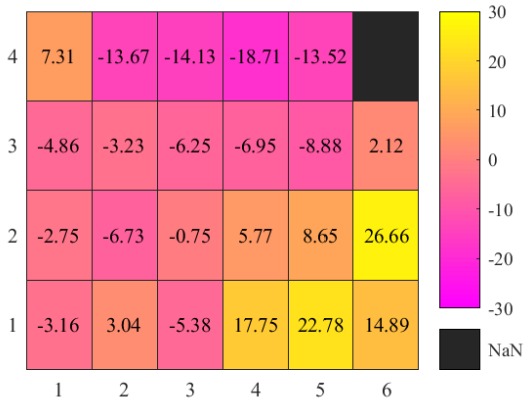

(b) Percent difference

Figure C.3: Radiator exit plane flow distribution in the horizontal configuration with inlet velocity of 0.80 m/s

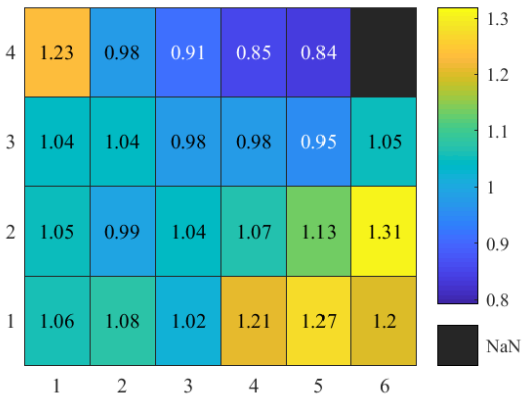

(a) Velocity

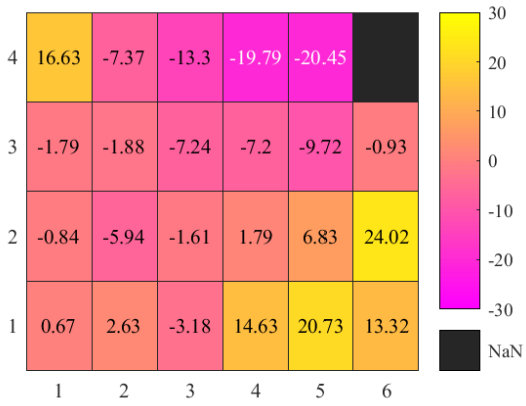

(b) Percent difference

Figure C.4: Radiator exit plane flow distribution in the horizontal configuration with inlet velocity of 1.06 m/s

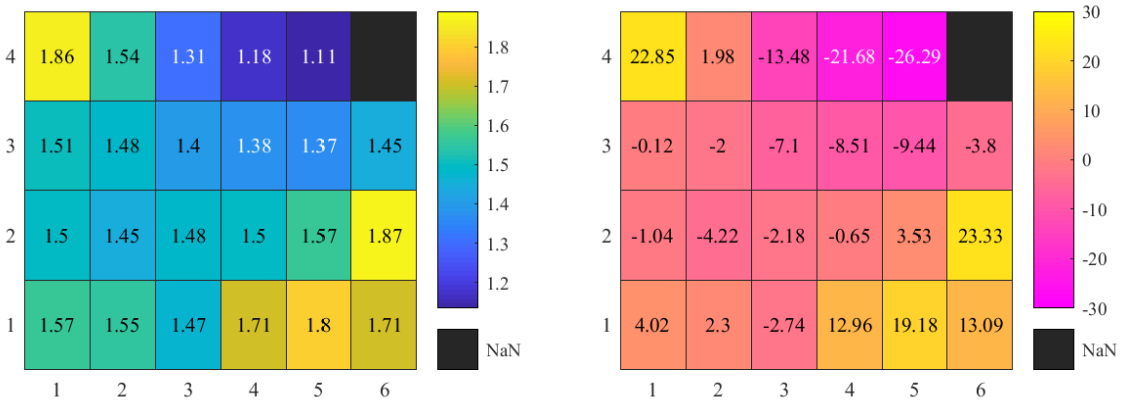

(a) Velocity (b) Percent difference

Figure C.5: Radiator exit plane flow distribution in the horizontal configuration with inlet velocity of 1.51 m/s

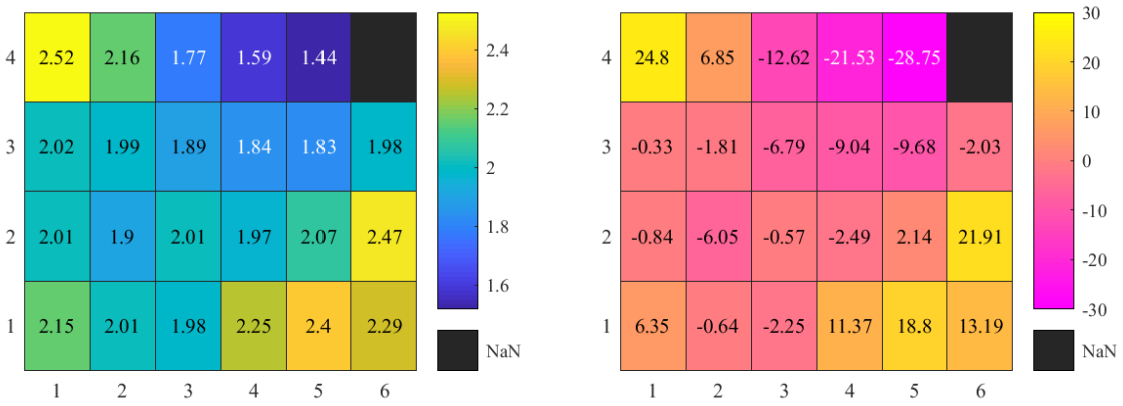

(a) Velocity (b) Percent difference

Figure C.6: Radiator exit plane flow distribution in the horizontal configuration with inlet velocity of 2.02 m/s

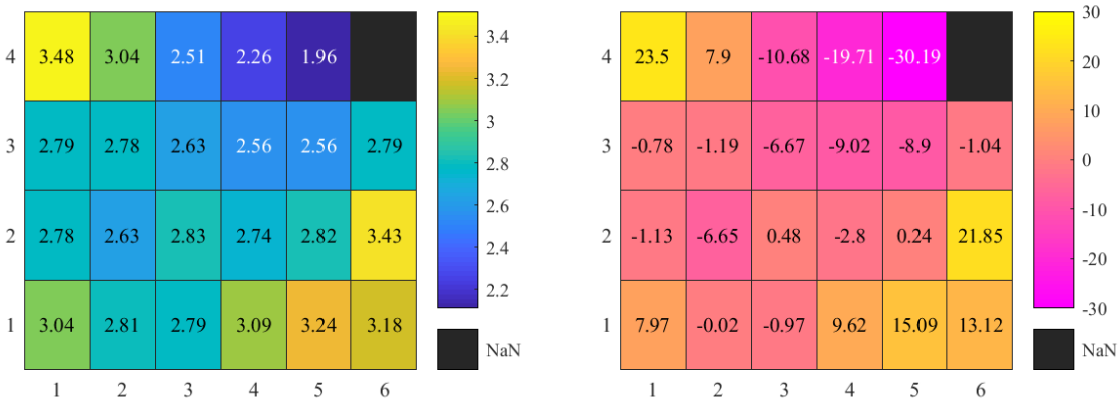

(a) Velocity (b) Percent difference

Figure C.7: Radiator exit plane flow distribution in the horizontal configuration with inlet velocity of 2.81 m/s

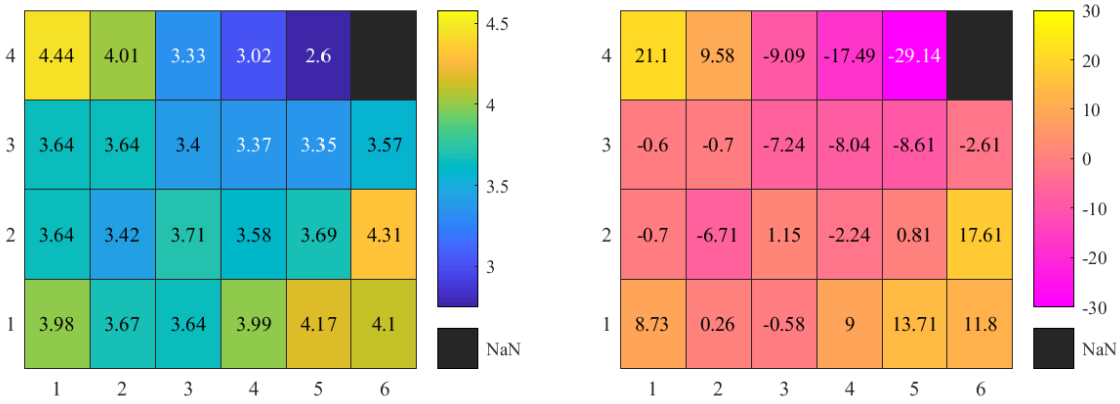

(a) Velocity (b) Percent difference

Figure C.8: Radiator exit plane flow distribution in the horizontal configuration with inlet velocity of 3.66 m/s

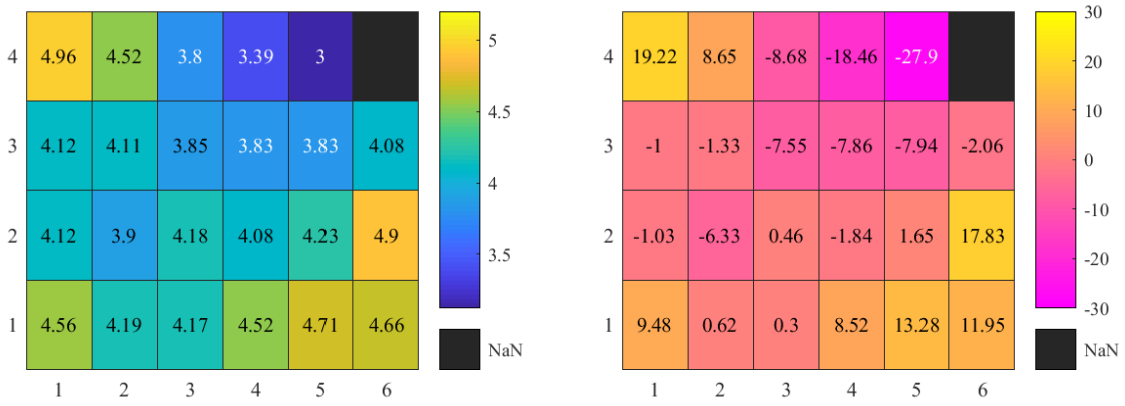

(a) Velocity (b) Percent difference

Figure C.9: Radiator exit plane flow distribution in the horizontal configuration with inlet velocity of 4.16 m/s

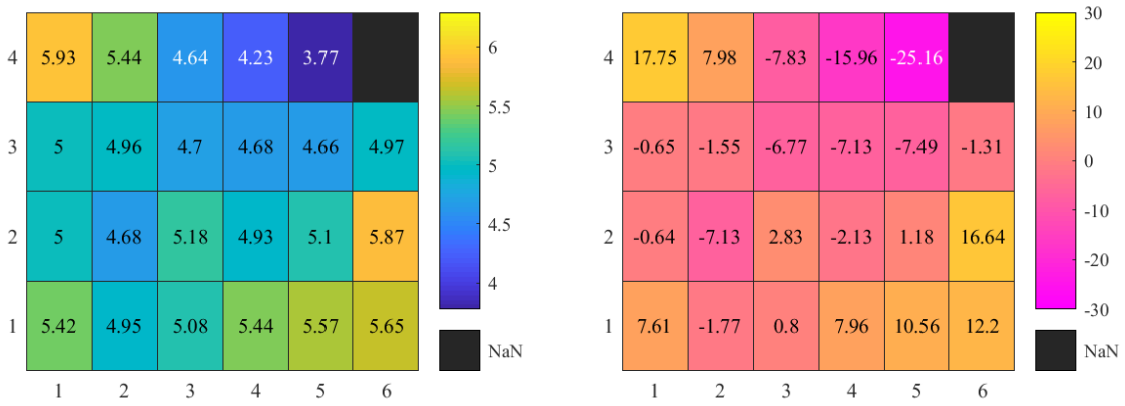

(a) Velocity (b) Percent difference

Figure C.10: Radiator exit plane flow distribution in the horizontal configuration with inlet velocity of 5.04 m/s

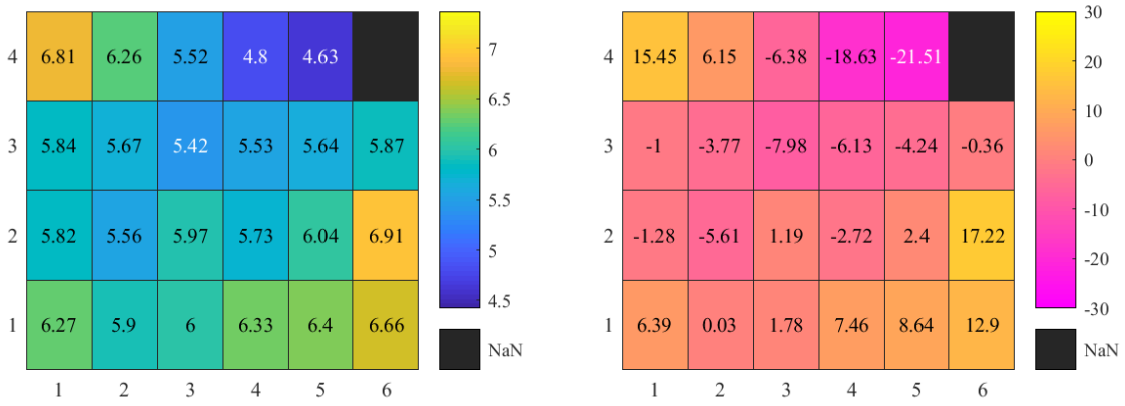

(a) Velocity (b) Percent difference

Figure C.11: Radiator exit plane flow distribution in the horizontal configuration with inlet velocity of 5.90 m/s

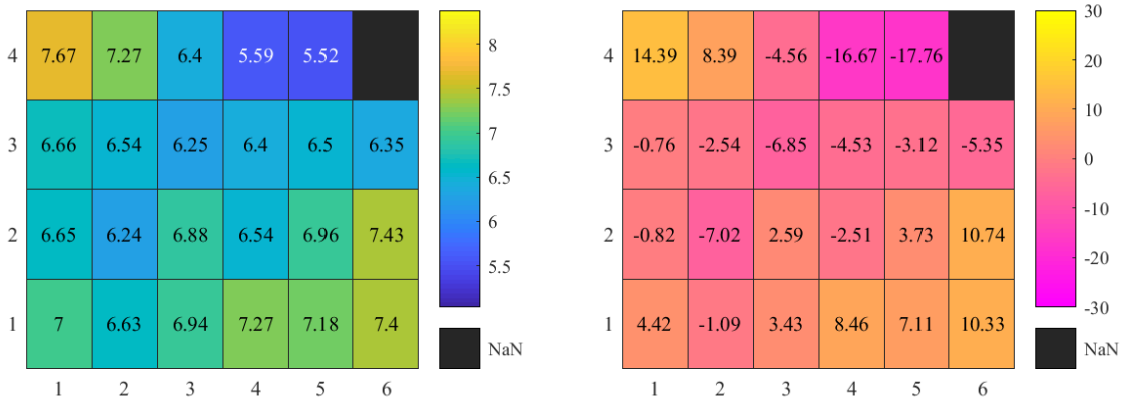

(a) Velocity (b) Percent difference

Figure C.12: Radiator exit plane flow distribution in the horizontal configuration with inlet velocity of 6.71 m/s

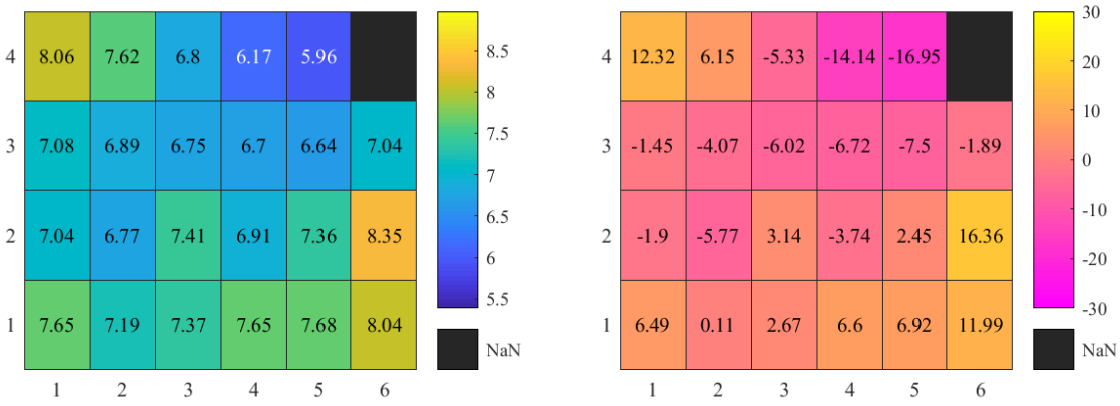

(a) Velocity (b) Percent difference

Figure C.13: Radiator exit plane flow distribution in the horizontal configuration with inlet velocity of 7.18/ m/s

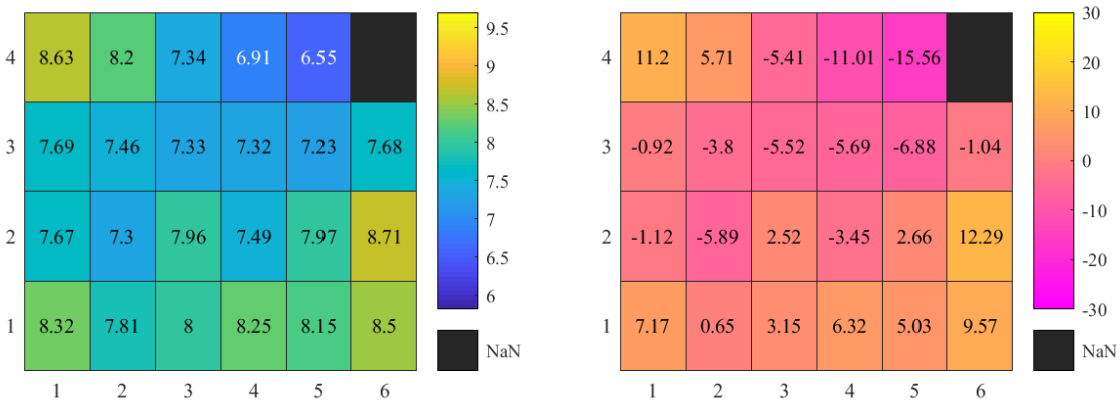

(a) Velocity (b) Percent difference

Figure C.14: Radiator exit plane flow distribution in the horizontal configuration with inlet velocity of 7.76 m/s

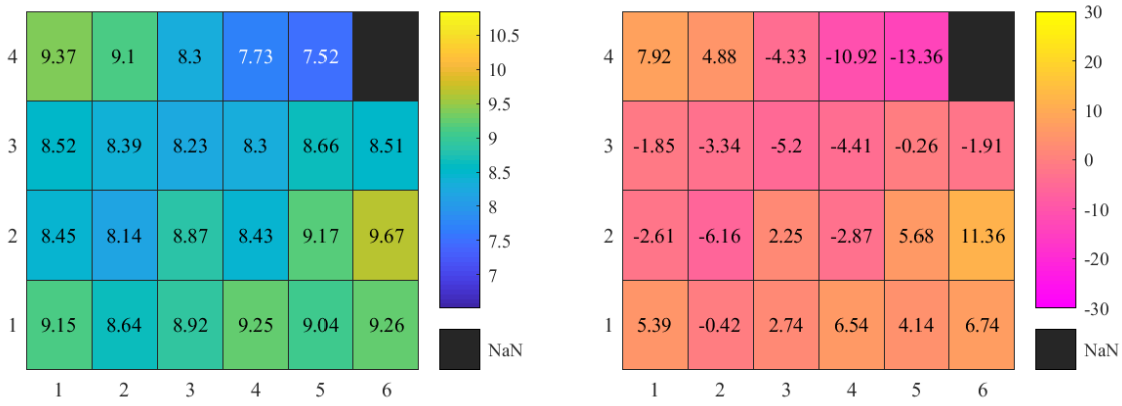

(a) Velocity (b) Percent difference

Figure C.15: Radiator exit plane flow distribution in the horizontal configuration with inlet velocity of 8.68 m/s

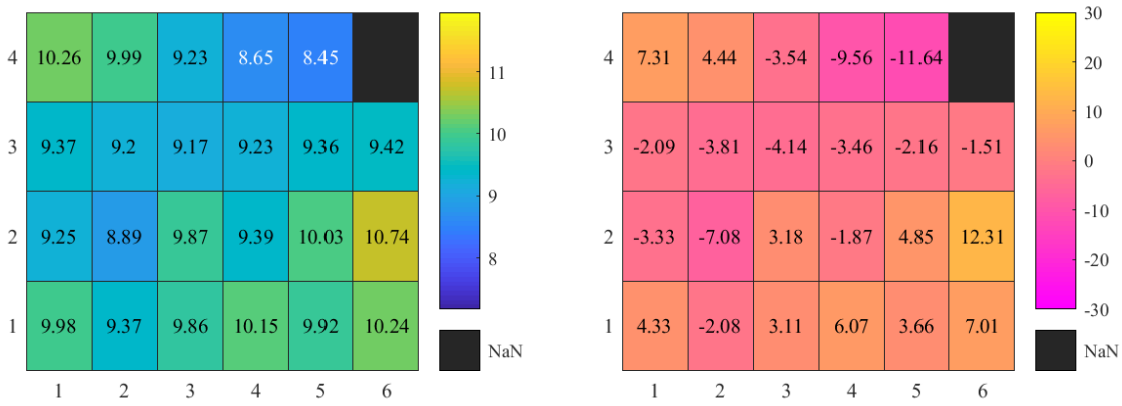

(a) Velocity (b) Percent difference

Figure C.16: Radiator exit plane flow distribution in the horizontal configuration with inlet velocity of 9.57 m/s

C.1.2 Standard Deviation of Percent Difference

Inlet Velocity (m/s)	Standard Deviation of Percent Difference (%)
0.26	26.23
0.57	14.02
0.80	11.97
1.06	11.73
1.51	12.46
2.02	12.74
2.81	12.29
3.66	11.32
4.16	11.03
5.04	10.03
5.90	9.41
6.71	8.14
7.18	8.21
7.76	7.10
8.68	6.14
9.57	5.84

Table C.1: Standard deviation of percent difference for each inlet velocity in the horizontal configuration

C.2 Results with Radiator in Inclined Position

C.2.1 Radiator Exit Plane Distribution

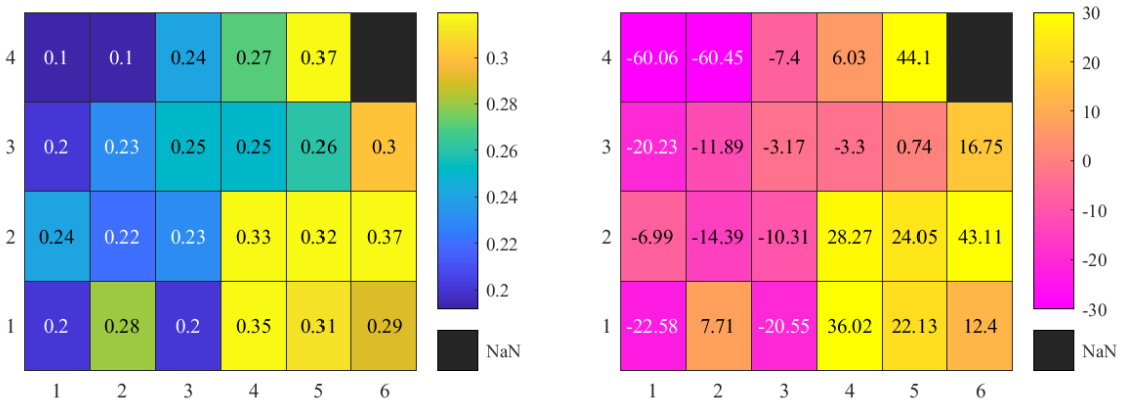

(a) Velocity (b) Percent difference

Figure C.17: Radiator exit plane flow distribution in the inclined configuration with inlet velocity of 0.26 m/s

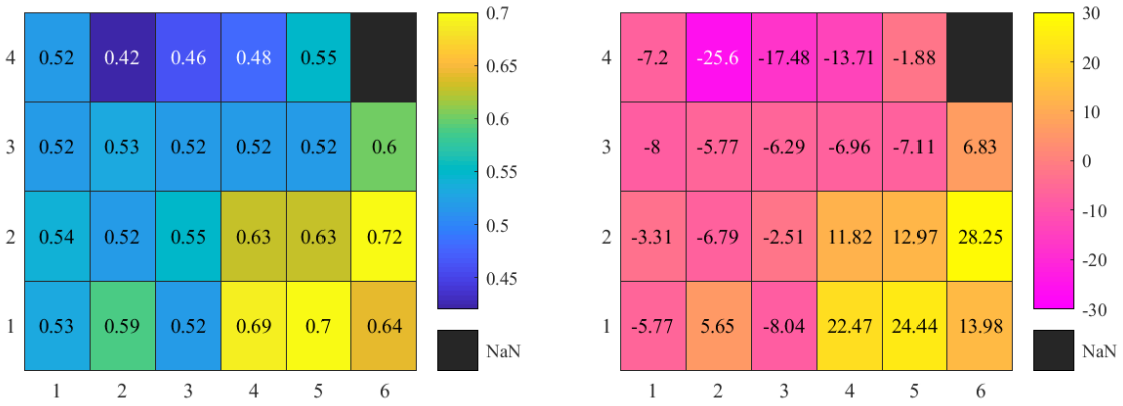

(a) Velocity (b) Percent difference

Figure C.18: Radiator exit plane flow distribution in the inclined configuration with inlet velocity of 0.56 m/s

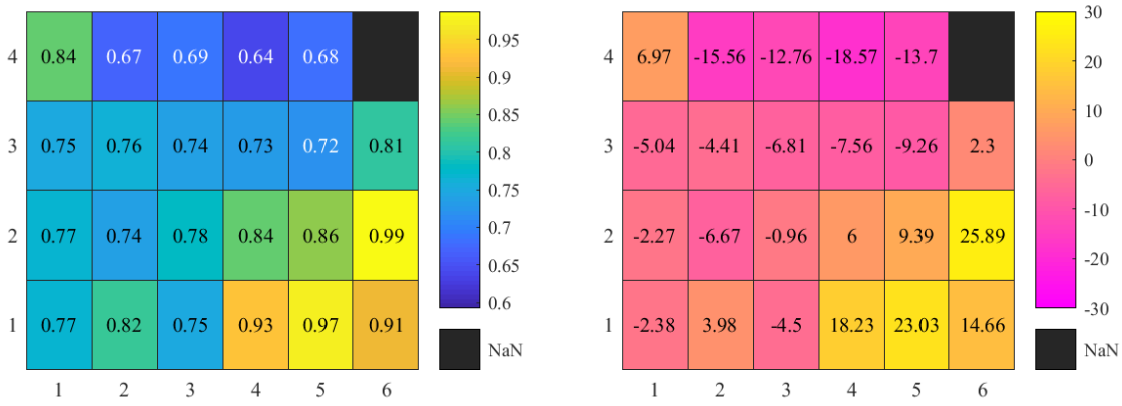

(a) Velocity (b) Percent difference

Figure C.19: Radiator exit plane flow distribution in the inclined configuration with inlet velocity of 0.79 m/s

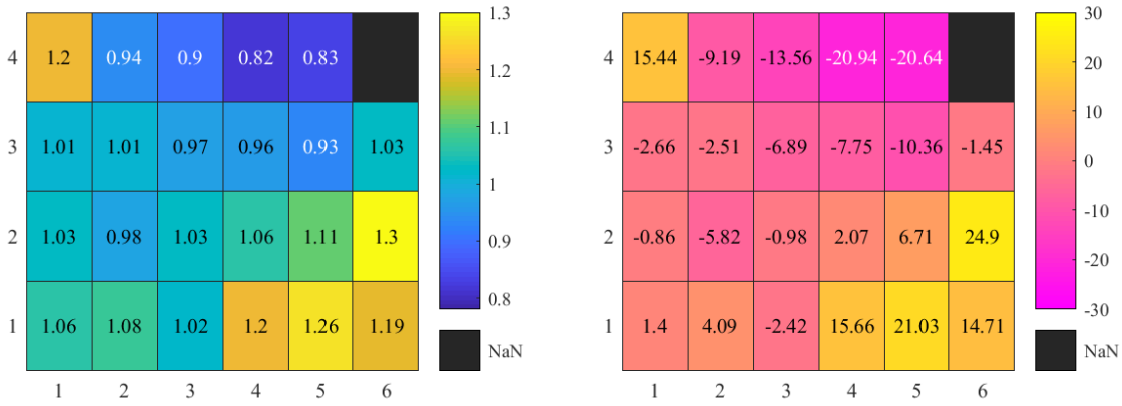

(a) Velocity (b) Percent difference

Figure C.20: Radiator exit plane flow distribution in the inclined configuration with inlet velocity of 1.04 m/s

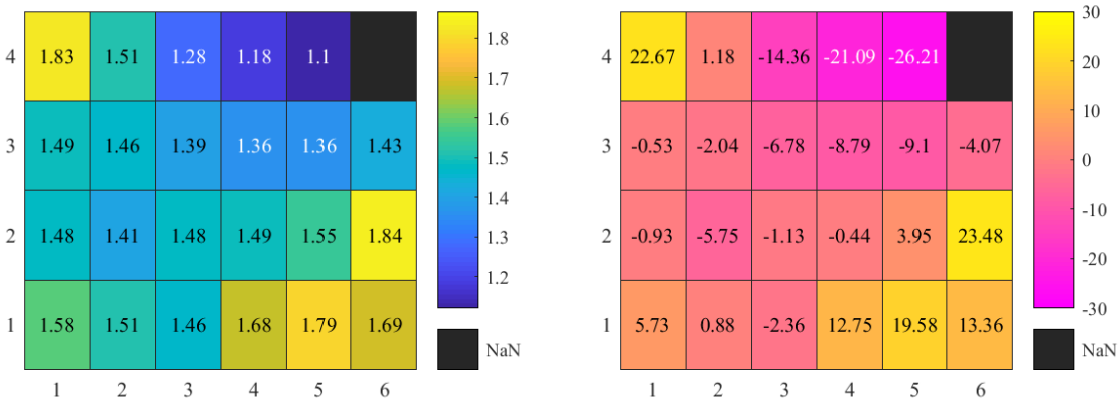

(a) Velocity (b) Percent difference

Figure C.21: Radiator exit plane flow distribution in the inclined configuration with inlet velocity of 1.49 m/s

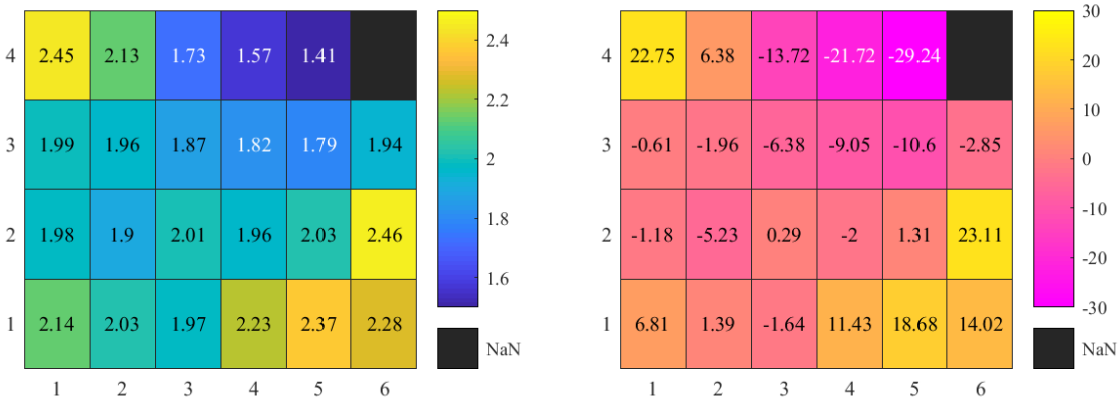

(a) Velocity (b) Percent difference

Figure C.22: Radiator exit plane flow distribution in the inclined configuration with inlet velocity of 2.00 m/s

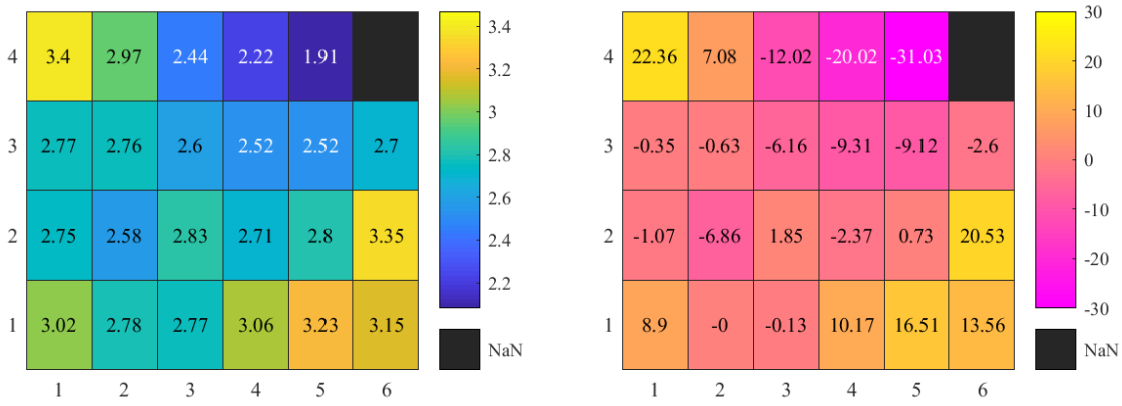

(a) Velocity (b) Percent difference

Figure C.23: Radiator exit plane flow distribution in the inclined configuration with inlet velocity of 2.78 m/s

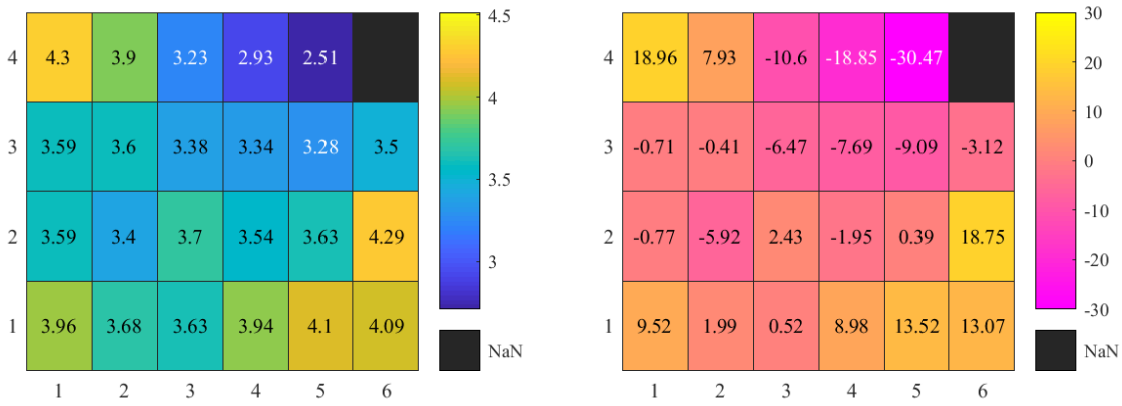

(a) Velocity (b) Percent difference

Figure C.24: Radiator exit plane flow distribution in the inclined configuration with inlet velocity of 3.61 m/s

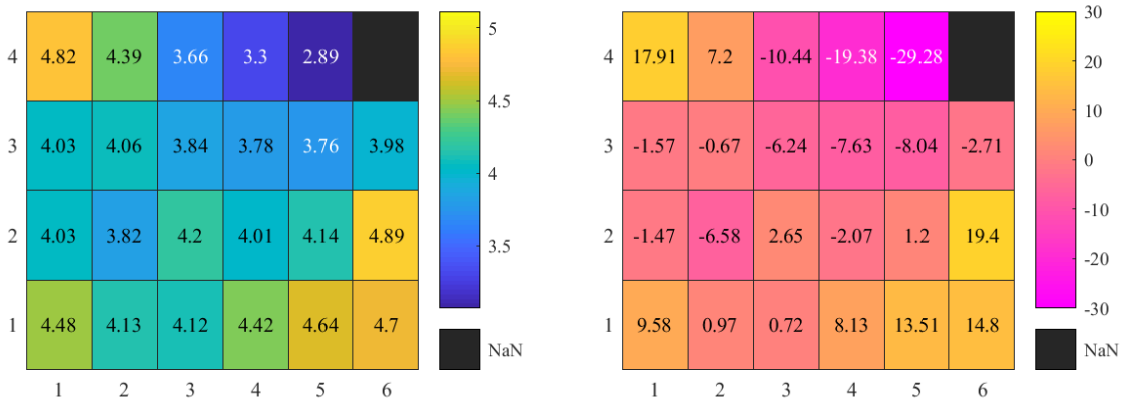

(a) Velocity (b) Percent difference

Figure C.25: Radiator exit plane flow distribution in the inclined configuration with inlet velocity of 4.09 m/s

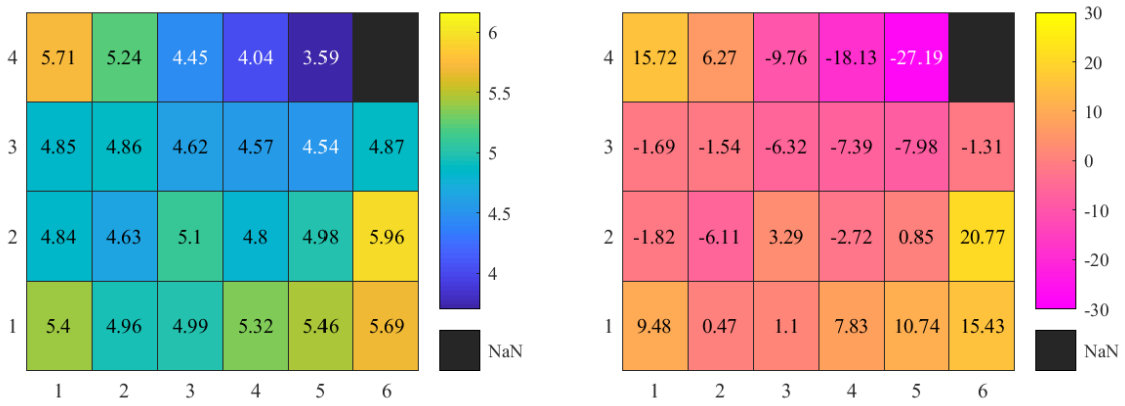

(a) Velocity (b) Percent difference

Figure C.26: Radiator exit plane flow distribution in the inclined configuration with inlet velocity of 4.93 m/s

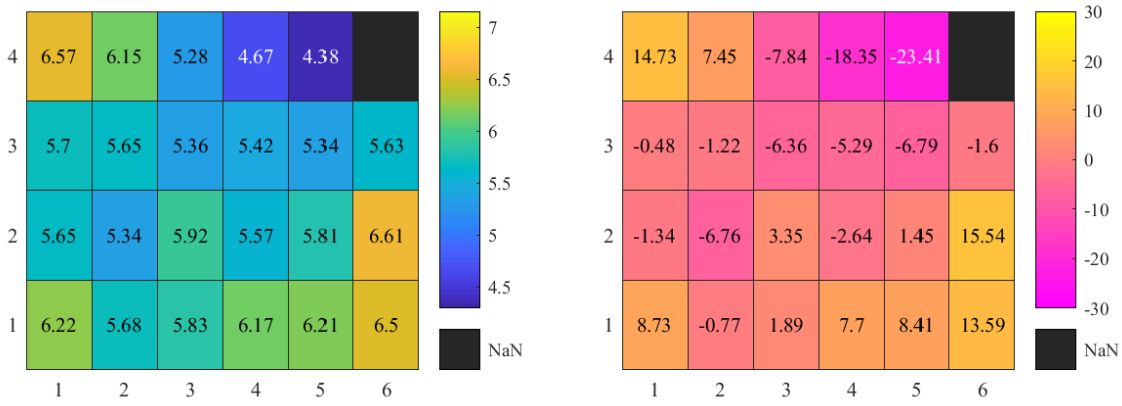

(a) Velocity (b) Percent difference

Figure C.27: Radiator exit plane flow distribution in the inclined configuration with inlet velocity of 5.72 m/s

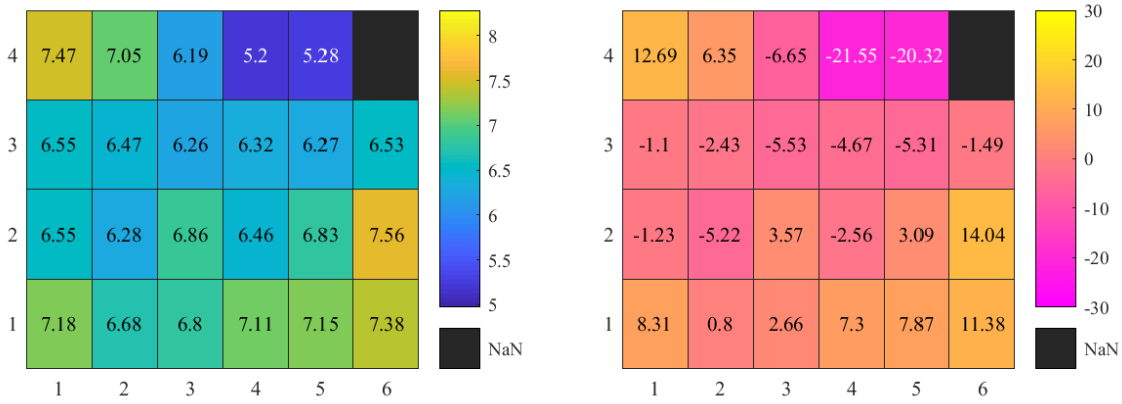

(a) Velocity (b) Percent difference

Figure C.28: Radiator exit plane flow distribution in the inclined configuration with inlet velocity of 6.63 m/s

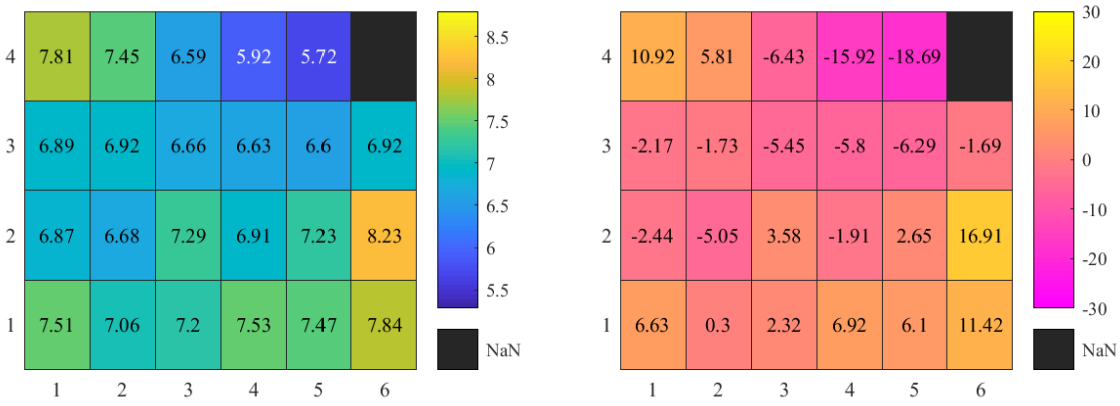

(a) Velocity (b) Percent difference

Figure C.29: Radiator exit plane flow distribution in the inclined configuration with inlet velocity of 7.04 m/s

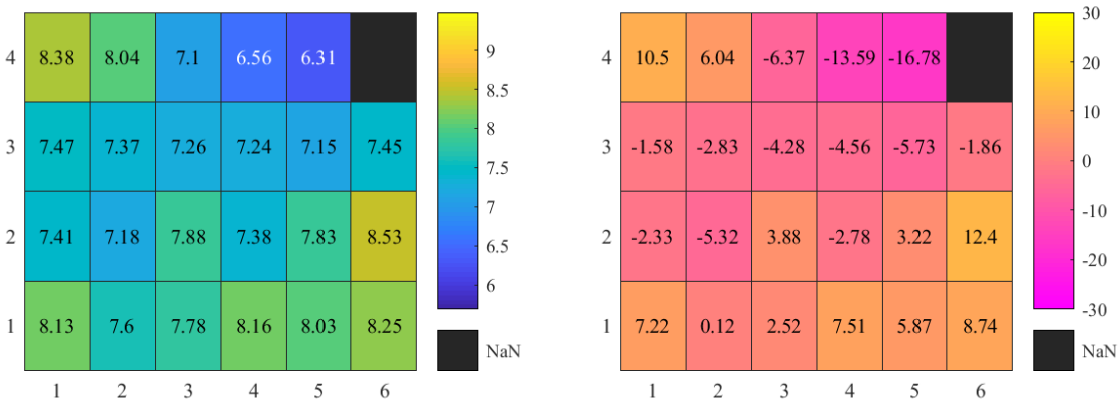

(a) Velocity (b) Percent difference

Figure C.30: Radiator exit plane flow distribution in the inclined configuration with inlet velocity of 7.59 m/s

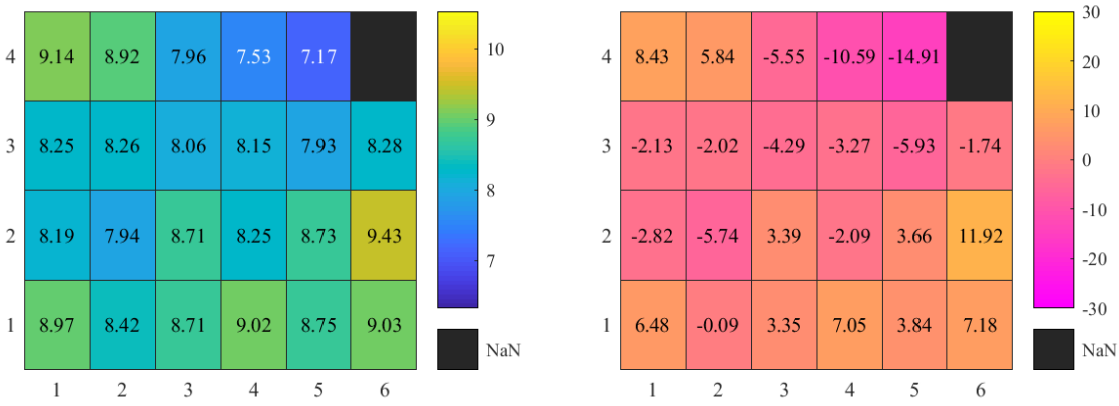

(a) Velocity (b) Percent difference

Figure C.31: Radiator exit plane flow distribution in the inclined configuration with inlet velocity of 8.43 m/s

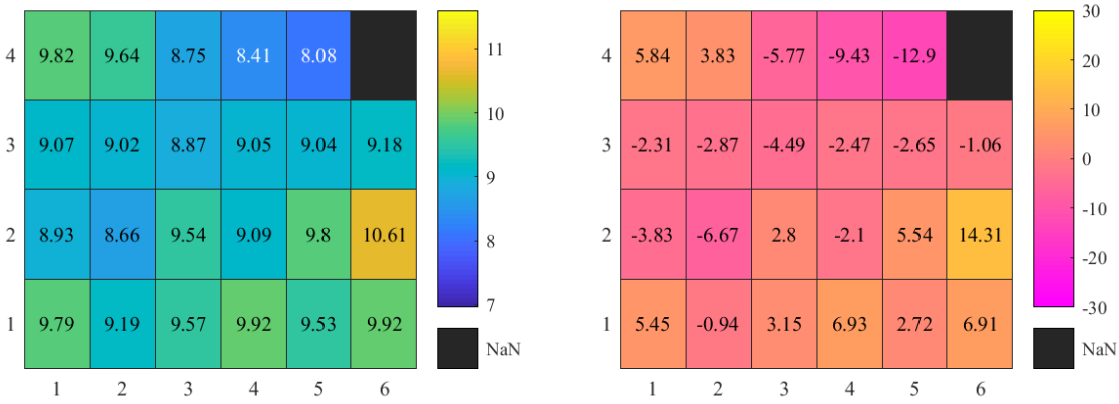

(a) Velocity (b) Percent difference

Figure C.32: Radiator exit plane flow distribution in the inclined configuration with inlet velocity of 9.28 m/s

C.2.2 Standard Deviation of Percent Difference

Inlet Velocity (m/s)	Standard Deviation of Percent Difference (%)
0.26	27.54
0.56	13.62
0.70	12.04
1.04	12.13
1.49	12.52
2.00	12.82
2.78	12.42
3.61	11.56
4.09	11.45
4.93	10.90
5.72	9.63
6.63	9.02
7.04	8.30
7.59	7.34
8.43	6.49
9.28	6.16

Table C.2: Standard Deviation of percent difference for each inlet velocity in the inclined configuration

C.2.3 Cell Velocity vs. Inlet Velocity in Horizontal and Inclined Positions with 95% Confidence Intervals

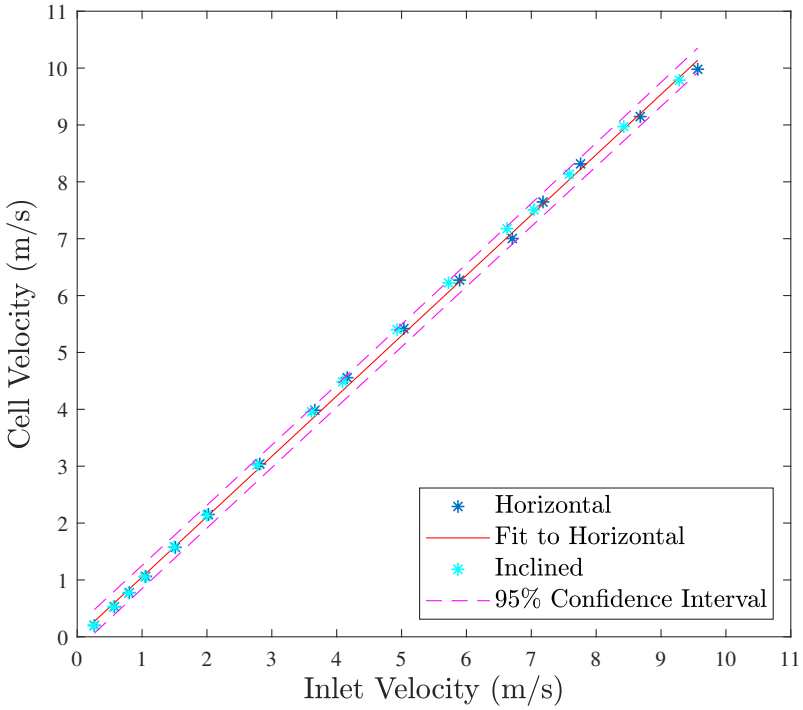

Figure C.33: Cell velocity vs. inlet velocity with 95% confidence intervals for cell 1

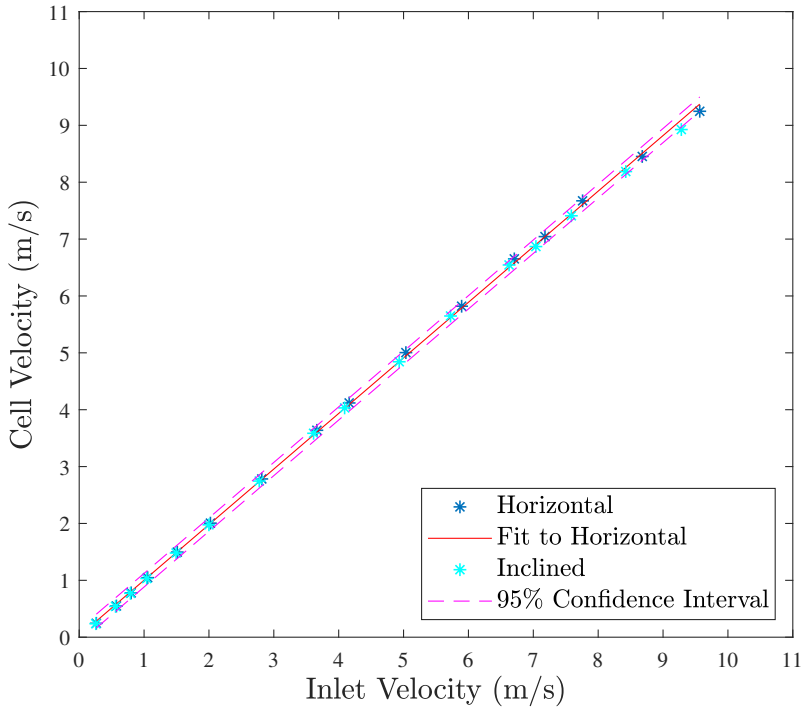

Figure C.34: Cell velocity vs. inlet velocity with 95% confidence intervals for cell 2

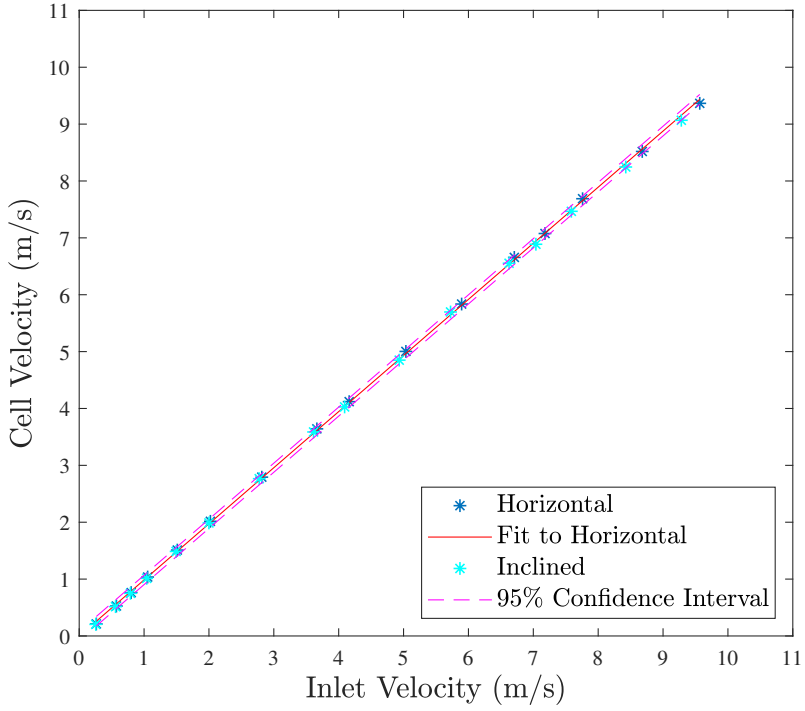

Figure C.35: Cell velocity vs. inlet velocity with 95% confidence intervals for cell 3

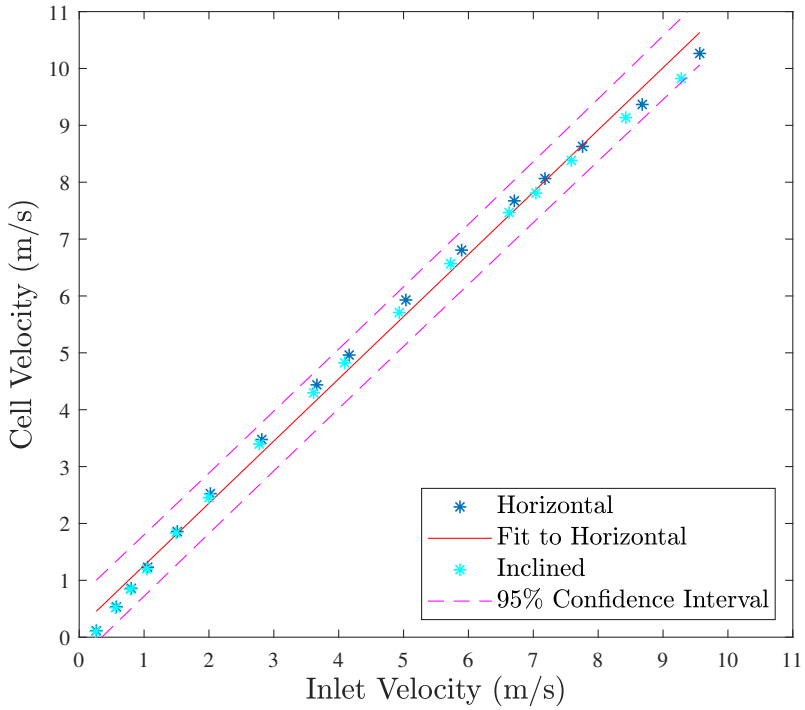

Figure C.36: Cell velocity vs. inlet velocity with 95% confidence intervals for cell 4

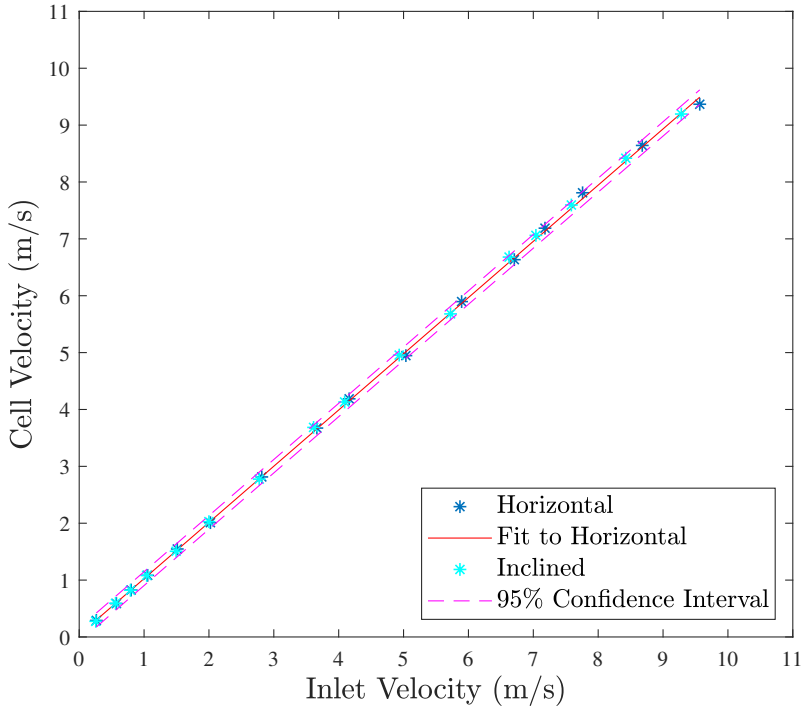

Figure C.37: Cell velocity vs. inlet velocity with 95% confidence intervals for cell 5

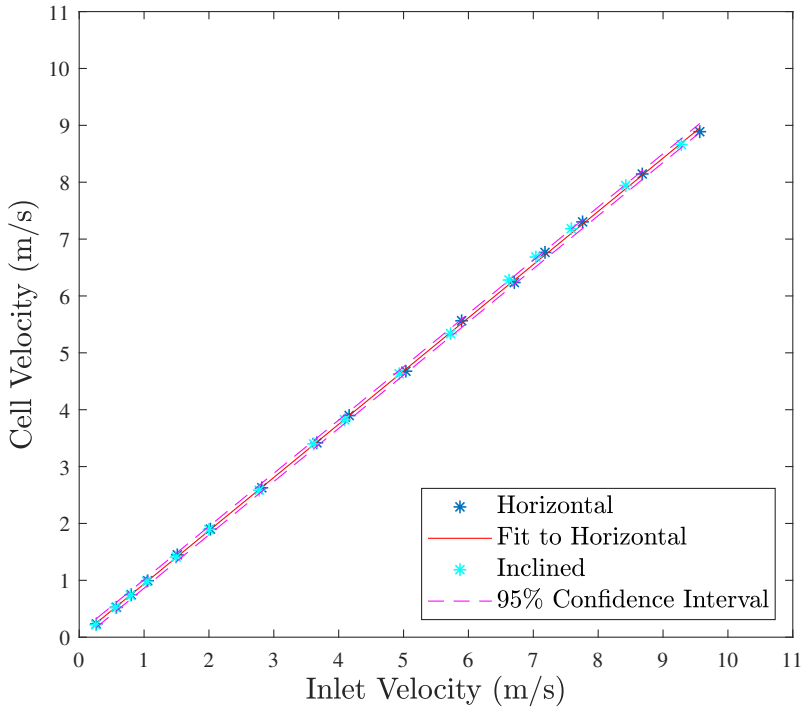

Figure C.38: Cell velocity vs. inlet velocity with 95% confidence intervals for cell 6

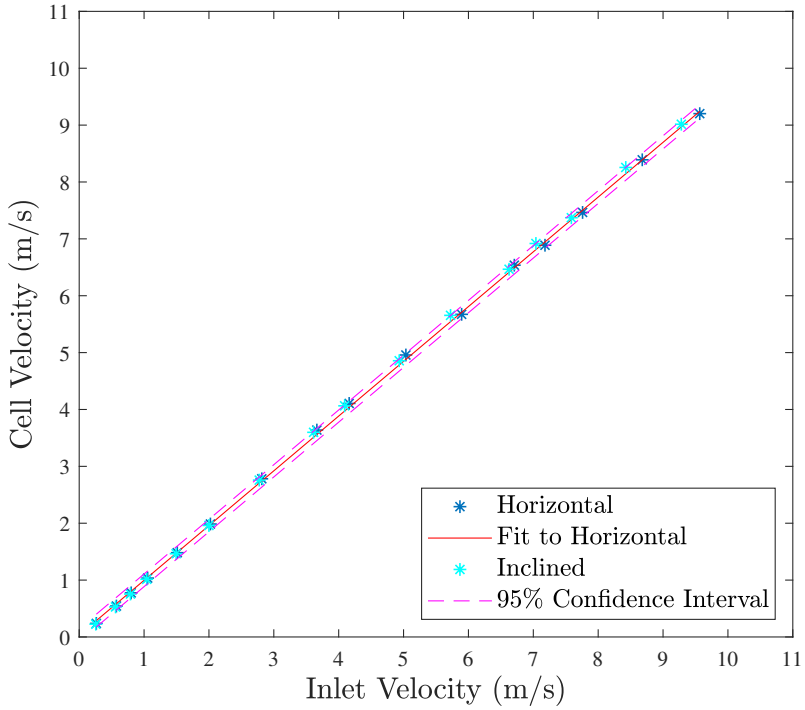

Figure C.39: Cell velocity vs. inlet velocity with 95% confidence intervals for cell 7

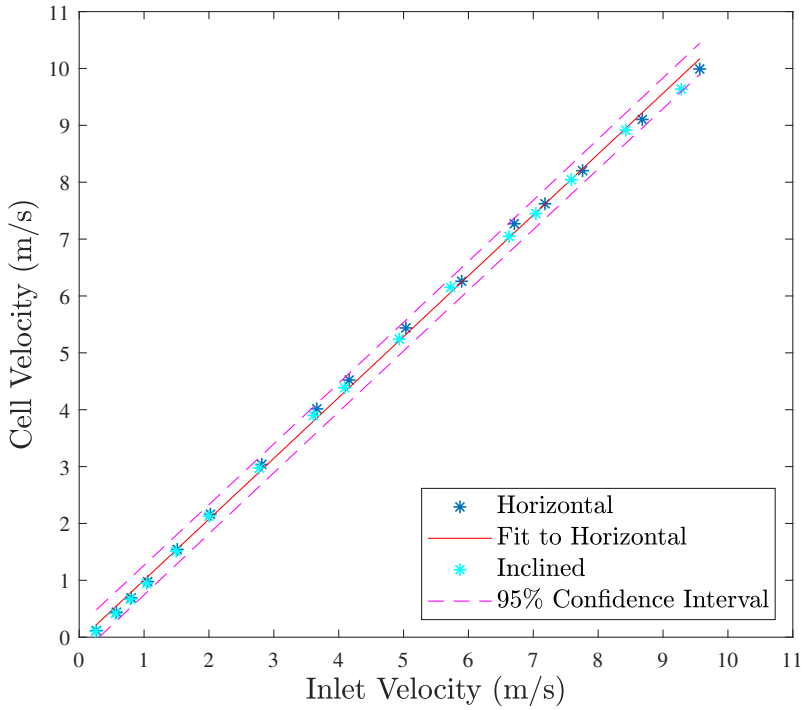

Figure C.40: Cell velocity vs. inlet velocity with 95% confidence intervals for cell 8

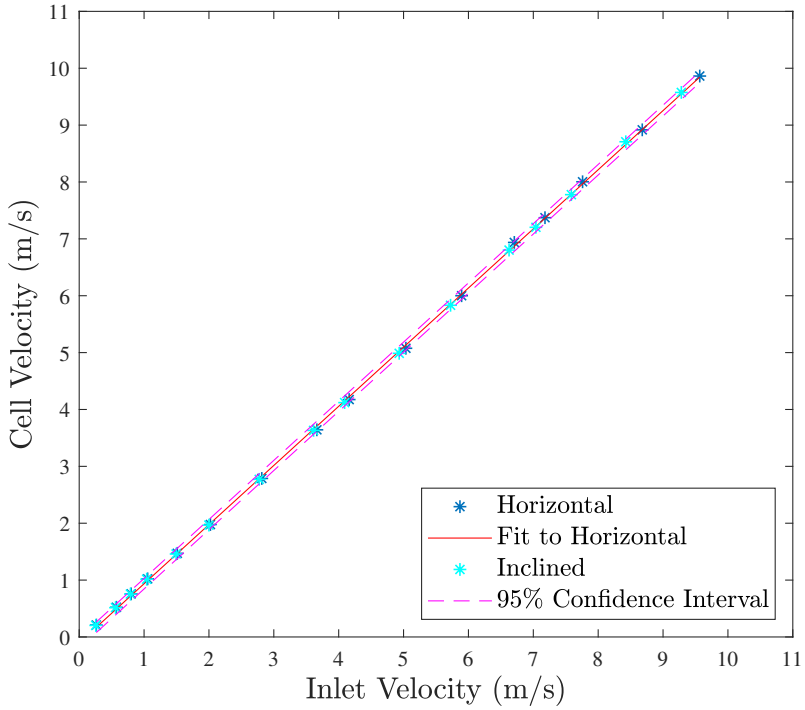

Figure C.41: Cell velocity vs. inlet velocity with 95% confidence intervals for cell 9

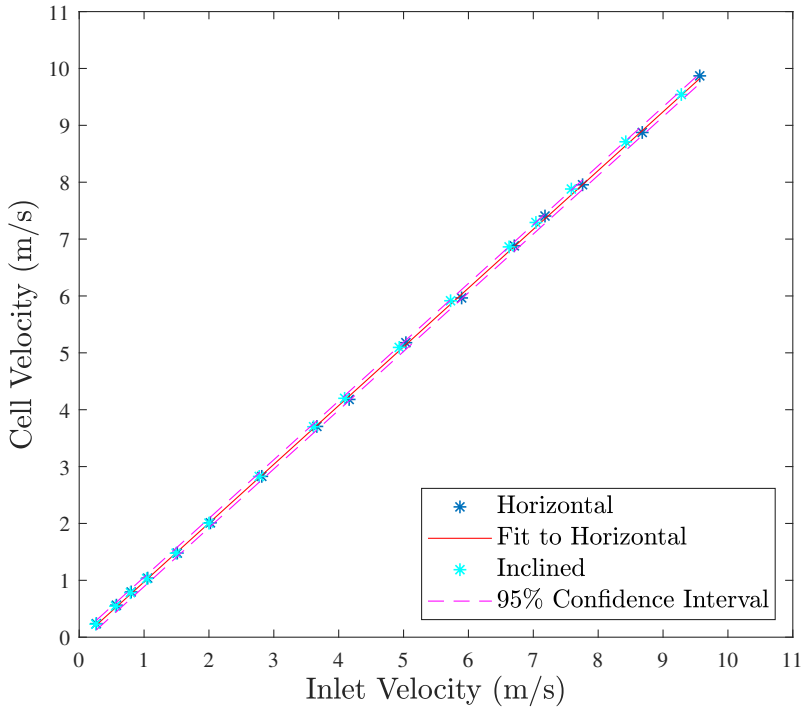

Figure C.42: Cell velocity vs. inlet velocity with 95% confidence intervals for cell 10

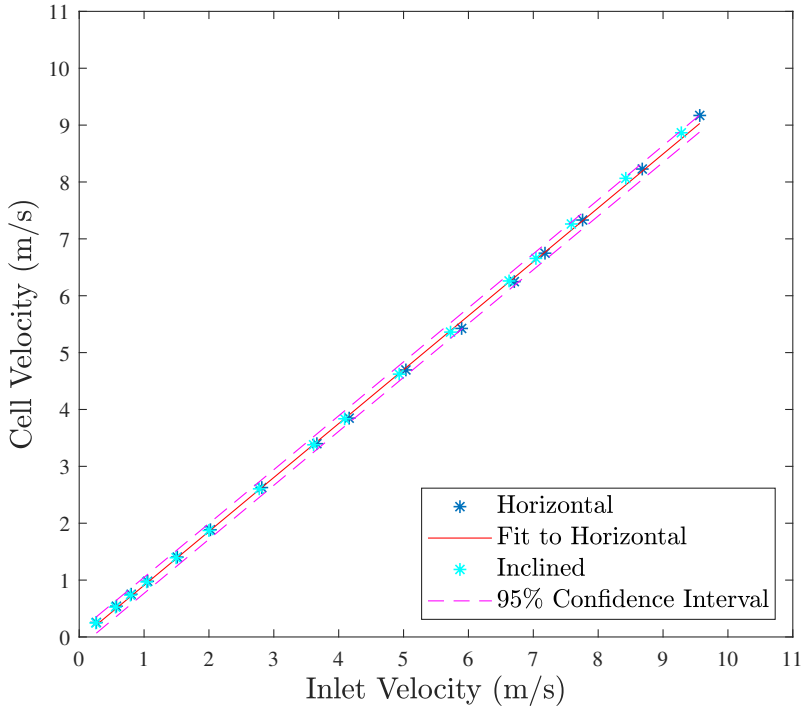

Figure C.43: Cell velocity vs. inlet velocity with 95% confidence intervals for cell 11

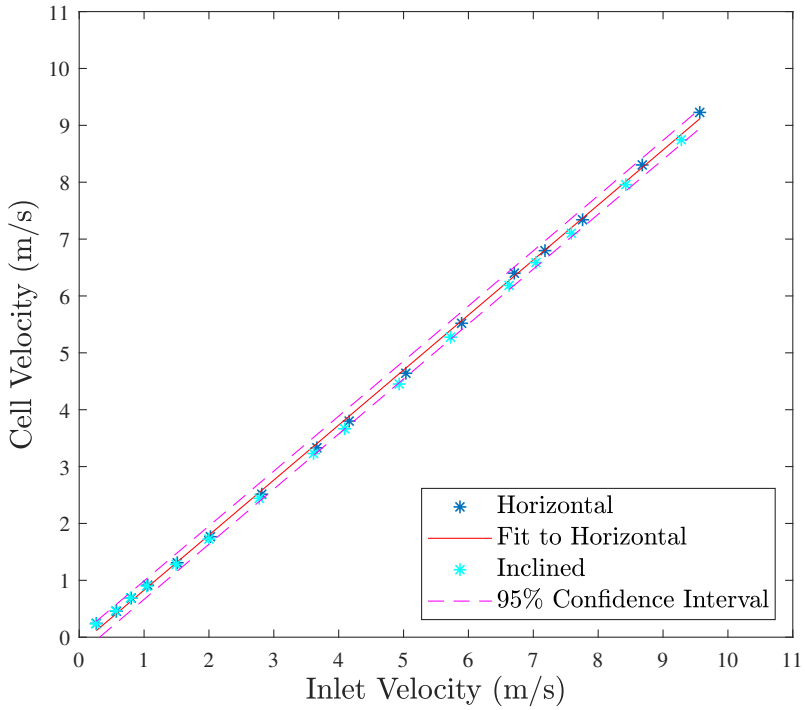

Figure C.44: Cell velocity vs. inlet velocity with 95% confidence intervals for cell 12

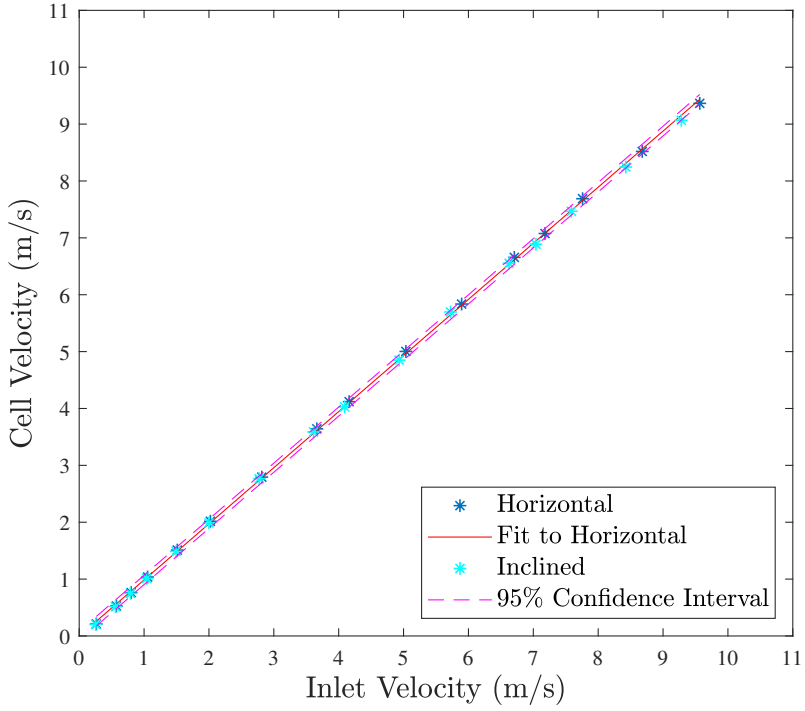

Figure C.45: Cell velocity vs. inlet velocity with 95% confidence intervals for cell 13

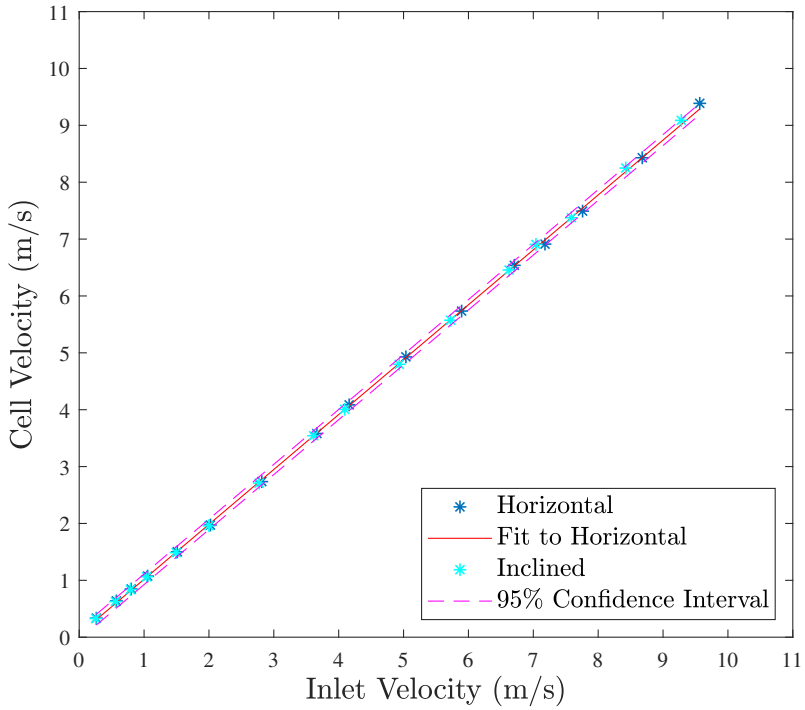

Figure C.46: Cell velocity vs. inlet velocity with 95% confidence intervals for cell 14

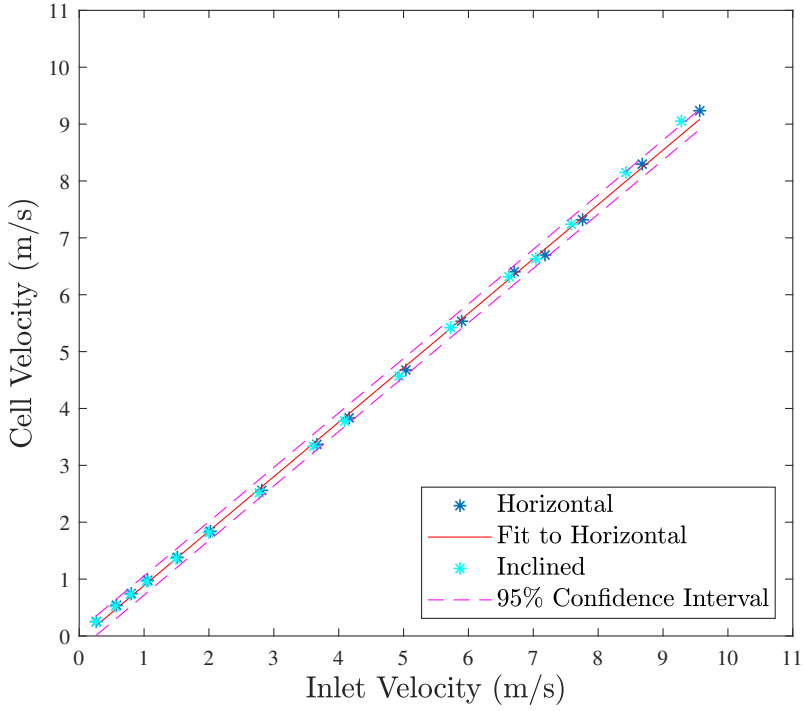

Figure C.47: Cell velocity vs. inlet velocity with 95% confidence intervals for cell 15

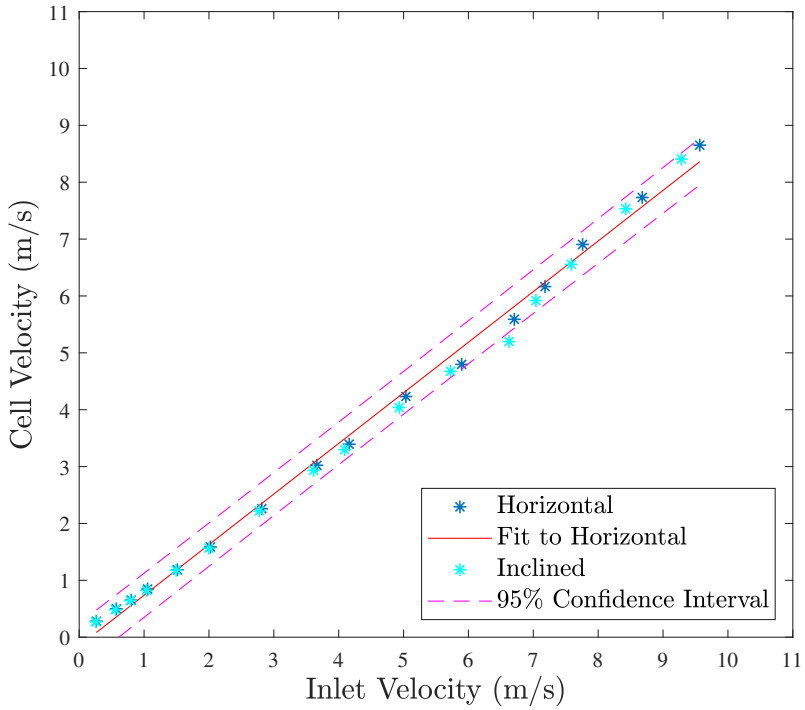

Figure C.48: Cell velocity vs. inlet velocity with 95% confidence intervals for cell 16

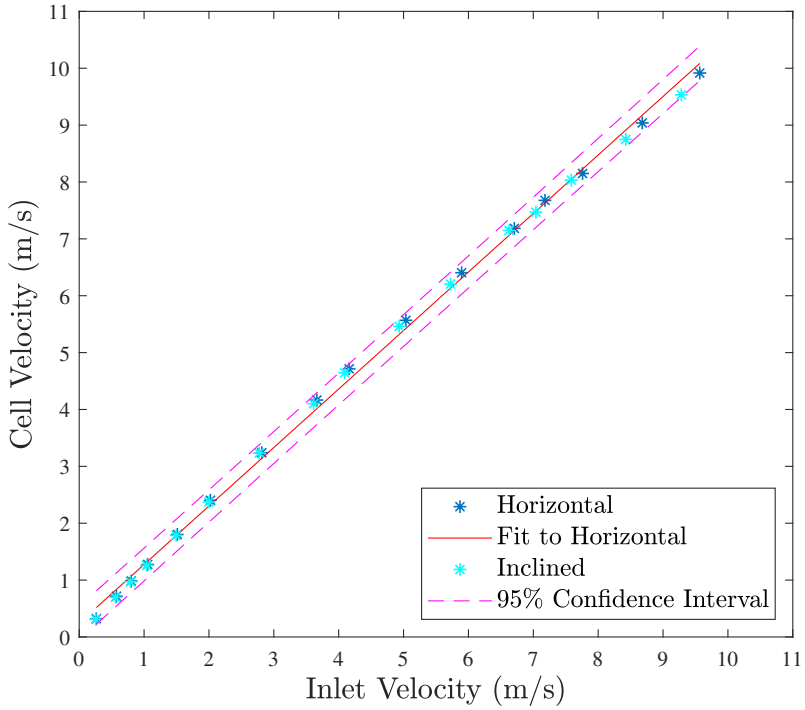

Figure C.49: Cell velocity vs. inlet velocity with 95% confidence intervals for cell 17

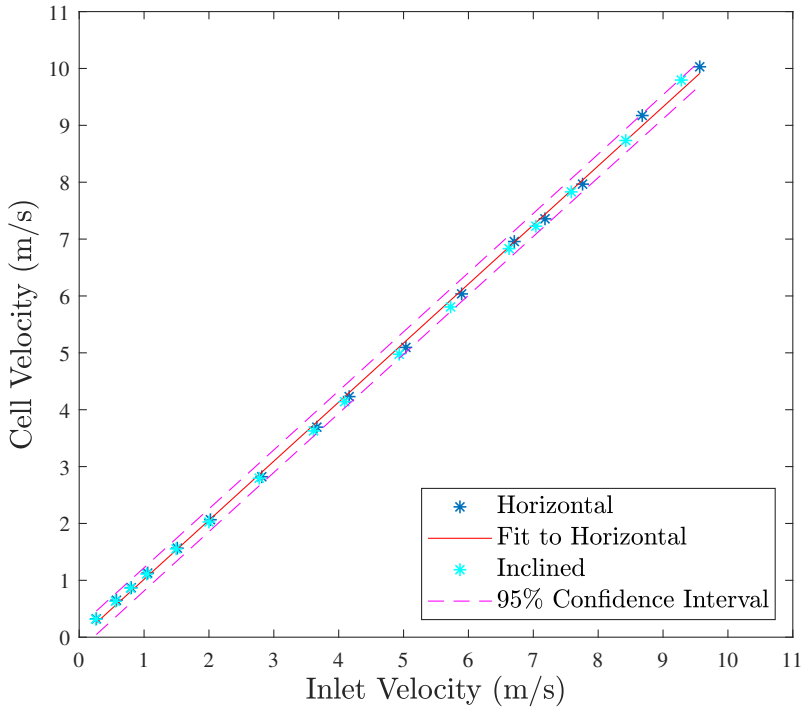

Figure C.50: Cell velocity vs. inlet velocity with 95% confidence intervals for cell 18

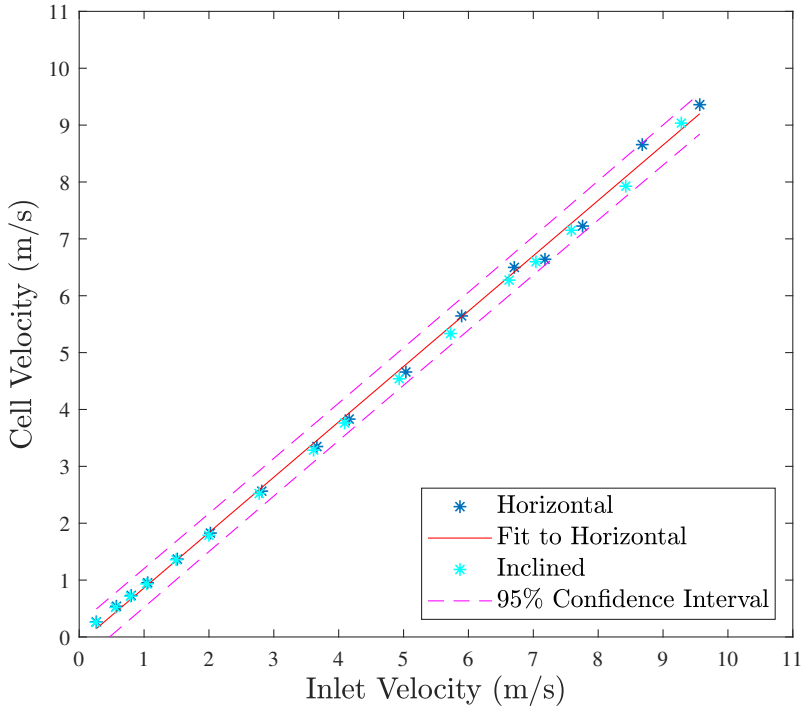

Figure C.51: Cell velocity vs. inlet velocity with 95% confidence intervals for cell 19

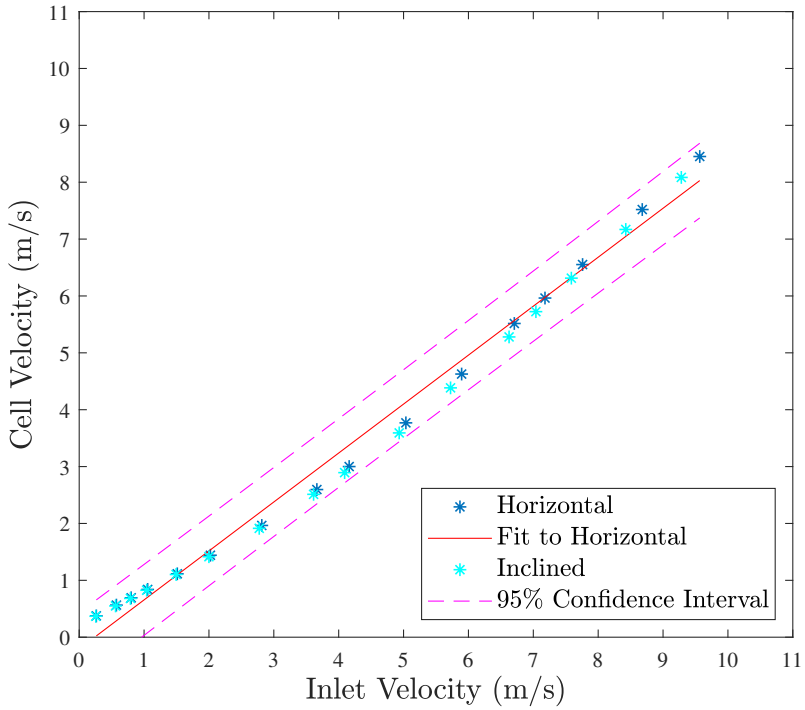

Figure C.52: Cell velocity vs. inlet velocity with 95% confidence intervals for cell 20

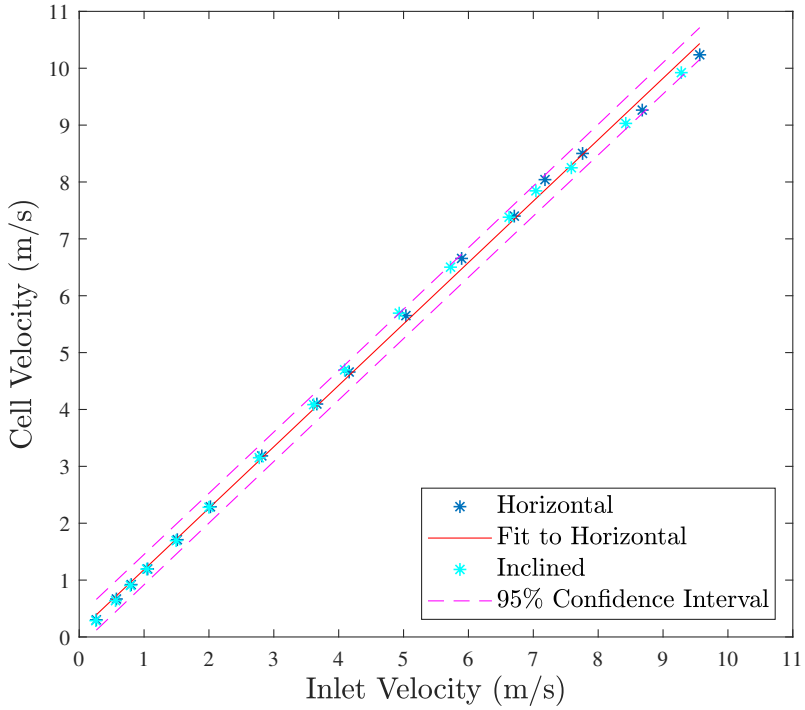

Figure C.53: Cell velocity vs. inlet velocity with 95% confidence intervals for cell 21

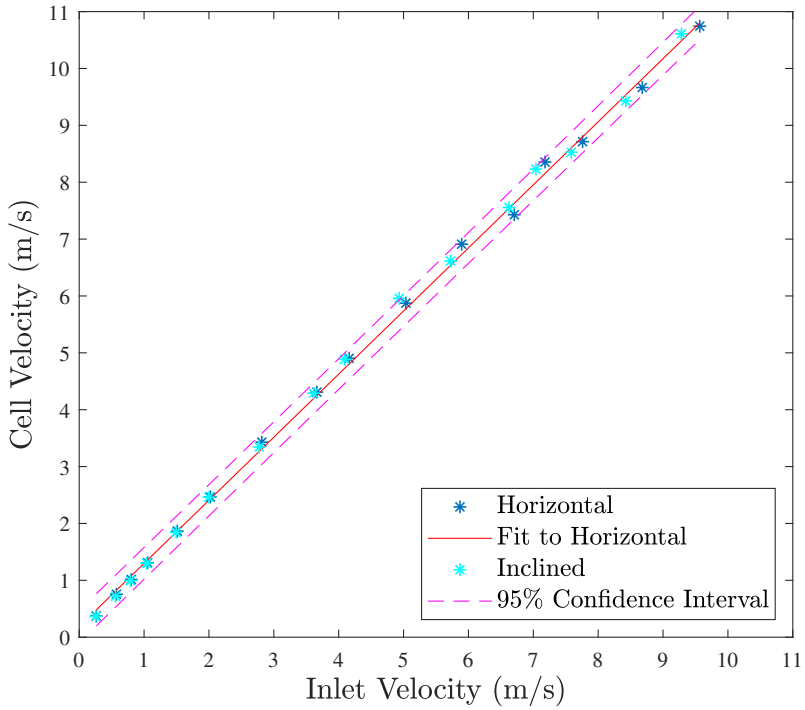

Figure C.54: Cell velocity vs. inlet velocity with 95% confidence intervals for cell 22

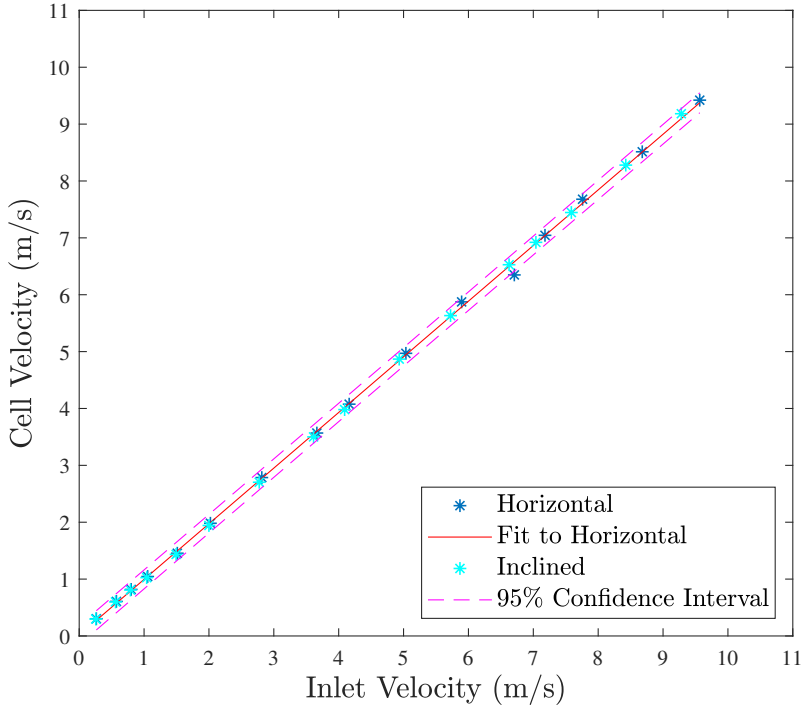

Figure C.55: Cell velocity vs. inlet velocity with 95% confidence intervals for cell 23

C.3 Results with Radiator in Inclined Position with Shroud Attached

C.3.1 Radiator Exit Plane Distribution Before and After Correction

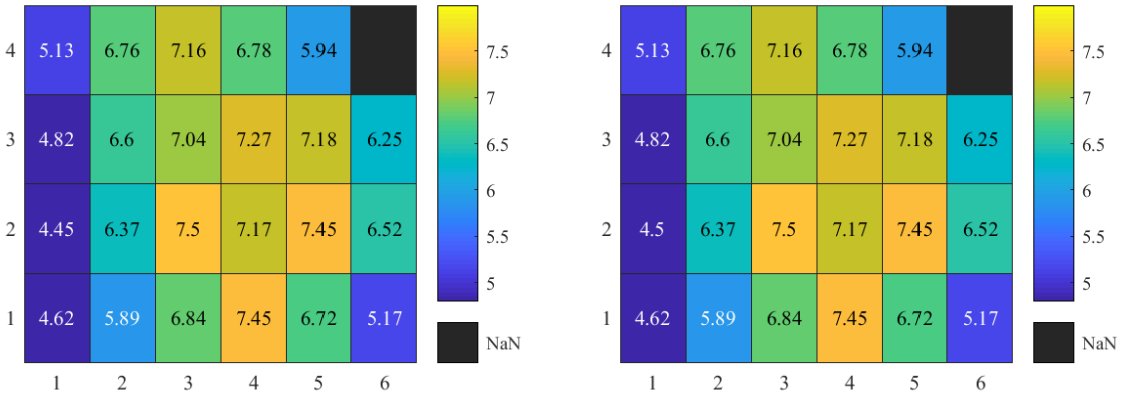

(a) Before correction (b) After correction

Figure C.56: Radiator exit plane flow distribution with shroud attached before and after correction for inlet velocity of 6.40 m/s

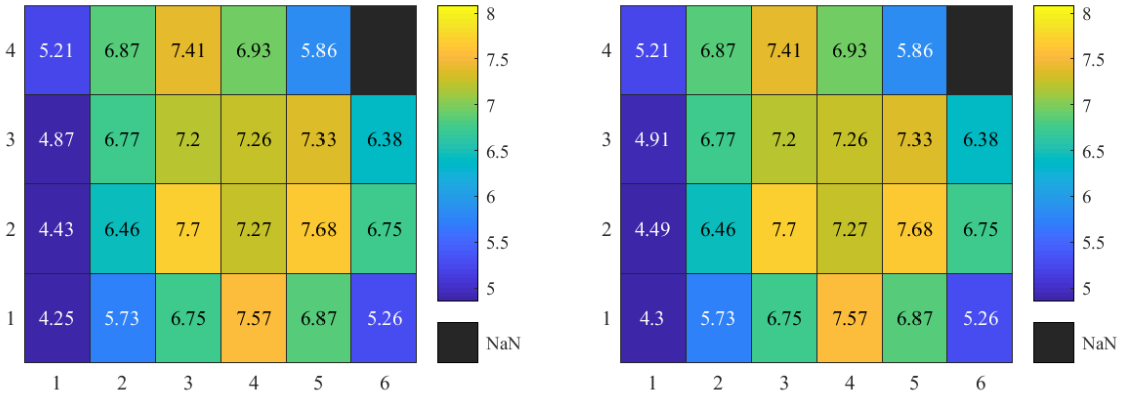

(a) Before correction (b) After correction

Figure C.57: Radiator exit plane flow distribution with shroud attached before and after correction for inlet velocity of 6.47 m/s

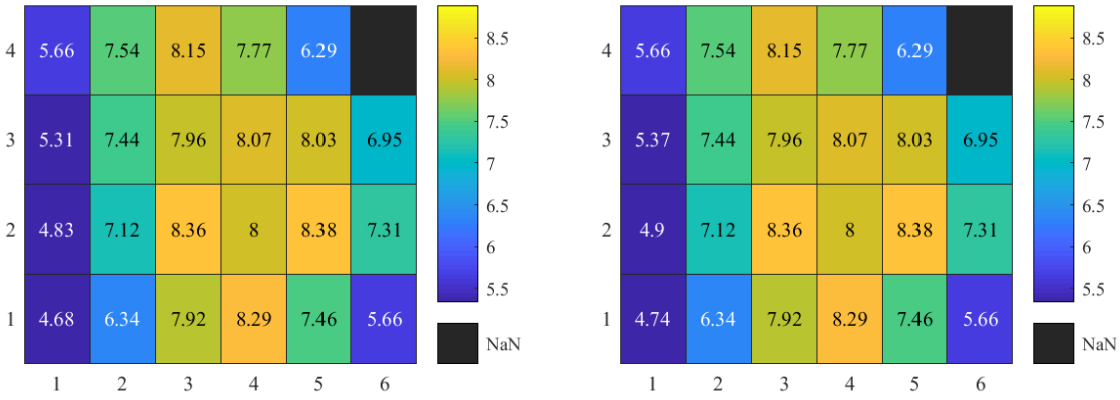

(a) Before correction

(b) After correction

Figure C.58: Radiator exit plane flow distribution with shroud attached before and after correction for inlet velocity of 7.11 m/s

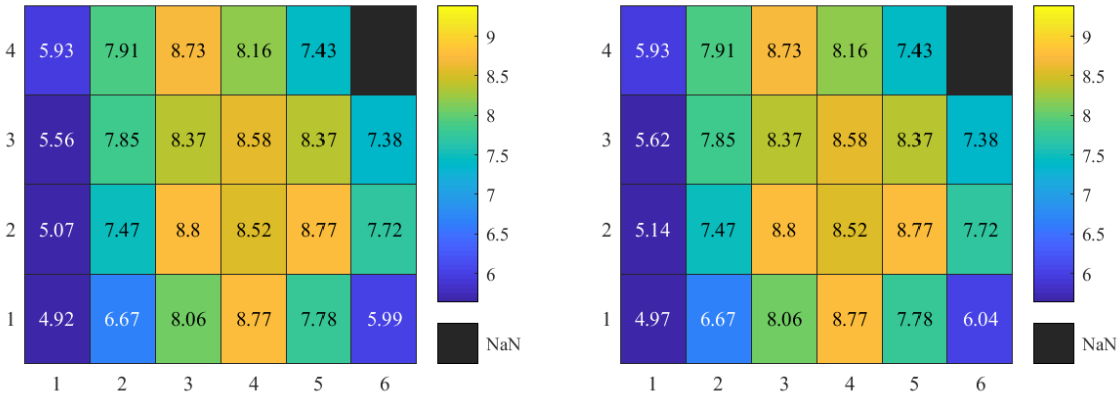

(a) Before correction

(b) After correction

Figure C.59: Radiator exit plane flow distribution with shroud attached before and after correction for inlet velocity of 7.51 m/s

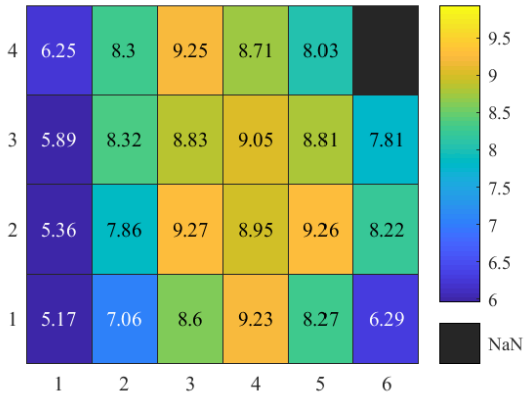

(a) Before correction

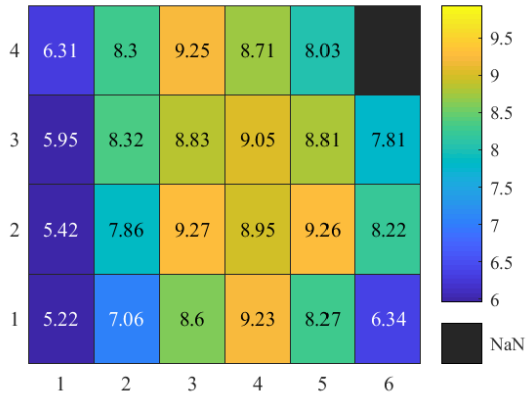

(b) After correction

Figure C.60: Radiator exit plane flow distribution with shroud attached before and after correction for inlet velocity of 7.95 m/s

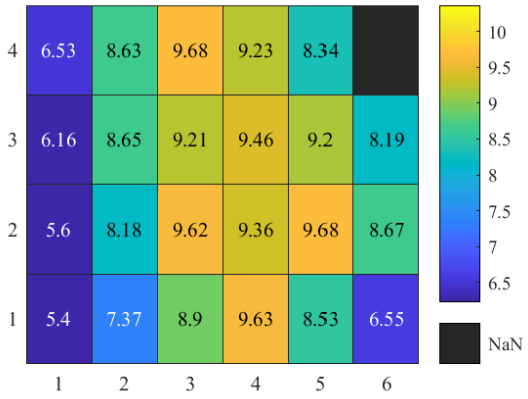

(a) Before correction

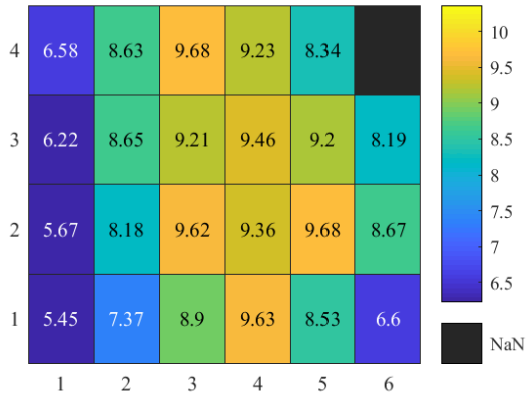

(b) After correction

Figure C.61: Radiator exit plane flow distribution with shroud attached before and after correction for inlet velocity of 8.29 m/s

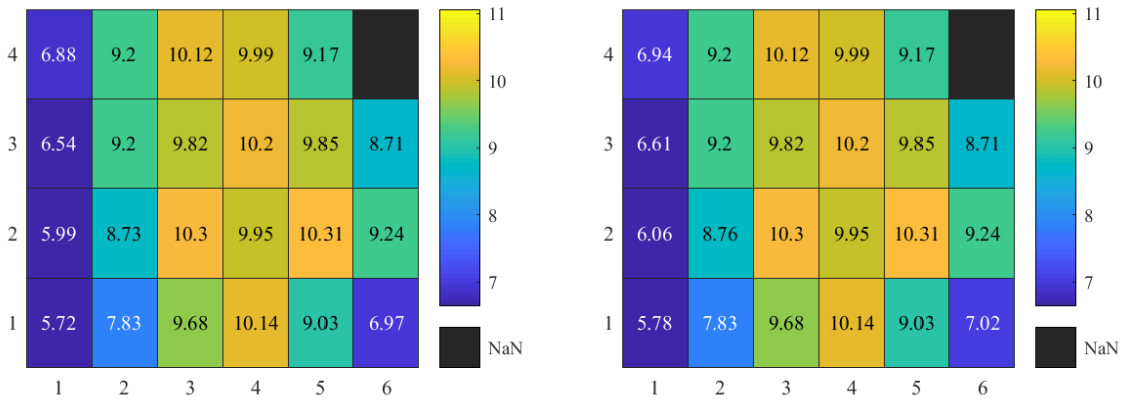

(a) Before correction

(b) After correction

Figure C.62: Radiator exit plane flow distribution with shroud attached before and after correction for inlet velocity of 8.85 m/s

C.3.2 Corrected Radiator Exit Plane Distribution

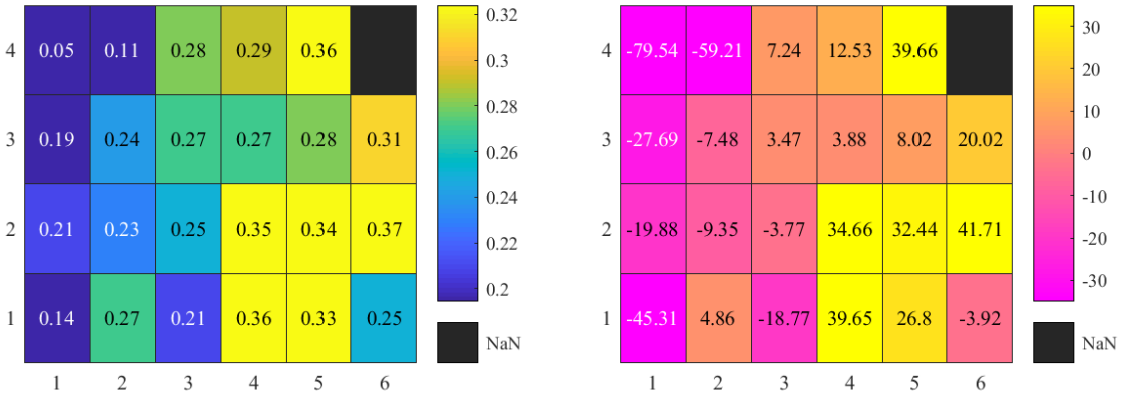

(a) Velocity (b) Percent difference

Figure C.63: Radiator exit plane flow distribution with shroud attached and inlet velocity of 0.26 m/s

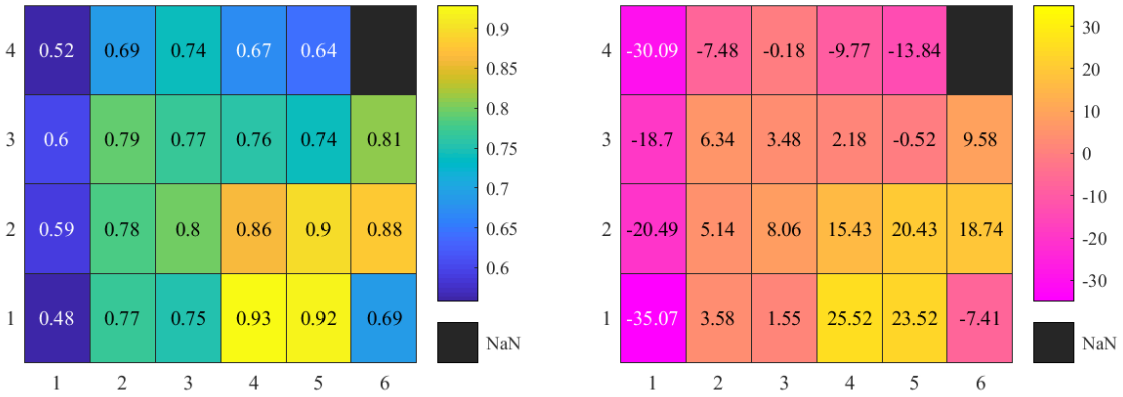

(a) Velocity (b) Percent difference

Figure C.64: Radiator exit plane flow distribution with shroud attached and inlet velocity of 0.74 m/s

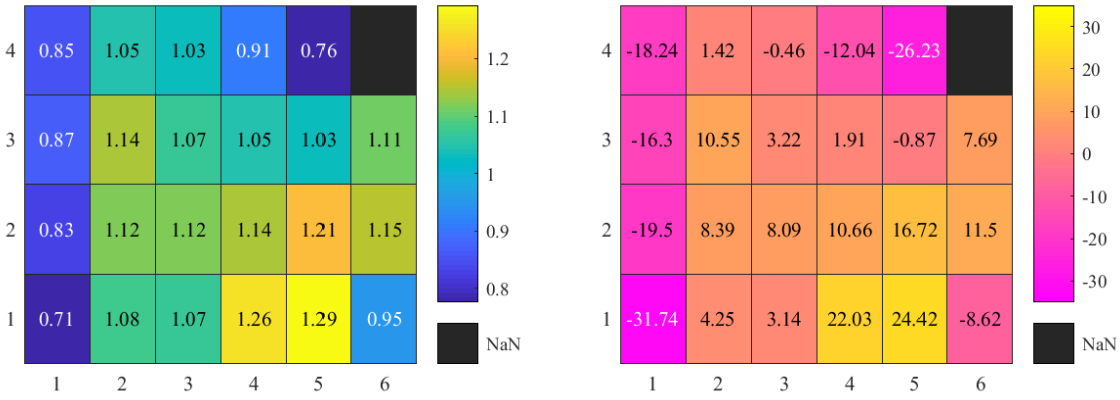

(a) Velocity

(b) Percent difference

Figure C.65: Radiator exit plane flow distribution with shroud attached and inlet velocity of 1.03 m/s

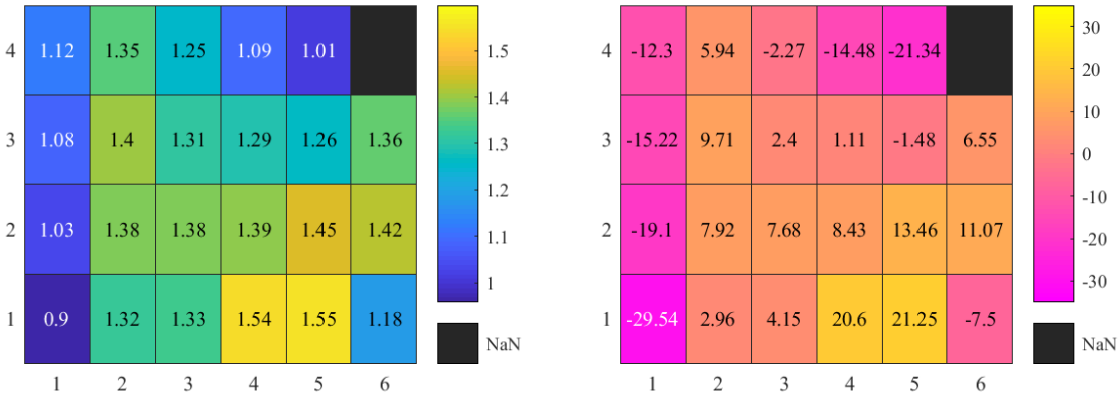

(a) Velocity

(b) Percent difference

Figure C.66: Radiator exit plane flow distribution with shroud attached and inlet velocity of 1.28 m/s

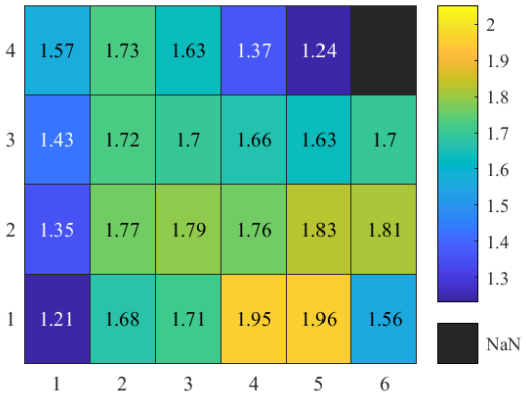

(a) Velocity

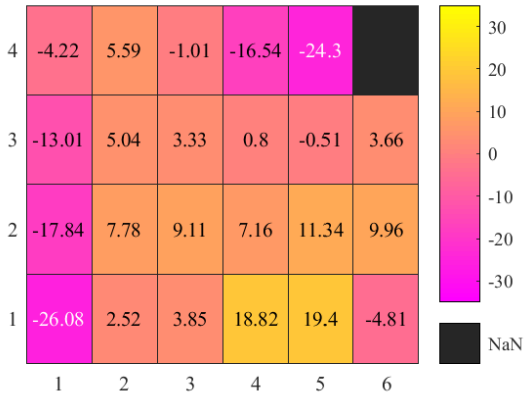

(b) Percent difference

Figure C.67: Radiator exit plane flow distribution with shroud attached and inlet velocity of 1.64 m/s

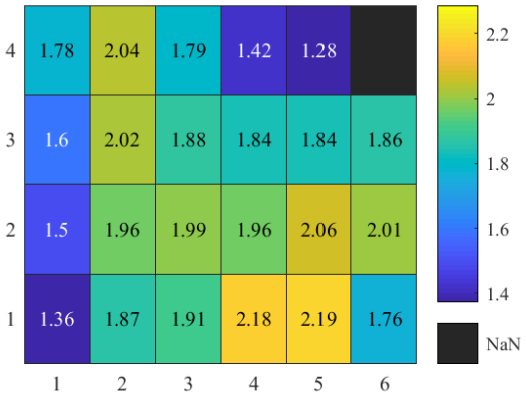

(a) Velocity

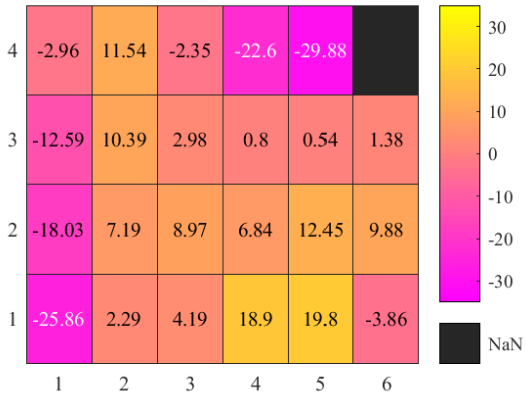

(b) Percent difference

Figure C.68: Radiator exit plane flow distribution with shroud attached and inlet velocity of 1.83 m/s

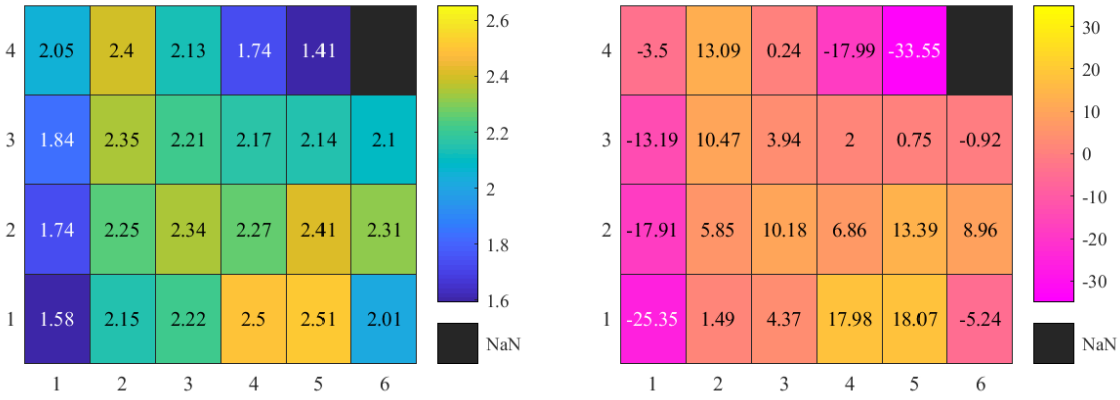

(a) Velocity (b) Percent difference

Figure C.69: Radiator exit plane flow distribution with shroud attached and inlet velocity of 2.12 m/s

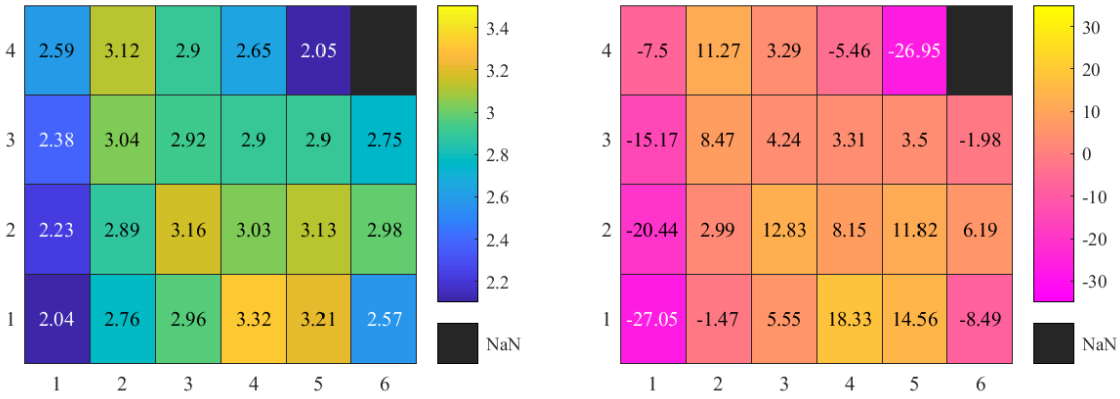

(a) Velocity (b) Percent difference

Figure C.70: Radiator exit plane flow distribution with shroud attached and inlet velocity of 2.80 m/s

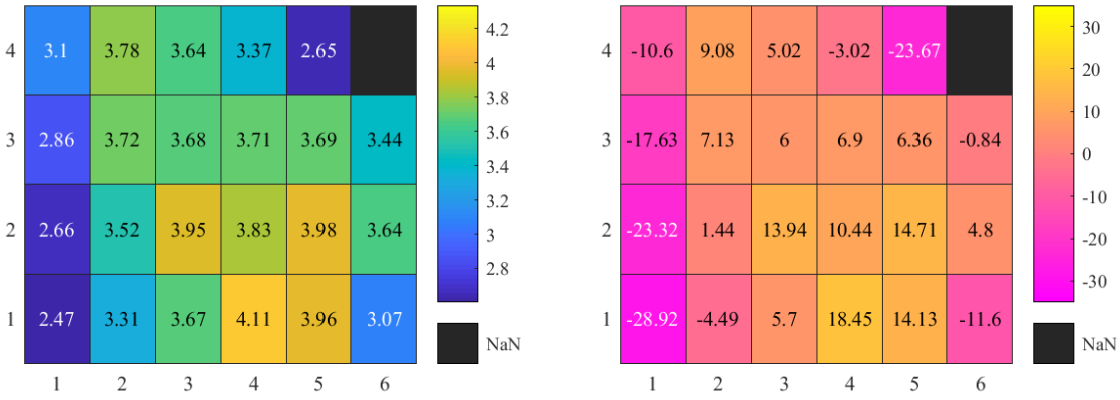

(a) Velocity (b) Percent difference

Figure C.71: Radiator exit plane flow distribution with shroud attached and inlet velocity of 3.47 m/s

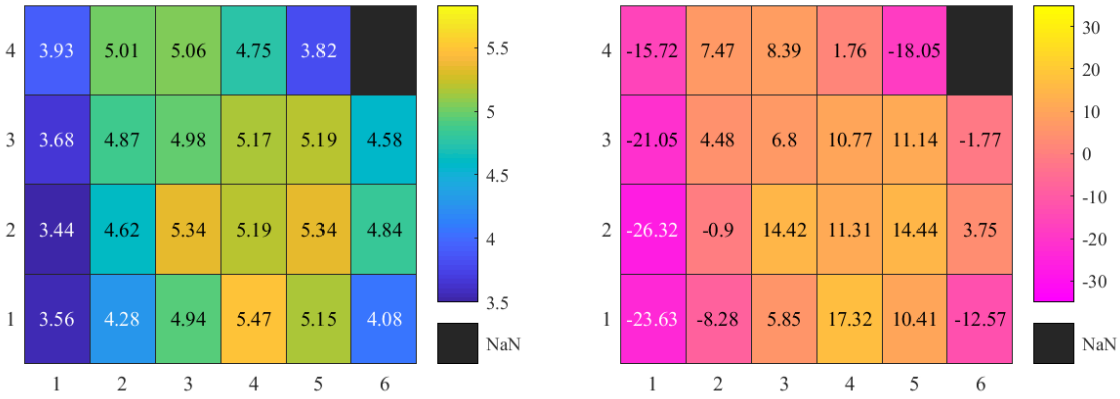

(a) Velocity (b) Percent difference

Figure C.72: Radiator exit plane flow distribution with shroud attached and inlet velocity of 4.67 m/s

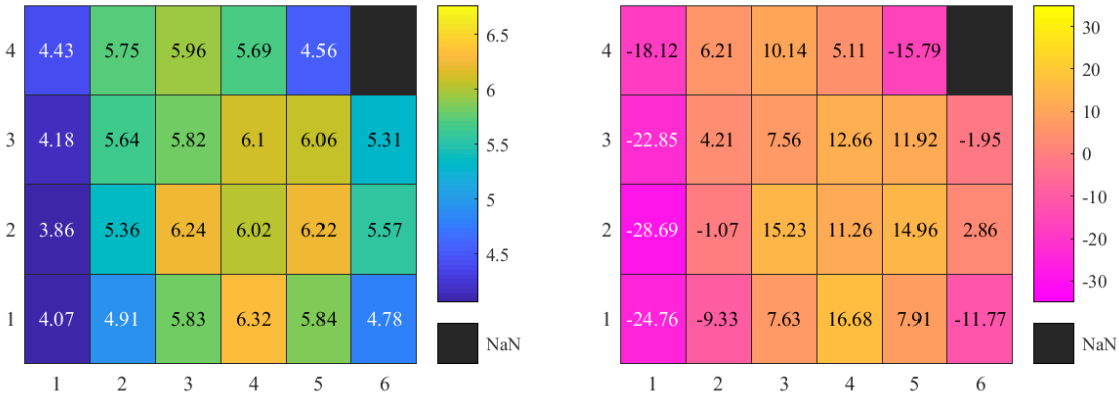

(a) Velocity (b) Percent difference

Figure C.73: Radiator exit plane flow distribution with shroud attached and inlet velocity of 5.41 m/s

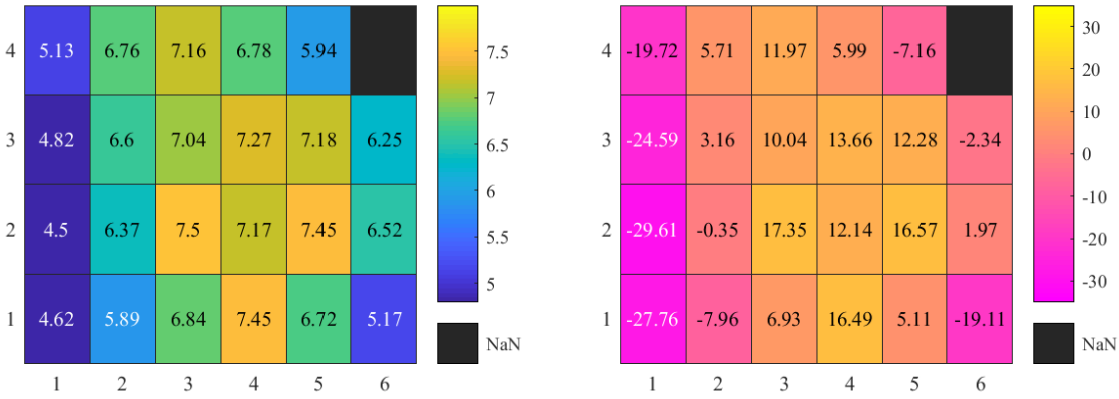

(a) Velocity (b) Percent difference

Figure C.74: Radiator exit plane flow distribution with shroud attached and inlet velocity of 6.40 m/s

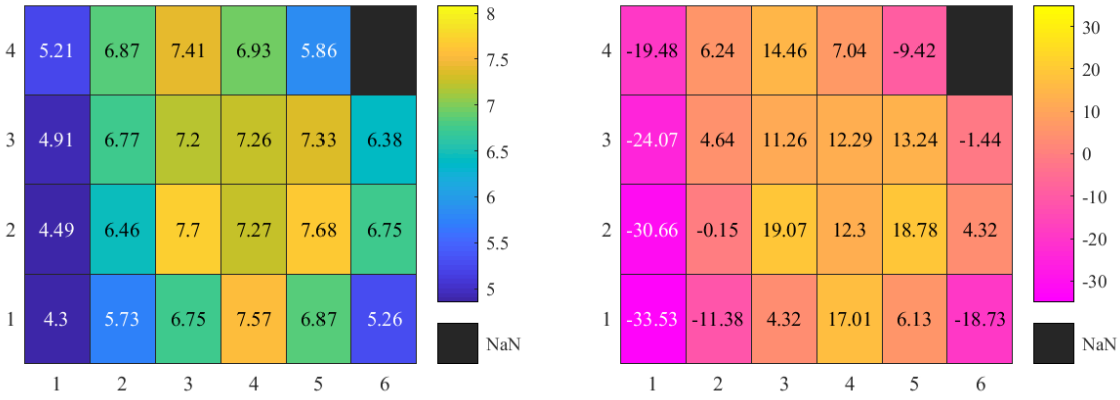

(a) Velocity (b) Percent difference

Figure C.75: Radiator exit plane flow distribution with shroud attached and inlet velocity of 6.47 m/s

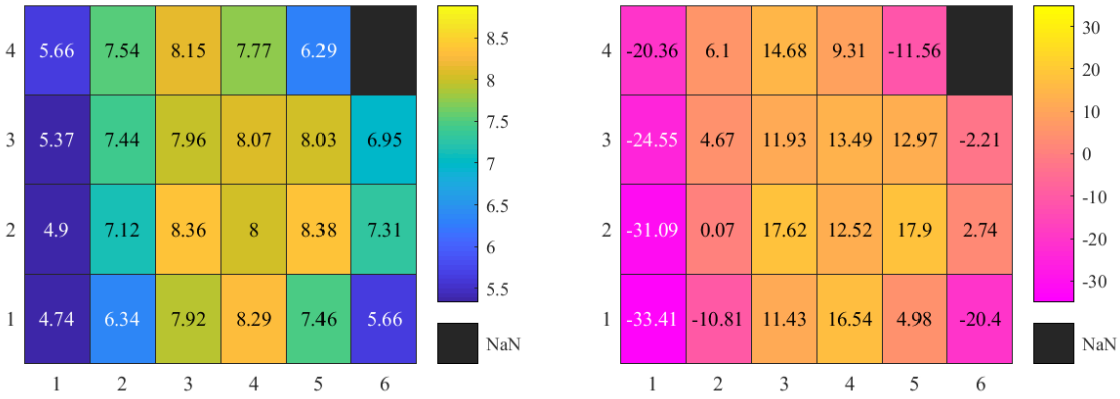

(a) Velocity (b) Percent difference

Figure C.76: Radiator exit plane flow distribution with shroud attached and inlet velocity of 7.11 m/s

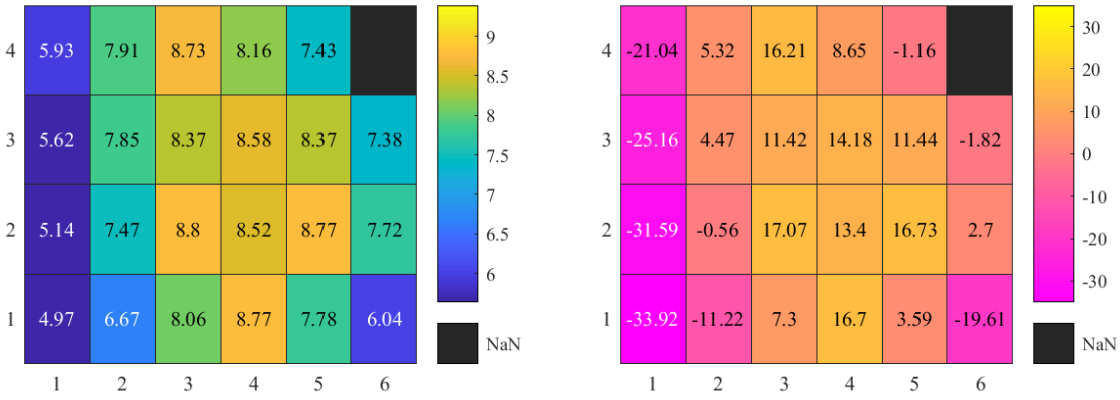

(a) Velocity (b) Percent difference

Figure C.77: Radiator exit plane flow distribution with shroud attached and inlet velocity of 7.51 m/s

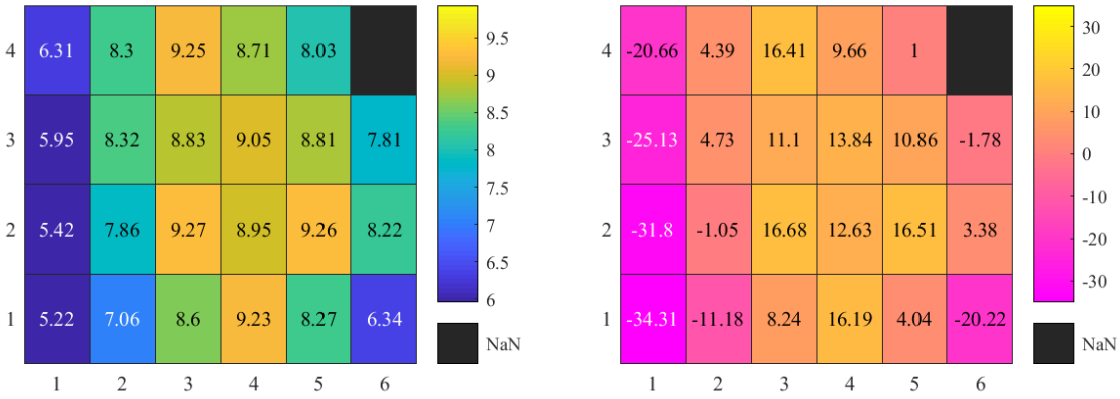

(a) Velocity (b) Percent difference

Figure C.78: Radiator exit plane flow distribution with shroud attached and inlet velocity of 7.95 m/s

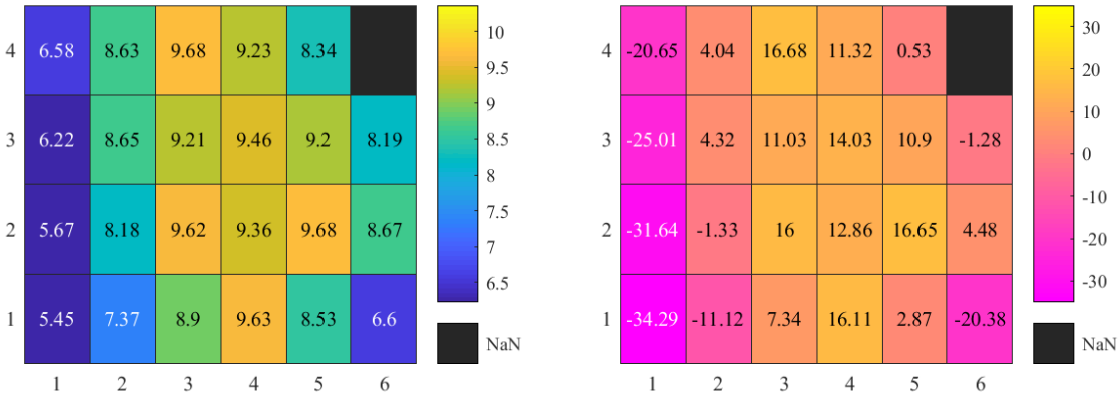

(a) Velocity (b) Percent difference

Figure C.79: Radiator exit plane flow distribution with shroud attached and inlet velocity of 8.29 m/s

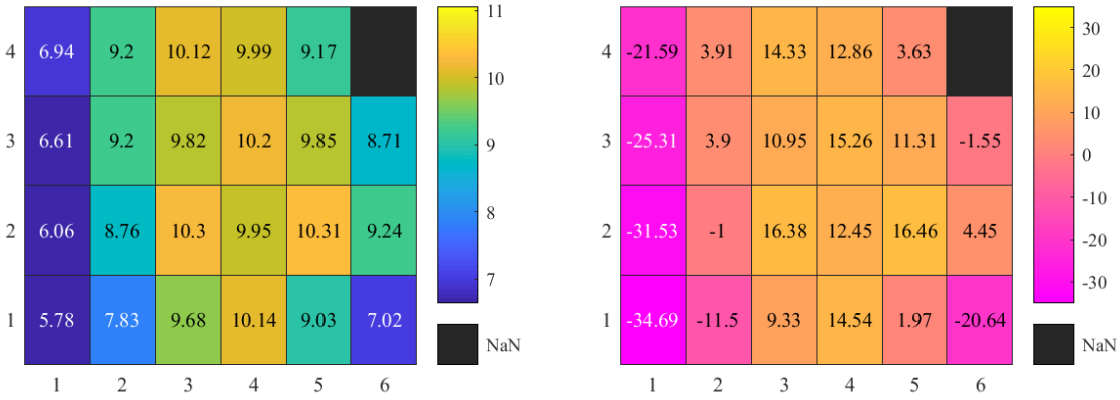

(a) Velocity (b) Percent difference

Figure C.80: Radiator exit plane flow distribution with shroud attached and inlet velocity of 8.85 m/s

BIBLIOGRAPHY

BIBLIOGRAPHY

[1] S. Ali and J. Foss. "The Discharge Coefficient of a Planar Submerged Slit-Jet". In: *Journal of Fluids Engineerings* 125 (4 2003), pages 613–619.

[2] John Anderson. *Computational Fluid Dynamics: the Basics with Applications*. McGraw Hill, 1995.

[3] David Barrent. "Controlled Diffusion Blade Axial Fan: Fluid Mechanical Mechanistic Effects on Fan Performance". Master's thesis. Michigan State University, 2015.

[4] H.H. Brunn. *Hot-wire Anemometry*. Oxford University Press, 1955.

[5] Yunus Cengel and Afshin Ghajar. *Heat and Mass Transfer: Fundamentals and Applications*. 5th edition. McGraw Hill, 2015.

[6] Michael D. Dusel. "An Experimental Investigation of the Aerodynamic Shroud with an Off-Highway Engine Cooling Fan". Master's thesis. Michigan State University, 2005.

[7] J. Foss, J. Peabody, M. Norconk, and A. Lawrenz. "Ambient temperature and free stream turbulence effects on the thermal transient anemometer". In: *Measurement Science and Technology* 17.9 (2006), pages 2519–2526.

[8] J. Foss, J. Schwannecke, A. Lawrenz, M. Mets, S. Treat, and M. Dusel. "The thermal transient anemometer". In: *Measurement Science and Technology* 15.11 (2004), pages 2248–2255.

[9] F. Gessner and G. Moller. "Response behaviour of hot wires in shear flow". In: *Journal of Fluid Mechanics* 47 (3 1971), pages 449–468.

[10] Incropera, DeWitt, Bergman, and Lavine. *Fundamentals of Heat and Mass Transfer*. 6th edition. John Wiley & Sons, 2006.

[11] James Leung. "Nonuniform Flow over a Thermal Transient Anemometer". Master's thesis. Michigan State University, 2018.

[12] S. Morris and J. Foss. "Transient thermal response of a hot-wire anemometer". In: *Measurement Science and Technology* 14.3 (2003), page 251.

[13] S. Morris, D. Neal, J. Foss, and G. Cloud. "A moment-of-momentum flux mass air flow measurement device". In: *Measurement Science and Technology* 12 (2001), N9–N13.

[14] Frank M. White. *Fluid Mechanics*. 7th edition. McGraw Hill, 2011.